EXPERIMENTAL EVALUATION OF TERRESTRIAL, UNDERWATER AND AERIAL FSO SYSTEMS WITH POINTING ERRORS

HASAN TAHSIN TOPLAR

ÖZYEĞİN UNIVERSITY

JULY, 2025

EXPERIMENTAL EVALUATION OF TERRESTRIAL, UNDERWATER AND AERIAL FSO SYSTEMS WITH POINTING ERRORS

by
Hasan Tahsin Toplar

Dissertation
Submitted in Partial Fulfillment of the
Requirements for the Degree of

Doctor of Philosophy

in
Electrical and Electronics Engineering

Advisor: Prof. Murat Uysal

Graduate School of Science and Engineering
Özyeğin University
İstanbul

July, 2025

EXPERIMENTAL EVALUATION OF TERRESTRIAL, UNDERWATER AND AERIAL FSO SYSTEMS WITH POINTING ERRORS

Approved by:

Prof. Murat Uysal, Advisor
Department of Electrical and Electronics Engineering
Özyeğin University

Asst. Prof. Çağatay Edemen
Department of Electrical and Electronics Engineering
Özyeğin University

Asst. Prof. Kadir Durak
Department of Electrical and Electronics Engineering
Özyeğin University

Prof. Serhan Yarkan
Department of Electrical and Electronics Engineering
Istanbul Ticaret University

Asst. Prof. Tahsin Yılmaz
Department of Electrical and Electronics Engineering
Yeni Yüzyıl University

Approval Date:

I dedicate this Ph.D. dissertation to my dear mother and father, who brought me to this life, which is far more precious than one could ever ask for.

DECLARATION OF ORIGINALITY

I hereby declare that I am the sole author of this thesis and that this is the true copy of my thesis, including the final revisions, approved by my thesis committee. All data and information have been obtained, produced, and presented in accordance with the rules of research ethics and principles of academic honesty. As required by these rules, to the best of my knowledge I have acknowledged ideas, thoughts, and any copyrighted material in accordance with the standard referencing rules. I certify that any part of this thesis has not been submitted for a degree or diploma in another educational institution.

Hasan Tahsin Toplar

ABSTRACT

With their high data rate capacity, Free Space Optical (FSO) communication systems can be used for last mile access, backhauling and fiber optic replacement. Terrestrial FSO links are typically installed on building roofs and are prone to building sways due to dynamic wind loads. In Underwater Wireless Optical Communications (UWOC) systems applications, these transmitters can be installed on Unmanned Underwater Vehicles (UUV), seafloor-mounted beacons, and surface buoys; some of which are influenced by environmental factors including sea waves, currents, and winds. In aerial systems, FSO can be installed on Unmanned Aerial Vehicles (UAV) which are subject to aerodynamic disturbances such as wind during flight. Motivated by these trends, we work on developing realistic models for analyzing the behavior and effects of pointing error in FSO systems. We first design and build a 5 Degree Of Freedom (DOF) motion table in order to experimentally generate pointing errors and study its effects. We then work on a realistic modeling of pointing errors in terrestrial FSO links, relating them to the underlying physical phenomena. Towards this end, we use a civil engineering software and conduct extensive simulations to characterize the behavior of various building sizes under wind loads. Secondly we model a UWOC system installed on an ocean buoy. We use an oceanographic marine simulation software to simulate the rotational motions of a realistic ocean buoy with moorings and study its pointing error behavior in the presence of waves and winds. Thirdly we model and simulate the motion behavior of a quadcopter UAV in hovering mode under the impact of wind-induced disturbances. Afterwards we model the pointing error over extended hovering durations under the effects of wind. This study aims to deliver a deeper understanding of FSO systems and fills the gap by providing more realistic models to analyze FSO behavior in the presence of pointing errors.

Keywords: FSO, Pointing Error, UWOC, UAV-to-Ground

ÖZET

Yüksek veri aktarım kapasitesine sahip serbest uzay optik (FSO) haberleşme sistemleri, son kilometre erişimi, geri taşıma (backhaul) ve fiber optik altyapının yerine kullanılabilir. Karasal FSO bağlantıları genellikle bina çatılarına kurulur ve dinamik rüzgar yükleri nedeniyle bina sallanmalarına maruz kalabilir. Su altı kablosuz optik haberleşme (UWOC) sistem uygulamalarında, bu vericiler insansız su altı araçlarına (UUV), deniz tabanına monte edilmiş işaretçilere ve su yüzeyi şamandıralarına takılabilir. Bunlar da deniz dalgaları, akıntılar ve rüzgarlar gibi çevresel faktörlerden etkilenebilir. Hava sistemlerinde ise, FSO insansız hava araçlarına (UAV) entegre edilebilir ve uçuş sırasında rüzgar gibi aerodinamik bozucu etkilere maruz kalabilir. Bunlardan motive olarak, bu çalışmada FSO sistemlerindeki yönlendirme hatalarının davranışını ve etkilerini analiz etmek için gerçekçi modeller geliştirilmiştir. Öncelikle, deneysel olarak yönlendirme hatalarını üretmek ve etkilerinin incelenmesi amacıyla 5 serbestlik derecesine (DOF) sahip bir hareket masası tasarlanıp, inşa edilmiştir. Daha sonra, yönlendirme hatalarının karasal FSO bağlantılarında gerçekçi bir şekilde modellenmesine çalışılmış ve bunların temel çevresel etkenlerle ilişkisi kurulmuştur. Bu doğrultuda, farklı bina boyutlarının rüzgar yükleri altındaki davranışını karakterize etmek için kapsamlı simülasyonlar yapılmıştır. Daha sonra, bir okyanus şamandırasına kurulan UWOC sistemi modellenmiştir. Sistemin bağlama halatlarıyla birlikte dönme hareketlerini simüle etmek ve dalgalar ile rüzgarın neden olduğu yönlendirme hatası davranışlarını incelemek amacıyla oşinografik simülasyon programı kullanılmıştır. Üçüncü olarak, rüzgarlı havada sabit duran bir UAV'nin hareket davranışı modellenmiş ve simüle edilmiştir. Ardından, rüzgar etkisi altında yönlendirme hatası modellenmiştir. Bu çalışma, FSO sistemlerine ilişkin daha derin bir anlayış sunmayı amaçlamakta ve yönelim hatalarının analizi için gerçekçi modeller sunmaktadır.

Anahtar Kelimeler: FSO, Yönelim Hatası, UWOC, UAV-to-Yer

TABLE OF CONTENTS

LIST OF TABLES

LIST OF FIGURES

LIST OF ACRONYMS AND ABBREVIATIONS

AoA	Angle of Arrival
AWGN	Additive White Gaussian Noise
BER	Bit Error Rate
CAD	Computer Aided Drawing
cm	Centimeter
DOF	Degree of Freedom
FSO	Free Space Optics
GUI	Graphical User Interface
IM/DD	Intensity Modulation / Direct Detection
Kb/S	Kilobit per Second
LD	Laser diode
LED	Light-emitting diode
LOS	Line of Sight
m/s	Meters per Second
Mb/s	Megabit per Second
mph	Miles per Hour
mrad	Milliradians

Nm	Newton meters
OOK	On-off Keying
PD	Photodiode
PLC	Programmable Logic Controller
SNR	Signal-to-Noise Ratio
UAC	Underwater Acoustic Communication
UAV	Unmanned Aerial Vehicle
UOWC	Underwater Optical Wireless Communication
UOT	Underwater Optical Turbulence
UUV	Unmanned Underwater Vehicle

1. INTRODUCTION

1.1 Motivation

Free Space Optical (FSO) communication systems use laser transmitters with operation wavelengths in the near infrared band (750–1600 nm) and provide line-of-sight wireless connectivity [1]. With their high data rate capacity, FSO systems can be used for last mile access, backhauling and fiber optic replacement. In the design of terrestrial FSO links, various performance degradations must be considered. In addition to atmospheric attenuation and turbulence-induced fading, FSO links are subject to pointing errors (PE) [2].

In a terrestrial link, dynamic wind loads, thermal expansion and vibrations cause buildings to sway. High-rise buildings sway in three directions along wind, across wind, and torsional. This results in the misalignment of optical beam at the receiver side and can deteriorate the performance of the link by introducing fluctuations in optical intensity [3]. Several works exist in the literature that present the statistical behavior of pointing error in the presence of sway in multiple axes either with the same magnitude and standard deviation or independent from each other with each having its own statistical characteristics.

Due to the growing demand for wireless communication systems tailored to underwater settings, there is a compelling need to support emerging applications such as monitoring offshore installations, controlling Unmanned Underwater Vehicles (UUVs), ship-to-shore and ship-to ship communications. Acoustic transmission has been adopted widely and became popular over the past decade, however it operates in the orders of Kb/s and hence does not suffice the ever growing need of increased data rate. Underwater wireless optical communication stands out for its ability to deliver enhanced security, minimal latency, and significantly higher data transmission rates compared to acoustic communication, in the orders of Mb/s. This has led the research on developing and advancing optical wireless communication systems designed for underwater environments. In marine FSO systems, path loss and underwater optical turbulence (UOT) leads to fluctuations in the average received power [4]. The turbulence in the seas may arise from waves, motion of the sea surface, currents, winds as well as salinity levels due to changing water temperature [5]. While some of these changes affects the refractive index of the transmission medium, some cause pointing error. This study focuses only on the physical incidents that result in pointing error such as the waves and the motion of the sea surface.

In FSO systems Line-of-Sight (LOS) is another requirement between the receiver (Rx) and the transmitter (Tx). Inserting relay nodes to improve link distance, performance and reliability have been considered in recent studies. Towards this end the usage of UAVs have been considered [6]. However, drones are prone to weather conditions. Wind, for example, is a major contributor to the pointing error of a FSO system installed on a drone and it can deteriorate the channel performance significantly [7].

In all of the aforementioned works, the variance values of jitter are provided without relating them to the underlying physical phenomena. In practice, jitter occurs due to the sway behavior of a building, and its strength depends on the wind force as well as static forces on the building coupled with its height and shape. Similarly, on a marine FSO, the jitter may arise from wave heights and the shape of sea surface due to turbulent winds. On an aerial FSO system installed on a UAV, the wind conditions during the flight might alter the drone position and orientation causing significant pointing errors.

Towards this end, we use both experimental and simulation based tools to model and simulate the pointing error behavior in terrestrial, marine and aerial systems. Our approach makes it possible to quantify the amount of pointing error that might arise in a FSO system and link it to the underlying physical phenomena causing the performance degradation.

1.2 Dissertation Outline

The dissertation has four main parts and can be summarized as follows:

1. In the first part, mechanical, electronic and controller design of a XYZ motion table platform is presented. This platform is able to move in 5 axes and is able to faithfully reproduce pointing errors for a FSO system. The system houses 5 step motors all controlled by a PLC and Labview [8]. By using this setup, one of the most popular pointing error models in the literature was emulated and the results have been statistically analyzed to confirm the correct functionality of the motion platform. Afterwards, actual coordinates of building sway data generated by the next chapter in this study have also been emulated and channel performance was analyzed in the presence of pointing errors for a FSO system.

2. In the second part, terrestrial FSO links are modelled and analyzed. Towards this end, an industry standard civil engineering software is used to model the sway behavior of a building under the effects of wind load. Simulations involved square buildings of various heights and widths, whilst facing winds between 0 to 60 mph. The sway characteristics of the building are statistically analyzed and a closed form expression regarding building motion is achieved. Afterwards, error performance in the presence of pointing error is studied and a closed form expression for the BER is derived.

3. In the third part, a buoy based UWOC system is modelled. Towards this end we use an oceanographic marine simulation software to simulate the rotational motions of a realistic ocean buoy with moorings and analyze the effect of environmental factors such as wave height, wind speed and wind direction on the motion behavior of the

buoy. Resulting pointing error due to these motions are derived. Error performance is studied afterwards and a closed form expression for the Bit Error Rate (BER) is derived.

4. In the fourth part, a quadcopter UAV is modeled in Matlab [9] and its flight behavior was analyzed during hovering state while facing winds of varying speeds and directions. Statistical analysis is then performed on the tilt angle and lateral position of the UAV and a closed form expression is obtained for both radial displacements. Afterwards a novel PE model is derived and presented.

1.3 Organization

The dissertation is organized as follows. In Chapter 2, the design and usage of XYZ motion table is presented. In Chapter 3, modelling of building sway under wind, and its effects on FSO pointing error is presented. In Chapter 4, pointing errors in UWOC system experiencing waves and winds is theoretically analyzed. In Chapter 5, a quadcopter UAV is modelled and its hovering flight is simulated under various wind conditions. Radial displacement Probability Density Function (PDF) and PE PDF are derived. In Chapter 6, conclusion and future works are given. The chapters are detailed as follows:

- **Chapter 2** has six sections. It details the mechanical, electrical and control design of the 5-axis XYZ motion table and its experimental performance regarding the measurements and analysis of pointing error.

- **Chapter 3** has four sections. It details the modeling of a tall building with an industry standard civil engineering software, analysis of its sway motion under the wind turbulence, and the modeling of the pointing error behavior by parameterizing the building sway to various physical parameters of the building and the wind.

- **Chapter 4** has five sections. It details the modeling of a realistic ocean buoy with an oceanographic simulation software and analyzes its rotational motion under the effects of sea waves and winds. Afterwards a closed-form model of the pointing error and channel performance are derived and presented.

- **Chapter 5** has four sections. It details the modeling of a realistic quadcopter UAV with engineering simulation software and analyzes its rotational and translational motions under the effect of winds. Afterwards pointing error model is derived and presented.

- **Chapter 6** is the conclusion and the future works.

2. DESIGN OF XYZ MOTION TABLE FOR EXPERIMENTAL VERIFICATION OF POINTING ERRORS

2.1 Introduction

FSO communication systems can be used in a wide range of application areas including enterprise/campus connectivity, backhauling for cellular networks, fiber back-up and airborne communications among others. With the recent increasing interest on this promising technology, there is a need for a comprehensive understanding of system limitations in practical propagation settings. Optical signal propagation in free space is affected by atmospheric turbulence and pointing errors, which fade the signal at the receiver and deteriorate the link performance [2, 3].

Pointing error due to misalignment of optical beam at the receiver side in a line-of-sight FSO communication system is an important issue and can deteriorate the performance of FSO link by introducing fluctuations in optical intensity. The impact of pointing error first has been investigated for inter-satellite space-based FSO links [10, 11, 12] which operate over ranges of many thousands of kilometers. In these links, the assumption of negligible detector aperture size with respect to the beam width at the receiver is made, as a result of large distances. The effect of pointing error and atmospheric turbulence has also been considered in terrestrial links of shorter range. This is usually caused by wind loads and building sways which enhance signal fading at the receiver [13]. Modeling the combined impact of turbulence and pointing error, as well as the impact of the BER of communication systems, has been considered in [14]; however, the detector size is assumed to be negligible compared to the beam width at the receiver, and only un-coded transmission is considered. Optimization of the beam width in FSO systems to minimize BER has also been investigated using the small detector model [15]. Joint optimization of beam width and coding for FSO systems to maximize the channel capacity subject to outage has been studied in this work and a statistical model for the optical intensity fluctuations at the receiver due to the combined effects of atmospheric turbulence and pointing error is derived. However, the ideal Gaussian beam shape is considered, and no experimental work is included.

Due to the problems with the prediction of occurrence of specific degrading effects, and to repeat the measurements under the same conditions, it is highly desirable to quantify the FSO system performance in a controlled laboratory environment. Along this direction, several works have been recently reported in the literature [16, 17, 18, 19, 20] where various environmental effects (turbulence, fog, smoke, dust, ash, and sand) are investigated. However, due to its difficulty, the number of experiments conducted on characterizing pointing error and beam misalignment is sporadic and no experiment has been reported under laboratory conditions to the best of our knowledge.

In this chapter, we first present the XYZ table and show its mechanical, electrical and controller design details. We then proceed to conduct experiments using our robotic XYZ table and investigate the performance of FSO links over slow fading channels. Under controlled laboratory environment using a XYZ table, pointing error of FSO systems due to building sways is simulated and analyzed. Under the assumption of Gaussian beam shape the PDF of pointing error coefficient in [11] is experimentally verified.

The robotic XYZ table in this study is a kinematic manipulator capable of moving in 5 Degrees of Freedom (DOF), namely X, Y, Z, roll (ϕ) and pitch (θ). It was designed and built in order to experimentally analyze the FSO channel outage behavior under pointing error caused due to winds and building sways. The end effector follows a path generated by Labview in a random Gaussian fashion.

The rest of this chapter is organized as follows: Chapter 2.2 presents the communication channel model, along with mechanical, electrical and controller properties of the XYZ table. In Chapter 2.3, the experimental setup and the emulation of building sway displacements using XYZ table is presented. In Chapter 2.4, generation of Gaussian beam and verification of its shape is presented. In Chapter 2.5, experimental verification of pointing error is presented. In Chapter 2.6, we conclude the chapter.

2.2 System Model

2.2.1 Optical Channel Model

In a FSO system the received signal is a function of incident optical power, and detector responsivity (R). The received signal (y) is a combination of the transmitted intensity (x), channel gain (h), AWGN (n) and can be modelled as [11]

$$y = hRx + n \tag{2.1}$$

The channel gain h , or sometimes referred as channel state, consists of three main components. Atmospheric turbulence h_a , path loss h_l and pointing error h_p . Hence the channel gain is defined as

$$h = h_a h_l h_p \tag{2.2}$$

The pointing error loss factor $h_p\,(.)$ fluctuates due to the radial displacement between the transmitter and the receiver. This displacement is a combination of both vertical and horizontal displacement and can be written as

$$r = \|\mathrm{r}\| = \sqrt{r_x^2 + r_y^2} \tag{2.3}$$

A Gaussian beam propagating through a distance z to a circular aperture with radius a , affected by the radial displacement r , leads to the fraction of the collected power at the receiver to be approximated as [11].

$$h_p(r;z) \approx A_0 \exp\left(-\frac{2r^2}{w_{L_e}^2}\right) \tag{2.4}$$

where A_0 is the fraction of power collected at $r = 0$, w_L is the beam waist (radius calculated at e^{-2}), w_{L_e} is the equivalent beam width and a is the aperture radius. They are defined in Equations (2.5)- (2.7) as follows

$$A_0 = erf[(v)]^2 \tag{2.5}$$

$$w_{L_e}^2 = w_L^2 \sqrt{\frac{\pi erf(v)}{2v\exp(-v^2)}} \tag{2.6}$$

$$v = \sqrt{\frac{\pi a^2}{2w_L^2}} \tag{2.7}$$

Assuming the radial displacement is caused by horizontal (r_x) and vertical (r_y) swings both having an independent Gaussian distribution, the resulting radial displacement PDF is in the form of a Rayleigh distribution and is defined as Equation (2.8) [11].

$$f_r(r) = \frac{r}{\sigma_s^2} \exp\left(-\frac{r^2}{2\sigma_s^2}\right), \mathrm{r} > 0 \tag{2.8}$$

where σ_s is the standard deviation of motion and is identical for all axes ($\sigma_s = \sigma_x = \sigma_y$). The pointing error PDF can then be written as [11]

$$f_{h_p}(h_p) = \gamma^2 h_p^{\gamma^2 - 1}, \quad 0 < h_p < A_0, \quad \gamma = w_{L_e}/2\sigma_s \tag{2.9}$$

2.2.2 Mechanical System Model

The robotic XYZ Table is a kinematic manipulator capable of moving in 5 DOFs designed and built to experimentally analyze FSO channel outage behavior under pointing error. XYZ Table platform is housed in a 100 x 100 x 100 cm C-Beam Aluminum chassis, as can be seen from the CAD model in Figure 2.1. The DOFs of the system are, motions in X-Y-Z axes, roll (ϕ) and pitch (θ). The actuators of the system consist of 1.2 Nm DC Stepper Motors. Mechanically, the motors are driving 5 mm pitch lead screws that are attached to the platform that moves in 5 corresponding axes.

Figure 2.1: *CAD models of the XYZ Motion Table, Orthograpic View / Side View / Top View.*

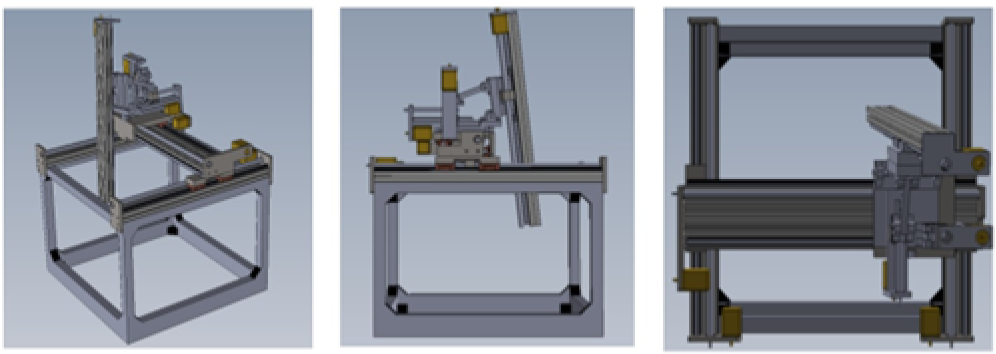

The XYZ Table has 90 cm motion range in all X, Y and Z axes. The resolution of the linear motion is 0.03 cm. For roll and pitch, the angular resolution is 0.1 degrees. Speed of the stepper motors are adjustable, and reliable speed range up to 50 mm/s were observed during experimentation. This designed table is a kinematic manipulator capable of moving in 5 DOFs designed and built to experimentally analyze FSO channel outage behavior under pointing error.

2.3 Controller System Design and Implementation

2.3.1 Overall Architecture of Controller System

Step motor drivers are controlled by Delta DVP28 series PLC's generated PWM and direction signals. The PLC and step motor drivers are housed in a control cabinet as indicated by the block diagram in Figure 2.2. Control of the PLC and motion signals are generated by the Labview software. Data transfer between Labview and the PLC is maintained through the RS-485 communication protocol.

Figure 2.2: *System Block Diagram of the XYZ Motion Table.*

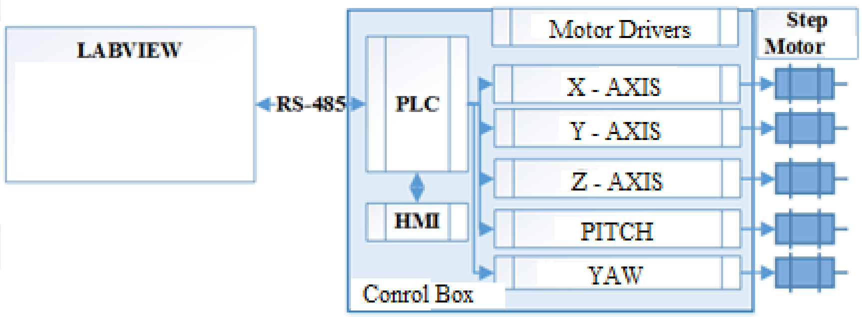

2.3.2 Generation of Stochastic Motion for Experimentation

PLCs have been used in the industrial automation field for the past 5 decades primarily for their durability, robustness and stability. They are, by design, devices that produce predictable outcomes. However, in order to truthfully analyze the pointing error behavior experimentally, the XYZ Table is needed to be moving in a Gaussian fashion were the mean and the standard deviation of the motion can be controlled by the user. Currently the PLCs do not allor the users to generate these type of random variables with the said control parameters.

To overcome this issue, the PLC was used in junction with the Labview software.

A Graphical User Interface (GUI) was developed on Labview where the user can input the desired mean and standard deviation of the Gaussian motion. The software then generates the corresponding motion coordinates and sends them to the PLC to control the motors. The motion of the end effector was measured by a mechanical ruler with a resolution of 10 µm, and the Gaussian nature of the motion was verified against a theoretical Gaussian distribution.

2.3.3 System Performance

Shown below in Figure 2.3 is the mechanical motion of the XYZ Table in the x axis, compared against a theoretical normal distribution. The stochastic motion coordinates are generated by Labview with the user defined input values of $N(0, 2)$. Since both the horizontal and vertical axes have the same mechanical parts such as the lead screw and the step motor, the experience was only conducted on horizontal axis and is taken to be identical for the vertical axis as well. Labview was used to create 140 path coordinates in a Gaussian fashion and it was observed that the XYZ Table was moving in a controlled Gaussian motion with an RMSE of 0.0125, which is very satisfactory.

Figure 2.3: *Verification the Gaussian Motion of the XYZ Table by a Mechanical Ruler.*

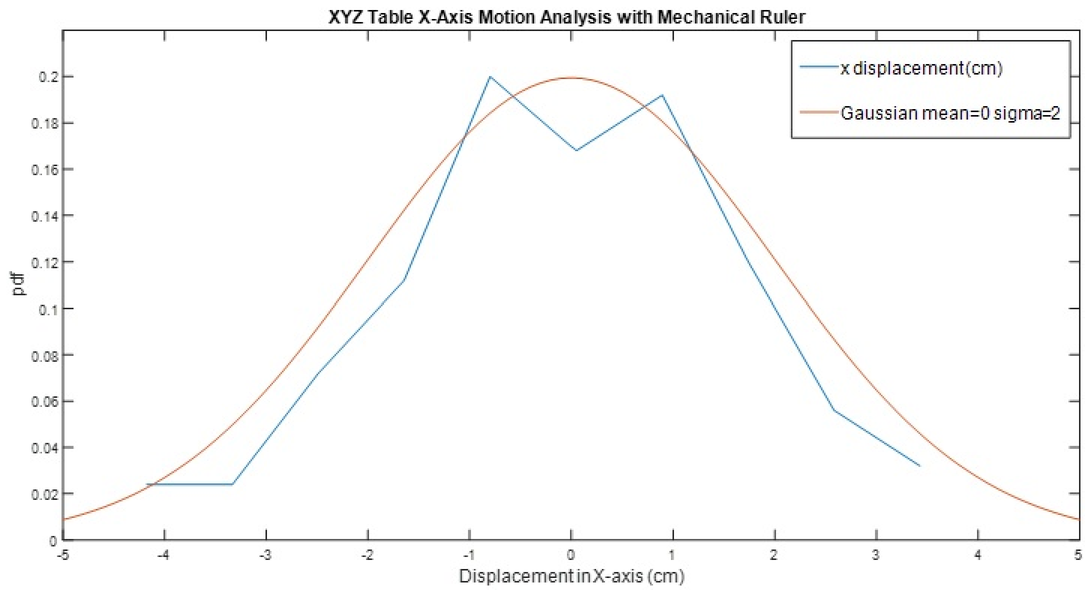

The dip in the middle is cause by the cases where the desired motion is so small that the system did not move and hence the mechanical ruler did not pick up these subtle movements. Nonetheless this lead to a lower data count for displacements close to zero and was expected. It was concluded that the XYZ Table controlled through the Labview software is able to generate random Gaussian motion with the desired mean and standard deviation values.

2.4 Generation of Gaussian Beam

Under the assumption of Gaussian beam profile, the normalized Gaussian intensity profile at the receiver plane by $I_L(r)$ given as [11]

$$I_L(r) = \exp\left(-\frac{2r^2}{w_L^2}\right) \tag{2.10}$$

where w_L is the beam waist, calculated as the radius at e^{-2} of peak intensity profile at the receiver plane at distance L. Leaving the fraction of collected power at perfect alignment to the geometrical loss coefficient, in this study we consider normalized channel coefficient for the ease of measurements and accuracy.

A Gaussian beam profile was created by using a pinhole adjacent to the output of the laser beam. Hypothetically, when the aperture diameter of the pinhole tends to zero the beam profile converges to a Gaussian distribution as it is depicted in Figure 2.4- 2.5 below. Two images of the beam shape are captured in 2D and 3D using beam profiler.

Figure 2.4: *2D View of the Generated Gaussian Beam.*

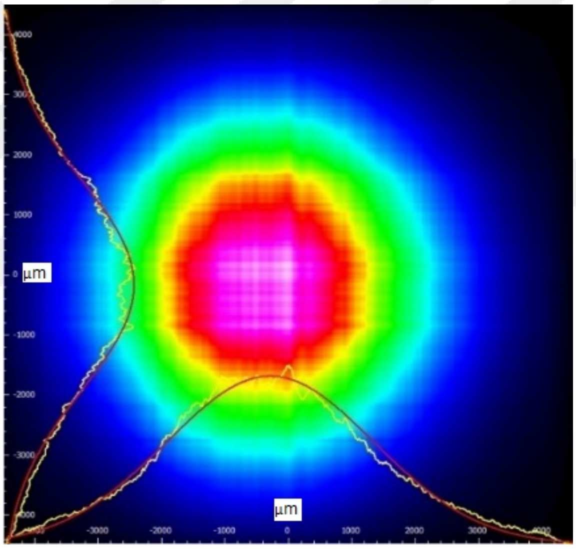

Figure 2.5: *3D View of the Generated Gaussian Beam.*

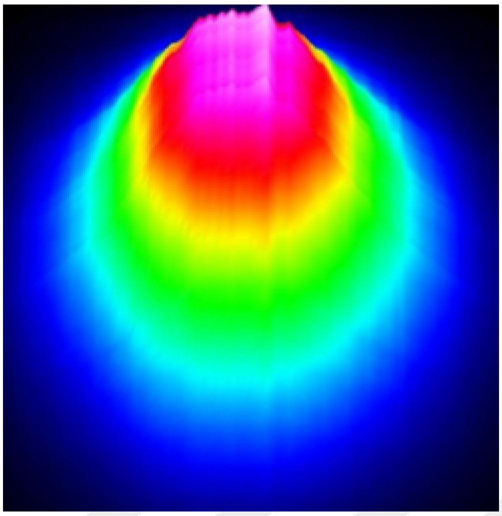

The mapped intensity profile to Cartesian coordinates of x-axis and y-axis are then plotted and this data is used to calculate the Mean Squared Error (MSE) of the profiles. A Gaussian distribution is fitted to the data and the MSE is calculated between the fitted curve and the actual profiles. For the x- and y-axis profiles MSE of 0.0014 and 0.0012 was measured respectively which validates the Gaussian profile of the beam.

2.5 Experimental Verification of Pointing Error

2.5.1 Experimental Setup and Optical Channel Specifications

In order to perform the experiments, the XYZ Table was moved in a Gaussian normal distributed fashion where the mean and the standard deviation of the motion can be dictated by the user. This motion was simultaneously happening as two independent Gaussian distributions with zero mean and varying standard deviation for both axes ($\sigma_s = \sigma_x = \sigma_y$). Shown in Figure 2.6 is the experimental setup with the FSO transmitter laser placed on the XYZ Table.

Figure 2.6: *XYZ Motion Table Setup during an Experiment.*

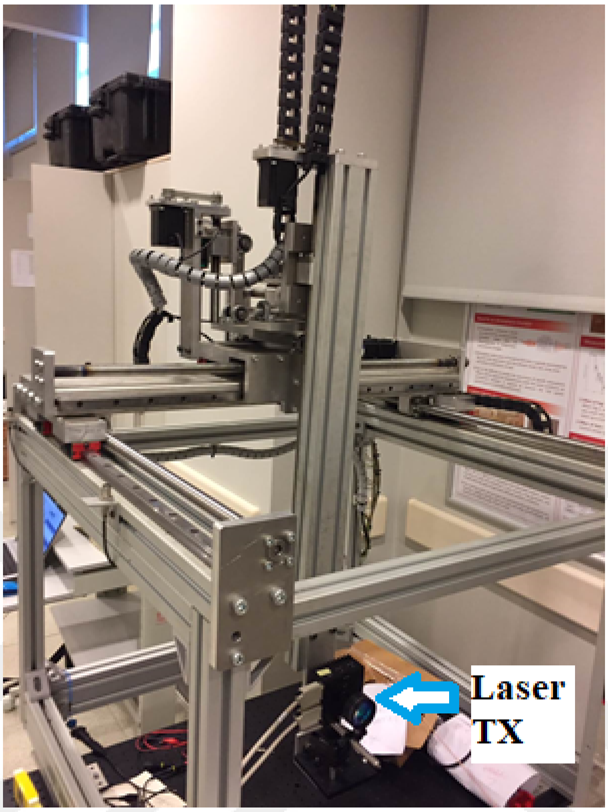

Given in Table 2.1 are the details of the optical link and system configuration.

Table 2.1: *Experiment System Configuration.*

Optical Link	**Experiment System Configuration**	
	Parameter	*Value*
Transmitter (TX)	Wavelength	1550 nm
	Max. Power	5 mW
	Divergence	25 mrad
	Collimated Lens	
Optical Channel	Dimensions	3 x 0.4 x 0.6 m^3
	Link Distance	3 m
Receiver (RX)	Detector Type	BP209-VIS

2.5.2 Measuring Pointing Error in the Presence of Gaussian Distributed Motion

In order to experimentally measure the pointing error, the XYZ Table was moved in a Gaussian random distributed fashion in both X and Z axes, with a mean $\mu = 0$ and standard deviation of σ_s. For both of the axes, the motion coordinates were generated by using the following PDF on Labview.

$$f_x(x) = f_z(\mathrm{z}) = \frac{1}{\sqrt{2\pi{\sigma_s}^2}}\exp\left(-\frac{x^2}{2{\sigma_s}^2}\right) \tag{2.11}$$

Each test was 18000 seconds in duration and was performed with different σ_s values. Received signal was captured and recorded with a 200 Hz detector. Afterwards the PDF of the received power was generated and compared against theoretical model. Shown in Figures 2.7- 2.11 below are experimental results along with theoretical model.

Figure 2.7: *Experimental Verification of Pointing Error Measurement versus Theoretical Model Equation* (2.8) *(σ_s^2 = 0.25 cm).*

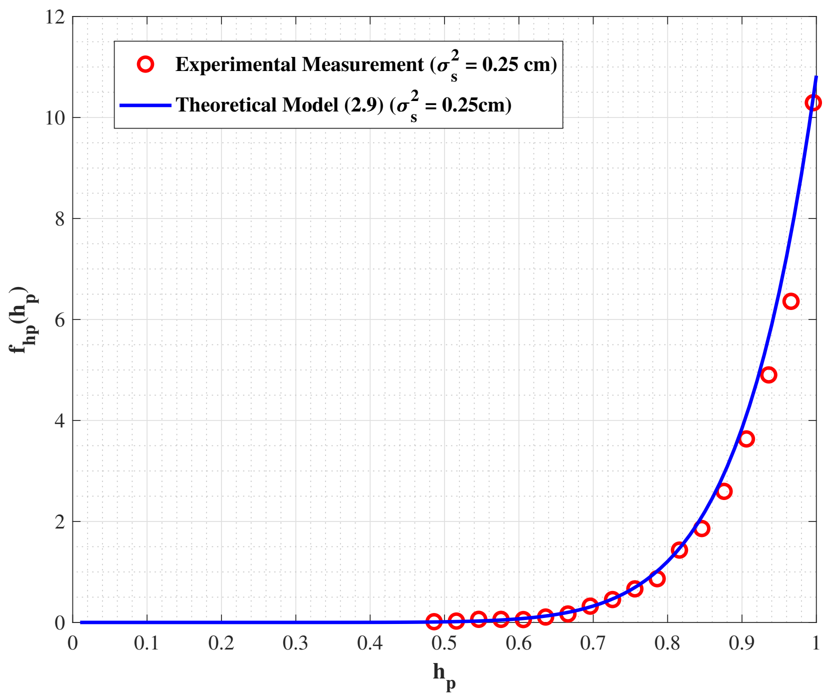

Figure 2.8: *Experimental Verification of Pointing Error Measurement versus Theoretical Model Equation* (2.8) *(σ_s^2 = 0.50 cm).*

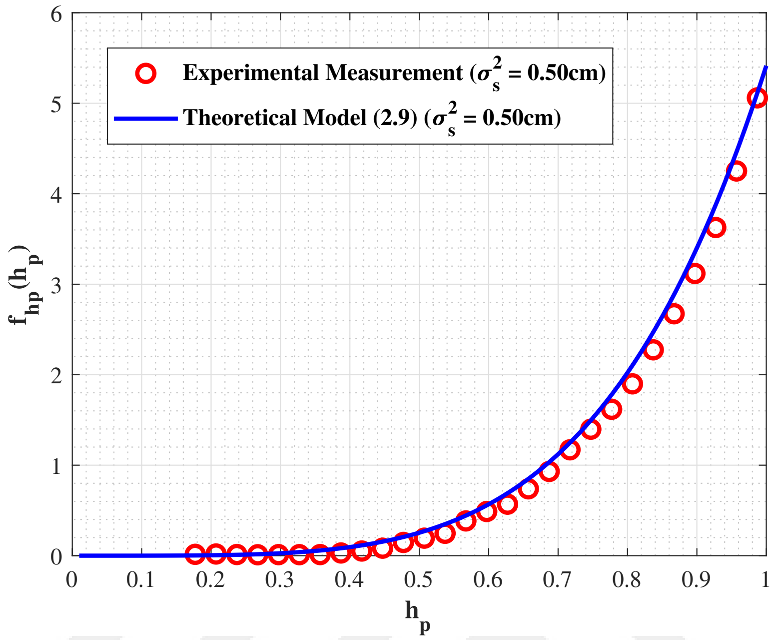

Figure 2.9: *Experimental Verification of Pointing Error Measurement versus Theoretical Model Equation* (2.8) *(σ_s^2 = 0.75 cm).*

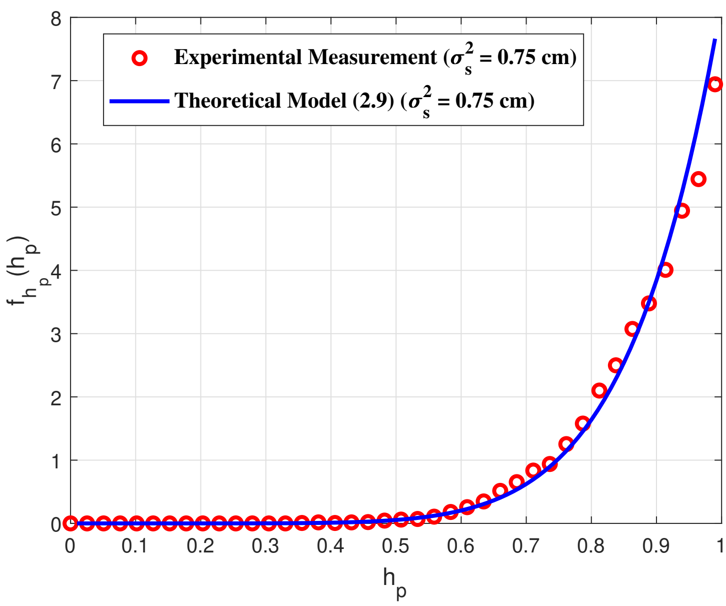

Figure 2.10: *Experimental Verification of Pointing Error Measurement versus Theoretical Model Equation* (2.8) *(σ_s^2 = 1.0 cm).*

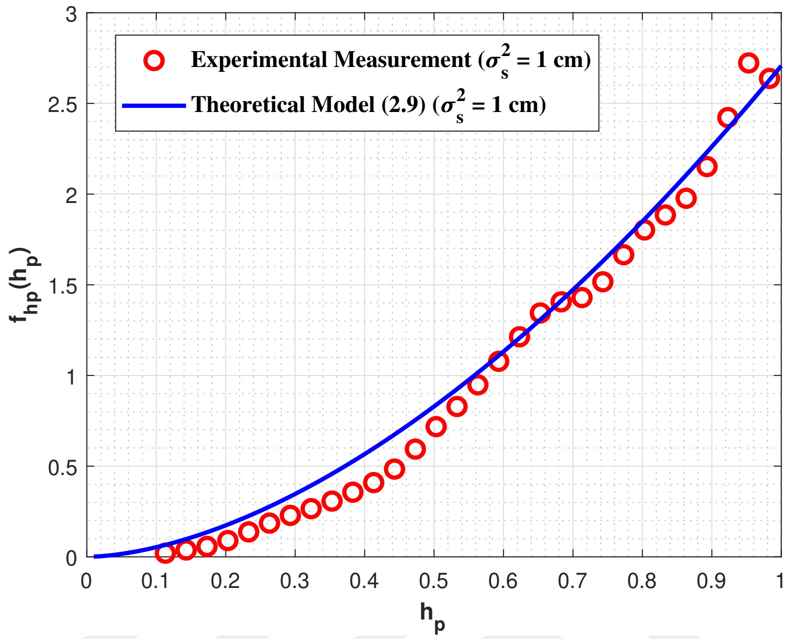

Figure 2.11: *Experimental Verification of Pointing Error Measurement versus Theoretical Model Equation* (2.8) *(σ_s^2 = 1.25 cm).*

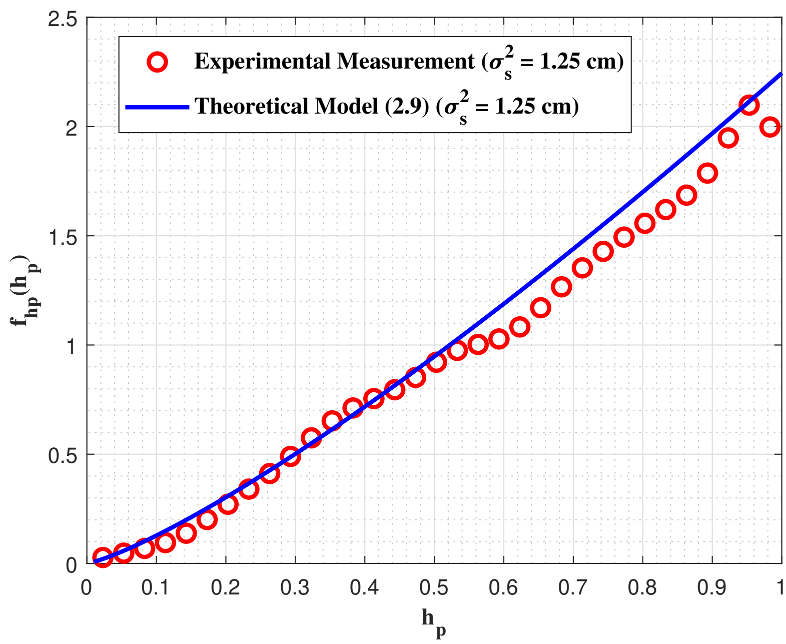

2.6 Results and Discussion

When the FSO transmitter was moved in a Gaussian fashion, it was observed that the pointing error on the received signal closely followed the theoretical model. This was a good verification of the applicability of the XYZ Table in pointing error experiments. The system has proven itself to be capable of producing reliable and repeatable pointing errors in a stochastic yet controllable fashion.

Due to the flexible control architecture of the system, the XYZ table is capable of producing different movements on each axis separately and with this aspect it can test pointing error scenarios that go beyond the currently available models in the literature. It was also seen that using RS-485 protocol along with a PLC was a reliable method for such an application. This designed XYZ Table is a cost efficient, yet a reliable platform for experimental analysis of pointing errors.

3. MODELLING OF POINTING ERRORS IN TERRESTRIAL FSO LINKS CAUSED BY BUILDING SWAY UNDER WIND LOADS

3.1 Introduction

In a terrestrial link, dynamic wind loads, thermal expansion and vibrations cause buildings to sway. High-rise buildings sway in three directions along wind, across wind, and torsional. This results in the misalignment of optical beam at the receiver side and can deteriorate the performance of the link by introducing fluctuations in optical intensity [11].

A pointing error model developed in [11] is widely used in the FSO literature, see e.g. [12, 13, 14], due to its mathematical simplicity. This model assumes a zero mean Gaussian distribution for horizontal and vertical (elevation) displacements with identical standard deviations of motion and zero boresight. In this scenario, the resultant radial displacement becomes Rayleigh distributed. In [12], jitter in vertical and horizontal directions are taken to be non-identical and hence the resultant radial displacement becomes Hoyt (a.k.a Nakagami-q) distributed. In [16], it is shown that the resulting PDF is Beckmann (a.k.a lognormal-Rician) in the presence of nonzero boresight pointing errors. In [14], a unified composite pointing error PDF model is presented with parameters that can be set accordingly to specialize for Rayleigh, Rician, Hoyt, Beckmann, zero mean single-sided Gaussian or non-zero mean single-sided Gaussian distributions depending on jitter and boresight behavior.

In all of the aforementioned works, the variance values of jitter are provided without relating them to the underlying physical phenomena. In practice, jitter occurs due to the sway behavior of a building, and its strength depends on the wind force as well as static forces on the building coupled with its height and shape. None of the earlier studies in the literature relate the pointing error behavior of FSO channel directly to the effects of the wind on the building structure. This study aims to fill this gap. Towards this end, we use civil engineering software for multi-story building analysis and design in conjunction with a wind simulator. We conduct extensive simulations to characterize the behavior of various building sizes under wind loads. Statistical analysis of the building sway motion due to wind demonstrates that the motion is Gaussian in each axis and is in good agreement with current literature. However, it is also observed that the sway motion is dominated by the major axis (horizontal) while the other two are negligible in amplitude when the building is directly facing the wind. This leads to a zero mean single-sided Gaussian distribution. Through non-linear regression, we propose a closed-form expression for the standard deviation as a function of building height, width and wind speed. Afterwards, we present a closed-form expression of the error probability as a function of these environmental parameters and confirm its accuracy through Monte Carlo simulations.

The rest of this chapter is organized as follows: In Chapter 3.2, we discuss the simulation model for building sway due to wind and present standard deviation as a function of building height, width and wind speed based on a comprehensive simulation study. In Chapter 3.3, we provide a closed-form expression for the error rate performance of the FSO link in the presence of pointing errors. In Chapter 3.4, we present numerical results for error probability considering various building heights, widths, and wind speeds. Finally, we conclude in Chapter 3.5.

3.2 Modelling of Building Sway Under Wind

To study buildings' sway behavior under wind, we use ETABS (Extended Three-Dimensional Analysis of Building Systems), a civil engineering software that caters to multi-story building analysis and design [21]. ETABS allows us to create three dimensional models of building structures and analyze them statically and dynamically under external loads such as wind, seismic, and temperature loads.

3.2.1 Wind Force

Wind is a complex meteorological phenomenon comprised of multitude of eddies and moving particles. A turbulent wind flow stochastically varies in time and space [22, 23]. It is a general assumption to set a period of at least 10 minutes for analysis and assume Gaussian distribution for wind [23].

3.2.2 Online Wind Tunnel

In our study, we use Nat-Haz [24], an online wind simulator to generate stationary Gaussian multivariate wind fields.

3.2.3 Building Code Standards

For a realistic simulation, the wind force specifications are taken from the ASCE 7-16 (Associated Criteria for Buildings and Other) code standard, which describes the means for determining extra loads such as the wind on the structural design and specifies force magnitudes to be applied on the building proportional to the wind speed [25]. Using these generated stochastic wind load forces on the building, time series response of the building sway is obtained and eigen type modal analysis is performed with ETABS. As Figure 3.1 illustrates, the wind is assumed to be hitting the building at 0 ° direction. Even though the wind might be composed of multiple vector components with each hitting the building at different angles, in this study we only focused on the wind component that will cause the maximum building sway, which is the wind hitting the building at 0° direction.

Figure 3.1: *Modelling of the Building with the Assumed Wind Direction.*

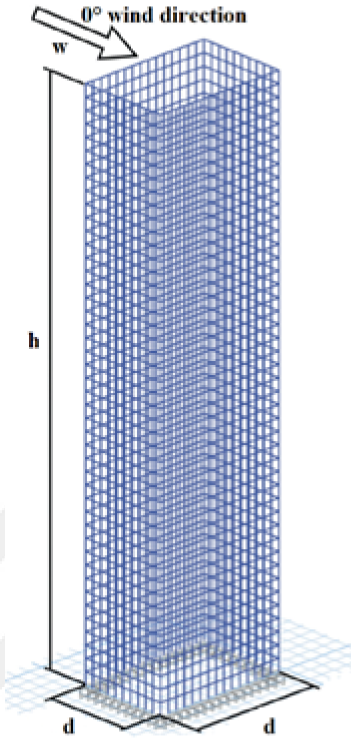

3.2.4 Simulations

In our simulation study, we consider various steel buildings with reinforced concrete at different heights and widths. Specifically, we consider 200 m tall (67 story), 150 m tall (50 story), 120 m tall (40 story), 90 m tall (30 story), 60 m tall (20 story), 30 m tall (10 story) and 3 m tall (1 story) buildings with widths ranging between 5 m to 64 m. As an example, Figure 3.2 shows the three-dimensional displacements of a 24 m x 24 m wide, 150 m tall building under 40 mph wind gusts for a period of 18000 seconds. Quantile-quantile statistical analysis of these simulations confirms the Gaussian nature of building sway in all three dimensions.

Figure 3.2: *Time Series Data of X-Y-Z Positions of 150 m Building Top Under Gaussian Winds with 40 mph Gusts.*

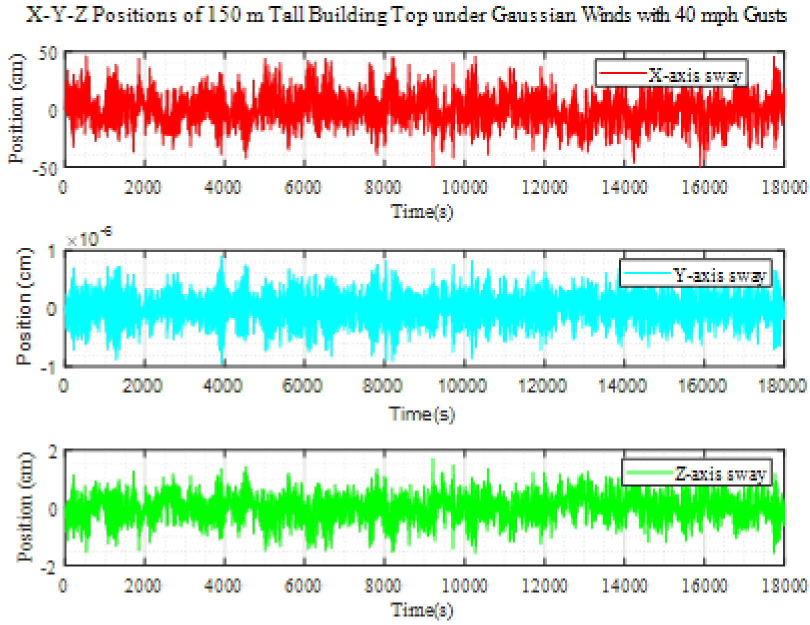

Table 3.1 presents mean and standard deviation of sway motion for all the buildings under consideration, assuming different gusts between 10 to 60 mph. Based on the wind speed, the variance in x axis changes between 1.97×10^{-4} cm and 7.11×10^{-4} cm for a single floor building. As the building height increases, the variance significantly increases. This is simply because a building is a slender structure with its fixation at the ground frame and is, therefore, similar to a cantilever beam in terms of its sway motion behavior. For example, in a building with 67 floors, these values are observed to be in the range of 1.82 cm and 65.5 cm depending on wind speed. For all building heights under consideration, it is observed that the displacement in the z (elevation) axis is two orders of magnitude smaller than the major horizontal axis. The sway in y (back and forth) axis would not have any impact on the transmitted signal because the standard deviation of jitter in y-axis is observed to be at least 7 orders of magnitude small compared to the jitter

values in x-axis for all building heights under the presence of noticeable winds (> 1 mph – Light air winds [26] and higher).

Table 3.1: *Displacement Statistics Under Varying Winds and Building Heights.*

1 Floor Building (3 m)						
Wind (mph)	10	20	30	40	50	60
μ_x (cm)	1.51×10^{-7}	6.03×10^{-7}	1.36×10^{-6}	2.41×10^{-6}	3.77×10^{-6}	5.43×10^{-6}
σ_x (cm)	1.97×10^{-4}	7.89×10^{-4}	1.78×10^{-3}	3.16×10^{-3}	4.94×10^{-3}	7.11×10^{-3}
μ_y (cm)	1.70×10^{-18}	6.81×10^{-18}	1.53×10^{-17}	2.72×10^{-17}	4.26×10^{-17}	8.03×10^{-17}
σ_y (cm)	2.33×10^{-15}	9.31×10^{-15}	2.10×10^{-14}	3.73×10^{-14}	5.82×10^{-14}	1.09×10^{-13}
μ_z (cm)	2.91×10^{-9}	1.16×10^{-8}	2.62×10^{-8}	4.65×10^{-8}	7.27×10^{-8}	1.05×10^{-7}
σ_z (cm)	3.80×10^{-6}	1.52×10^{-5}	3.42×10^{-5}	6.09×10^{-5}	9.51×10^{-5}	1.37×10^{-4}
10 Floor Building (30 m)						
Wind (mph)	10	20	30	40	50	60
μ_x (cm)	4.94×10^{-6}	8.35×10^{-5}	7.76×10^{-5}	2.94×10^{-4}	2.81×10^{-4}	4.84×10^{-4}
σ_x (cm)	1.26×10^{-2}	6.85×10^{-2}	1.06×10^{-1}	2.35×10^{-1}	4.22×10^{-1}	6.04×10^{-1}
μ_y (cm)	2.39×10^{-15}	8.20×10^{-14}	6.37×10^{-14}	9.44×10^{-14}	1.30×10^{-13}	3.35×10^{-13}
σ_y (cm)	1.12×10^{-11}	1.20×10^{-10}	1.75×10^{-10}	1.74×10^{-10}	4.33×10^{-10}	4.99×10^{-10}
μ_z (cm)	3.89×10^{-8}	6.77×10^{-7}	6.38×10^{-7}	2.41×10^{-6}	2.26×10^{-6}	4.01×10^{-6}
σ_z (cm)	1.04×10^{-4}	5.69×10^{-4}	8.89×10^{-4}	1.97×10^{-3}	3.54×10^{-3}	5.09×10^{-3}
20 Floor Building (60 m)						
Wind (mph)	10	20	30	40	50	60
μ_x (cm)	2.24×10^{-5}	3.61×10^{-4}	3.04×10^{-4}	1.29×10^{-3}	1.21×10^{-3}	2.20×10^{-3}
σ_x (cm)	0.59×10^{-2}	3.24×10^{-1}	5.12×10^{-1}	1.14	2.06	2.99
μ_y (cm)	3.30×10^{-14}	4.70×10^{-13}	2.90×10^{-13}	3.20×10^{-12}	1.50×10^{-12}	4.00×10^{-12}
σ_y (cm)	2.03×10^{-10}	1.08×10^{-9}	2.24×10^{-9}	6.96×10^{-9}	7.87×10^{-9}	1.47×10^{-8}
μ_z (cm)	3.60×10^{-6}	5.82×10^{-6}	4.90×10^{-6}	2.10×10^{-5}	2.01×10^{-5}	3.61×10^{-5}
σ_z (cm)	9.80×10^{-4}	5.39×10^{-3}	8.56×10^{-3}	1.91×10^{-2}	3.45×10^{-2}	5.04×10^{-2}
30 Floor Building (90 m)						
Wind (mph)	10	20	30	40	50	60
μ_x (cm)	5.88×10^{-5}	9.60×10^{-4}	9.30×10^{-4}	3.34×10^{-3}	3.01×10^{-3}	5.24×10^{-3}

Continued from previous page						
σ_x (cm)	1.59×10^{-1}	8.78×10^{-1}	1.41	3.13	5.60	8.22
μ_y (cm)	2.90×10^{-13}	1.38×10^{-12}	3.22×10^{-12}	2.84×10^{-11}	9.49×10^{-12}	3.50×10^{-11}
σ_y (cm)	1.51×10^{-9}	3.17×10^{-9}	1.02×10^{-8}	3.28×10^{-8}	3.81×10^{-8}	1.21×10^{-7}
μ_z (cm)	1.37×10^{-6}	2.23×10^{-5}	2.16×10^{-5}	7.75×10^{-5}	7.13×10^{-5}	1.20×10^{-4}
σ_z (cm)	3.79×10^{-3}	2.10×10^{-2}	3.40×10^{-2}	7.55×10^{-2}	1.35×10^{-1}	1.99×10^{-1}
40 Floor Building (120 m)						
Wind (mph)	10	20	30	40	50	60
μ_x (cm)	1.08×10^{-4}	2.27×10^{-3}	1.78×10^{-3}	7.63×10^{-3}	6.23×10^{-3}	1.07×10^{-2}
σ_x (cm)	3.39×10^{-1}	1.93	3.05	6.79	12.4	18.2
μ_y (cm)	9.44×10^{-14}	2.01×10^{-11}	1.22×10^{-11}	3.43×10^{-11}	2.81×10^{-11}	6.62×10^{-12}
σ_y (cm)	2.61×10^{-9}	3.06×10^{-8}	5.20×10^{-8}	7.67×10^{-8}	1.62×10^{-7}	1.40×10^{-7}
μ_z (cm)	3.04×10^{-6}	6.61×10^{-5}	5.11×10^{-5}	2.21×10^{-4}	1.81×10^{-4}	3.03×10^{-4}
σ_z (cm)	9.98×10^{-3}	5.71×10^{-2}	9.08×10^{-2}	2.02×10^{-1}	3.70×10^{-1}	5.47×10^{-1}
50 Floor Building (150 m)						
Wind (mph)	10	20	30	40	50	60
μ_x (cm)	2.26×10^{-4}	4.03×10^{-3}	3.37×10^{-3}	1.27×10^{-2}	1.09×10^{-2}	2.45×10^{-2}
σ_x (cm)	6.30×10^{-1}	3.68	5.73	12.2	23.8	35.7
μ_y (cm)	2.70×10^{-12}	2.66×10^{-11}	1.13×10^{-11}	8.66×10^{-11}	9.36×10^{-11}	1.70×10^{-10}
σ_y (cm)	7.45×10^{-9}	6.37×10^{-8}	1.02×10^{-7}	2.49×10^{-7}	4.47×10^{-7}	6.55×10^{-7}
μ_z (cm)	7.30×10^{-6}	1.31×10^{-4}	1.09×10^{-4}	4.11×10^{-4}	3.49×10^{-4}	8.01×10^{-4}
σ_z (cm)	2.10×10^{-2}	1.23×10^{-1}	1.93×10^{-1}	4.48×10^{-1}	8.03×10^{-1}	1.21
67 Floor Building (201 m)						
Wind (mph)	10	20	30	40	50	60
μ_x (cm)	1.11×10^{-3}	4.42×10^{-3}	9.96×10^{-3}	1.77×10^{-2}	2.77×10^{-2}	3.98×10^{-2}
σ_x (cm)	1.82	7.28	16.4	29.1	45.5	65.5
μ_y (cm)	9.27×10^{-10}	3.71×10^{-9}	8.34×10^{-9}	1.48×10^{-8}	2.32×10^{-8}	3.34×10^{-8}
σ_y (cm)	1.61×10^{-6}	6.42×10^{-6}	1.44×10^{-5}	2.57×10^{-5}	4.01×10^{-5}	5.78×10^{-5}
μ_z (cm)	3.98×10^{-5}	1.59×10^{-4}	3.58×10^{-4}	6.37×10^{-4}	9.96×10^{-4}	1.43×10^{-3}
σ_z (cm)	6.76×10^{-2}	2.70×10^{-1}	6.08×10^{-1}	1.08	1.69	2.43

Table 3.2 presents the effect of building width on building sway motion. The amount of displacement is observed to be inversely proportional to the building width. This effect is due to the fact that when the building gets more slender, it tends to sway more like a cantilever beam. However, the decrease in the variance with the increase in the width is quite small.

Table 3.2: *Effect of Building Width on the Sway Motion. A 150 m Building is Considered and 20 mph Wind Gusts are Assumed.*

Building Width	μ_x (cm)	σ_x (cm)
24 m × 24 m	4.03×10^{-3}	3.68
32 m × 32 m	2.98×10^{-3}	2.71
40 m × 40 m	2.37×10^{-3}	2.16
48 m × 48 m	1.97×10^{-3}	1.79
56 m × 56 m	1.69×10^{-3}	1.54

3.2.5 Derivation of Closed-form Expression for Building Sway

In the following we present a closed-form expression for the standard deviation of major axis sway motion using non-linear regression methods. In addition to the results presented in Tables 3.1- 3.2, we generated additional simulation data for slower wind speeds (0 mph to 5 mph), building widths in the range of 24 m - 64 m and building heights in the range of 3 m - 201 m. By analysis of the collected data, it is evident that the standard deviation of building sway is directly proportional with building height (h) and wind speed (w); and inversely proportional with its width (d). Accordingly, we considered a function in the form of

$$\sigma_x = \left(\frac{a_1 h^{b_1} a_2 w^{b_2} + a_3 y^{b_3}}{a_4 d^{b_4}} \right)^5 \tag{3.1}$$

where building height and wind speed appear at the numerator, and building width is at the denominator. In order to cater to cases with no wind, a unitless ratio of building height over width (y) was also added to the numerator. Using non-linear regression on this formulation, we obtain the related coefficients $a_1 = 0.0513$,$a_2 = 0.8284$,$a_3 = 0.0008$,$a_4 = 1.4032$,$b_1 = 0.5375$,$b_2 = 0.4862$,$b_3 = 0.0011$,$b_4 = 0.1840$.

To demonstrate its accuracy, we present the proposed expression in Equation (3.1) with respect to building height for various wind speeds in Figure 3.3, assuming a 24 m wide building. It is observed that the proposed expression is in good match with the simulation results. As a metric of accuracy, Root Mean Squared Error (RMSE) is adopted and average values of 0.1515-0.1716 are obtained for wind speeds of 10-60 mph. The RMSE increases slightly with building height and wind speed. Similarly, Figure 3.4 shows the simulation results for a 32 m wide building in which the diminishing effect of increasing building width on building sway standard deviation is more noticeable.

Figure 3.3: *The Proposed Closed-form Expression in Equation* (3.1) *versus Simulated Standard Deviation. A 24 m Wide Building is Considered.*

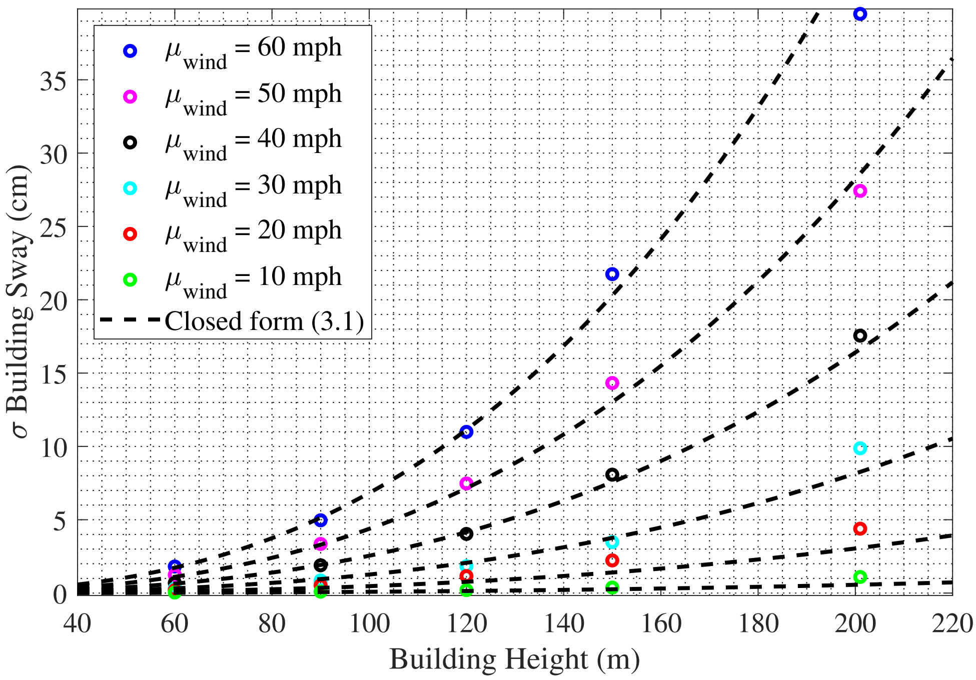

Figure 3.4: *The Proposed Closed-form Expression in Equation* (3.1) *versus Simulated Standard Deviation. A 32 m Wide Building is Considered.*

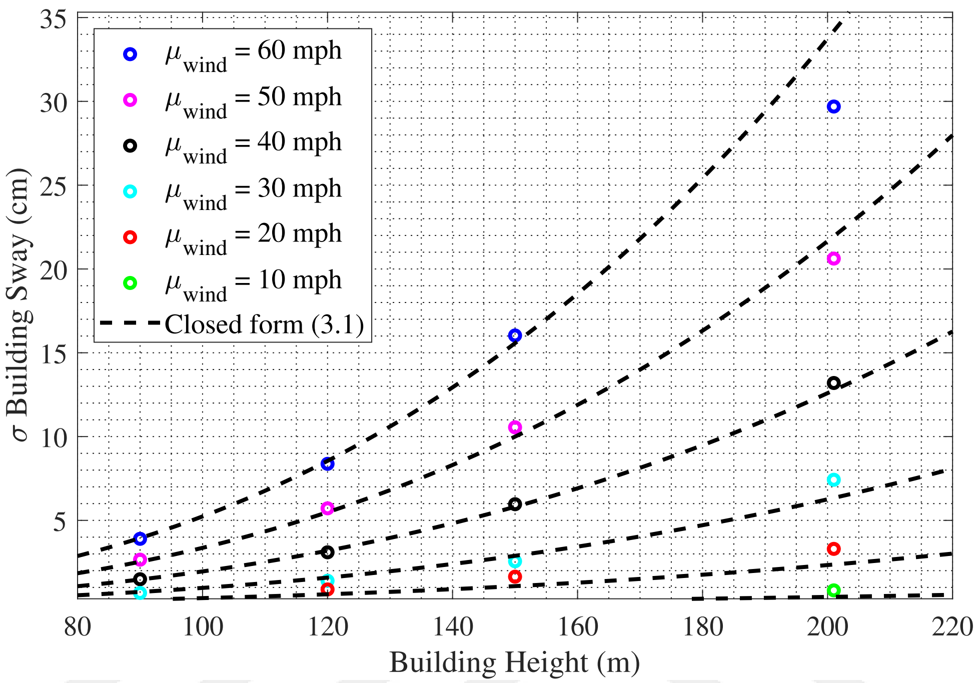

The validity of the derived expression Equation (3.1) was also checked against other publications that have studied the sway behavior of tall buildings under wind loads. In [28], experimental measurements of wind-induced response of a 108 m tall, 13 m wide steel tower is presented. For a wind speed value of 10 m/s, a standard deviation $\sigma_x = 1.1 \times 10^{-3}$ was measured. For the same parameters, the derived expression in Equation (3.1) yields $\sigma_x = 1.28 \times 10^{-3}$ which is in good match with the experimental result. We conjecture that the slight difference might arise from the fact that a steel tower is hollow and air can pass through it more easily causing a smaller sway. Whereas the building model used in our simulations is a closed structure from 4 sides and therefore experiences more force due to wind. In [27], the authors present the sway motion data for a 66-story, 234 m building. The motion of the building top is recorded by using GPS sensors installed at the rooftop and the data is captured during a day of regular winds ranging from 9 m/s to 14 m/s. In this work, the sway data for the building is given for the average winds of 11 m/s and their experimental data indicates a sigma of $\sigma_x = 4.71 \times 10^{-3}$. Using Equation (3.1), we obtain $\sigma_x = 5.23 \times 10^{-3}$ for the same wind and building values. The difference might arise from the fact the building studied in the mentioned work has a slightly rectangular shape, with a width to length ratio of 0.82, and therefore tends to sway less than the square model assumed in our model. However, the results are still within reasonable limits and is a good indicator that Equation (3.1) is in good match with the real world experimental data. In [28], the authors present the experimental sway data of the 384 m tall Di Wang Tower located in Shenzhen City, China. The sway behavior was captured for the average wind speed of 11.5 m/s. The sway data in this study suggests $\sigma_x = 6.35 \times 10^{-3}$ whereas (1) yields $\sigma_x = 7.48 \times 10^{-3}$ for the given building dimensions and wind speed. The difference again is likely to emanate from the fact that the building does not have a perfect square shape, and has a more rectangular base with a width to length ratio of 0.52. However, the value we obtain by Equation (3.1) is still within reasonable limits with respect to the experimental data.

3.2.6 Error Performance in the Presence of Pointing Error

We consider an FSO link with a transmission distance of and a circular receive aperture with radius . The fraction of the power collected by the receiver is obtained as

$$h_p\left(\mathbf{r};z\right) = \int\limits_A I_{beam}\left(\rho - \mathbf{r};z\right) d\rho \tag{3.2}$$

where $r = \|\mathrm{r}\| = \sqrt{r_x^2 + r_y^2}$ is the radial vector from the detector to beam center, ρ is the radial vector from beam center, and $A = \pi a^2$ is the circular detection area. Here $I_{beam}(.)$ represents the normalized spatial distribution of transmitted intensity. For a Gaussian beam, it is given by [11]

$$I_{beam}\left(\rho;z\right)=A_0\exp\left(-\frac{2\|\rho\|^2}{w_L^2}\right) \tag{3.3}$$

where w_L is the beam waist and A_0 is the fraction of the collected power at $r=0$. It can be calculated as $A_0=[\text{erf}\,(v)]^2$ where $v=(\sqrt{\pi}a)/(\sqrt{2}w_L)$ is the ratio between circular aperture radius and beam waist. Under the assumption that the radial distance is located along the primary axis, the pointing error can be approximated as [11]

$$h_p\left(r;z\right)\approx A_0\text{exp}\left(-\frac{2r^2}{w_{L_{eq}}^2}\right) \tag{3.4}$$

where $w_{L_{eq}}$ is the equivalent beam width and defined as [11]

$$w_{L_{eq}}^2=w_L^2\frac{\sqrt{\pi}\text{erf}\,(v)}{2v\text{exp}\,(-v^2)} \tag{3.5}$$

Based on the comprehensive simulations discussed in the previous section, we have observed that the sway motion is dominated by the major axis (horizontal) while the other two are negligible in amplitude when the building is directly facing the wind. This indicates that zero mean single-sided Gaussian distribution is a practical model to model pointing error. Therefore, the PDF of h_p can be expressed as [29]

$$f_{h_p}\left(h_p\right)=\frac{\frac{w_{Leq}}{2\sigma_x}h_p^{\left(\frac{w_{Leq}}{2\sigma_x}\right)^2-1}}{A_0^{\left(\frac{w_{Leq}}{2\sigma_x}\right)^2}\sqrt{\pi\ln\left(\frac{A_0}{h_p}\right)}} \tag{3.6}$$

where σ_x is the standard deviation of motion in the x-axis. It can be noticed that for negligible pointing errors, the term $w_{L_{eq}}/2\sigma_x$ approaches to infinity.

We assume Intensity-Modulation and Direct-Detection (IM/DD) system with On-Off Keying (OOK) modulation. The receive signal is given by

$$y = hRx + z \tag{3.7}$$

Where R is the detector responsivity, x is the transmitted OOK signal, z is Additive White Gaussian Noise (AWGN) and h is the fading channel coefficient due to pointing errors. The transmitted signal symbols are drawn from OOK constellation equiprobably such that $x \in \{0, 2P_t\}$, where P_t is the average transmitted optical power. The conditional BER for an IM/DD system with OOK is given by [12]

$$Pb\left(e|h\right) = \frac{1}{2}\mathrm{erfc}\left(\frac{P_t h}{\sigma_N}\right) \tag{3.8}$$

Therefore the average BER can be obtained by averaging Equation (3.8) over the pdf of h

$$P_b\left(e\right) = \int\limits_0^{A_0} \frac{w_{Leq} h_p{}^{\frac{w_{Leq}^2}{4\sigma_x{}^2}-1}}{2\sigma_x A_0{}^{\frac{w_{Leq}^2}{4\sigma_x{}^2}} \sqrt{\ln(A_0/h_p)\pi}} \frac{1}{2}\mathrm{erfc}(\frac{P_t h_p}{\sigma_N}) dh_p \tag{3.9}$$

By collecting the constants out of the integral, Equation (3.9) can be written as

$$P_b\left(e\right) = C \int\limits_0^{A_0} \frac{h_p{}^{B-1}}{\sqrt{\ln\left(A_0/h_p\right)}} \mathrm{erfc}\left(Eh_p\right) dh_p \tag{3.10}$$

where $C = w_{L_{eq}} \Big/ 4\pi\sigma_x A_0{}^B$, $B = w_{L_{eq}}^2 \Big/ 4\sigma_x{}^2$, $E = P_t/\sigma_N$

In order to simplify Equation (3.10), we approximated the denominator of the integrand as a weighted two-term exponential function as

$$\left(\ln\left(A_0/h_p\right)\right)^{-1/2} = a\exp\left(bh_p/A_0\right) + c\exp\left(dh_p/A_0\right) \tag{3.11}$$

where $a = 0.03149$, $b = -4.158\text{x}10^{-5}$, $c = 0.306$, $d = -3.956\text{x}10^{-7}$ were obtained through data fitting. Further using the approximation [30] we obtain

$$\operatorname{erfc}(x) \approx 1/6 \exp\left(-x^2\right) + 1/2 \exp\left(-4x^2/3\right) \tag{3.12}$$

$$\begin{aligned}
P(e) = {} & \underbrace{C\frac{a}{6}\int_0^{A_0}\left(e^{b\left(\frac{h_p}{A_0}\right)-(E\gamma h_p)^2}\right){h_p}^{B-1}dh_p}_{P_1(e)} \\
& \underbrace{+C\frac{c}{6}\int_0^{A_0}\left(e^{d\left(\frac{h_p}{A_0}\right)-(E\gamma h_p)^2}\right){h_p}^{B-1}dh_p}_{P_2(e)} \\
& \underbrace{+\mathrm{C}\frac{a}{2}\int_0^{A_0}\left(e^{b\left(\frac{h_p}{A_0}\right)-\left(\frac{4}{3}(E\gamma h_p)^2\right)}\right){h_p}^{B-1}dh_p}_{P_3(e)} \\
& \underbrace{+C\frac{c}{2}\int_0^{A_0}\left(e^{d\left(\frac{h_p}{A_0}\right)-\left(\frac{4}{3}(E\gamma h_p)^2\right)}\right){h_p}^{B-1}dh_p}_{P_4(e)}
\end{aligned} \tag{3.13}$$

The integration steps for each of the terms in Equation (3.13) are provided below. The integrands are similar in form and only differ by one or two terms. In order to simplify the derivation, we first define the following functions

$$v(x,y) = E\gamma y - x/(2A_0E\gamma) \tag{3.14}$$

$$w(x,y) = 2E\gamma y\Big/\sqrt{3} - \sqrt{3}x\Big/(4E\gamma A_0) \tag{3.15}$$

$$n(x,y) = 0.5Cx\left(\sqrt{3}\Big/2E\gamma\right)^B \exp\left(y/2A_0\right) \tag{3.16}$$

$$m(x,y) = C\frac{x}{6}\left(\frac{1}{E\gamma}\right)^B \exp\left(-E^2\gamma^2\left[-\left(\frac{y}{2A_0E^2\gamma^2}\right)^2\right]\right) \tag{3.17}$$

First term in Equation (3.13) is given as

$$P_1\left(e\right) = C\frac{a}{6}\int\limits_0^{A_0} {h_p}^{B-1}\exp\left(\frac{b}{A_0}h_p - E^2\gamma^2 h_p^2\right)dh_p \tag{3.18}$$

After the constants are taken out of the integral and some re-arrangements, Equation (3.18) becomes

$$\begin{aligned} P_1\left(e\right) = C\tfrac{a}{6}\exp\left(-E^2\gamma^2\left[-\left(\tfrac{b}{2A_0E^2\gamma^2}\right)^2\right]\right) \\ \times\int\limits_0^{A_0} {h_p}^{B-1}\exp\left(-\left(E\gamma h_p - \tfrac{b}{2A_0E\gamma}\right)^2\right)dh_p \end{aligned} \tag{3.19}$$

Letting $u_1 = v\left(b, h_p\right)$, Equation (3.19) can be written as

$$P_1\left(e\right) = C_1 \int\limits_{u_{1_{\min}}}^{u_{1_{\max}}} \left(u_1 + C_2\right)^{B-1}\exp\left(-u_1^2\right)du \tag{3.20}$$

where $C_1 = (a, b)$, $C_2 = v\left(-b, 0\right)$, $u_{1_{\min}} = v\left(b, 0\right)$, $u_{1_{\max}} = v\left(b, A_0\right)$. For high SNR, we have $C_2 \ll 1$, and hence $C_2u_1^{-1} \ll 1$ also holds true. Using binomial expansion and truncating the series to the first term for approximation as $\left(1+x\right)^n \approx 1 + nx$, we can rewrite Equation (3.20) as

$$\begin{aligned} P_1\left(e\right) = C_1 \int\limits_{u_{1_{\min}}}^{u_{1_{\max}}} u_1^{B-1}\exp\left(-u_1^2\right)du \\ +C_1\,C_2\,\left(B-1\right)\int\limits_{u_{1_{\min}}}^{u_{1_{\max}}} u_1^{B-2}\exp\left(-u_1^2\right)du \end{aligned} \tag{3.21}$$

Using [31] on both terms of Equation (3.20), the expression can be written as

$$\begin{aligned} P_1\left(e\right) = C_1\left[-\tfrac{1}{2}u_1^B(u_1^2)^{-\frac{B}{2}}\Gamma\left(\tfrac{B}{2}, u_1^2\right)\Big|_{u_{1_{\min}}}^{u_{1_{\max}}}\right] \\ +C_1\,C_2\,\left(B-1\right)\left[-\tfrac{1}{2}u_1^{B-1}(u_1^2)^{\frac{1}{2}-\frac{B}{2}}\Gamma\left(\tfrac{B-1}{2}, u_1^2\right)\Big|_{u_{1_{\min}}}^{u_{1_{\max}}}\right] \end{aligned} \tag{3.22}$$

By following the same derivation steps, the closed-form expression of the second term in Equation (3.13) is obtained as

$$\begin{aligned} P_2(e) = C_3 & \left[-\tfrac{1}{2} {u_3}^B (u_3^2)^{-\frac{B}{2}} \Gamma\left(\tfrac{B}{2}, {u_3}^2\right) \Big|_{u_{3_{\min}}}^{u_{3_{\max}}} \right] \\ & + C_3\, C_4\ (B-1) \left[-\tfrac{1}{2} {u_3}^{B-1} (u_3^2)^{\frac{1}{2}-\frac{B}{2}} \Gamma\left(\tfrac{B-1}{2}, u_3^2\right) \Big|_{u_{3_{\min}}}^{u_{3_{\max}}} \right] \end{aligned} \tag{3.23}$$

where $u_3 = v\,(d, h_p)$, $u_{3_{\min}} = v\,(d, 0)$, $u_{3_{\max}} = v\,(d, A_0)$, $C_3 = m\,(c, d)$, $C_4 = v\,(-d, 0)$. Similarly, closed-form expression of $P_3\,(e)$ is obtained as

$$\begin{aligned} P_3\,(e) = C_5 & \left[-\tfrac{1}{2} u_5^B (u_5^2)^{-\frac{B}{2}} \Gamma\left(\tfrac{B}{2}, u_5^2\right) \Big|_{u_{5_{\min}}}^{u_{5_{\max}}} \right] \\ & + C_5\, C_6\ (B-1) \left[-\tfrac{1}{2} u_5^{B-1} (u_5^2)^{\frac{1}{2}-\frac{B}{2}} \Gamma\left(\tfrac{B-1}{2}, u_5^2\right) \Big|_{u_{5_{\min}}}^{u_{5_{\max}}} \right] \end{aligned} \tag{3.24}$$

where $u_5 = w\,(b, h_p)$, $u_{5_{\min}} = w\,(b, 0)$, $u_{5_{\max}} = w\,(b, A_0)$, $C_5 = n\,(a, b)$ and $C_6 = w\,(-b, 0)$. Finally, $P_4\,(e)$ is given by

$$\begin{aligned} P_4\,(e) = C_7 & \left[-\tfrac{1}{2} u_7^B (u_7^2)^{-\frac{B}{2}} \Gamma\left(\tfrac{B}{2}, u_4^2\right) \Big|_{u_{7_{\min}}}^{u_{7_{\max}}} \right] \\ & + C_7\, C_8\ (B-1) \left[-\tfrac{1}{2} u_7^{B-1} (u_7^2)^{\frac{1}{2}-\frac{B}{2}} \Gamma\left(\tfrac{B-1}{2}, u_7^2\right) \Big|_{u_{7_{\min}}}^{u_{7_{\max}}} \right] \end{aligned} \tag{3.25}$$

where $u_7 = w\,(d, h_p)$, $u_{7_{\min}} = w\,(d, 0)$, $u_{7_{\max}} = w\,(d, A_0)$, $C_7 = n\,(c, d)$ and $C_8 = w\,(-d, 0)$

Combining Equations (3.22)- (3.25), the average BER is obtained as

$$
\begin{aligned}
P_b\left(e\right) = C_1 & \left[-\tfrac{1}{2}u^B (u_1^2)^{-\frac{B}{2}} \Gamma\left(\tfrac{B}{2}, u_1^2\right)\Big|_{u_{\min}}^{u_{\max}} \right] + \ldots \\
& C_1 C_2 \left(B-1\right) \left[-\tfrac{1}{2}u_1^{B-1} (u_1^2)^{\frac{1}{2}-\frac{B}{2}} \Gamma\left(\tfrac{B-1}{2}, u_1^2\right)\Big|_{u_{\min}}^{u_{\max}} \right] + \ldots \\
& C_3 \left[-\tfrac{1}{2}{u_2}^B (u_2^2)^{-\frac{B}{2}} \Gamma\left(\tfrac{B}{2}, u_2^2\right)\Big|_{u_{2_{\min}}}^{u_{2\max}} \right] + \ldots \\
& C_3 C_4 \left(B-1\right) \left[-\tfrac{1}{2}{u_2}^{B-1} (u_2^2)^{\frac{1}{2}-\frac{B}{2}} \Gamma\left(\tfrac{B-1}{2}, u_2^2\right)\Big|_{u_{2_{\min}}}^{u_{2\max}} \right] + \ldots \\
& C_5 \left[-\tfrac{1}{2}u_3^B (u_3^2)^{-\frac{B}{2}} \Gamma\left(\tfrac{B}{2}, u_3^2\right)\Big|_{u_{3_{\min}}}^{u_{3\max}} \right] + \ldots \\
& C_5 C_6 \left(B-1\right) \left[-\tfrac{1}{2}u_3^{B-1} (u_3^2)^{\frac{1}{2}-\frac{B}{2}} \Gamma\left(\tfrac{B-1}{2}, u_3^2\right)\Big|_{u_{3_{\min}}}^{u_{3\max}} \right] + \ldots \\
& C_7 \left[-\tfrac{1}{2}u_4^B (u_4^2)^{-\frac{B}{2}} \Gamma\left(\tfrac{B}{2}, u_4^2\right)\Big|_{u_{4_{\min}}}^{u_{4\max}} \right] + \ldots \\
& C_7 C_8 \left(B-1\right) \left[-\tfrac{1}{2}u_4^{B-1} (u_4^2)^{\frac{1}{2}-\frac{B}{2}} \Gamma\left(\tfrac{B-1}{2}, u_4^2\right)\Big|_{u_{4_{\min}}}^{u_{4\max}} \right]
\end{aligned}
\tag{3.26}
$$

Rearranging this as a summation, we obtain the final from as

$$
P_b\left(e\right) = \sum_{i=1,3,5,7} \begin{array}{l} C_i \left[-\tfrac{1}{2}u^B (u_i^2)^{-\frac{B}{2}} \Gamma\left(\tfrac{B}{2}, u_i^2\right)\Big|_{u_{i_{\min}}}^{u_{i_{\max}}} \right] \\ +C_i\, C_{i+1}\, \left(B-1\right) \left[-\tfrac{1}{2}u_i^{B-1} (u_i^2)^{\frac{1}{2}-\frac{B}{2}} \Gamma\left(\tfrac{B-1}{2}, u_i^2\right)\Big|_{u_{i_{\min}}}^{u_{i_{\max}}} \right] \end{array}
\tag{3.27}
$$

3.3 Numerical Results

In this section, we present numerical results for the BER performance. Unless otherwise noted, we assume $z = 1$ km and $R = 1$ in all our simulations.

In Figure 3.5, we investigate the effect of pointing error on the BER. We assume an aperture radius $a = 1$ cm and beam width $w_L = 15$ cm. We present BER assuming that the standard deviation of motion takes values in the range of $\sigma_x = 7$ cm to 25 cm, see Table 3.1 for tall buildings (> 100 m). As the pointing error increases, BER performance significantly deteriorates. For example, to achieve a BER of 10^{-4} , SNR of 13 dB is required for $\sigma_x = 7$ cm, a typical value for a building with 120 m height and 24 m width experiencing 40 mph winds. The required SNR increases to 34 dB for $\sigma_x = 25$ cm, a typical value for a building with 200 m height and 24 m width experiencing 35 mph winds. In the figure, we have further included the numerical computation of the integral in Equation (3.9) as a benchmark to demonstrate the accuracy of the derived approximate expression in Equations (3.27). It tends to converge to the simulation results for reasonable SNR rates.

Figure 3.5: *Effect of Beamwidth on BER. A Constant Normalized Jitter Standard Deviation $\sigma_x/a = 10$ is assumed.*

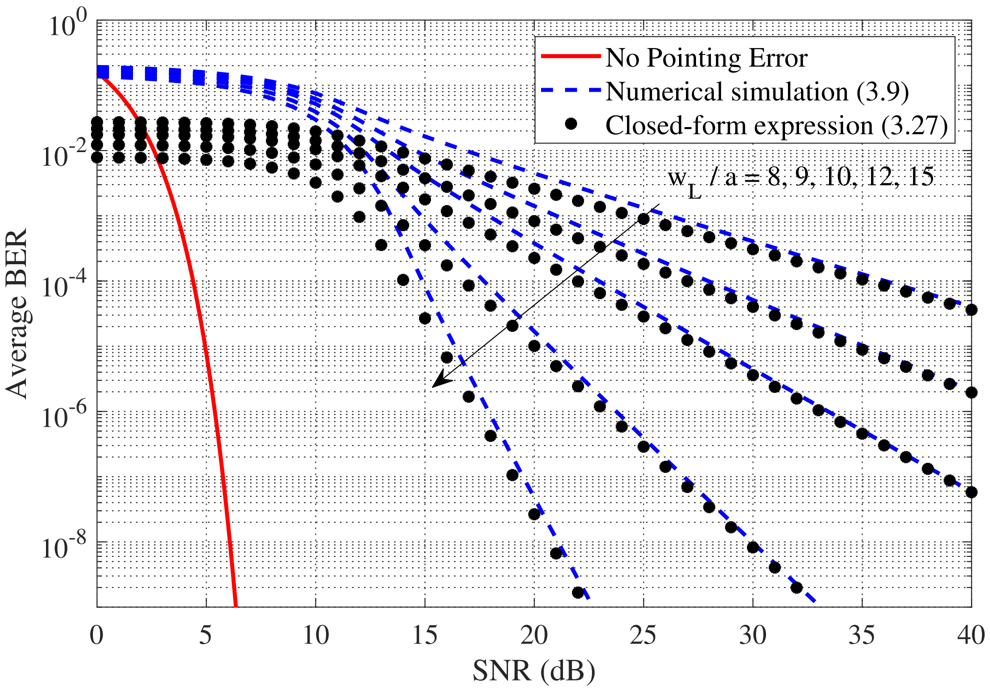

In Figure 3.6, we investigate the effect of beam widht on the BER. We consider a constant normalized jitter standard deviation $\sigma_x/a = 10$. The normalized beam width w_L/a is varied between 8 and 15. As the laser divergence angle, therefore beamwidth, increases, there is a noticeable change in the BER performance. For instance when w_L/a almost doubles from 8 to 15, the required SNR to achieve a BER of 10^{-4} decreases by 20 dB. This result is expected since as the beam gets larger, more chances that the receiver aperture will be getting the vast majority of the transmitted optical power despite misalignments causing pointing errors.

Figure 3.6: *Effect of Pointing Error on BER.* $a = 1$ *cm and* $w_L = 15$ *cm are assumed.*

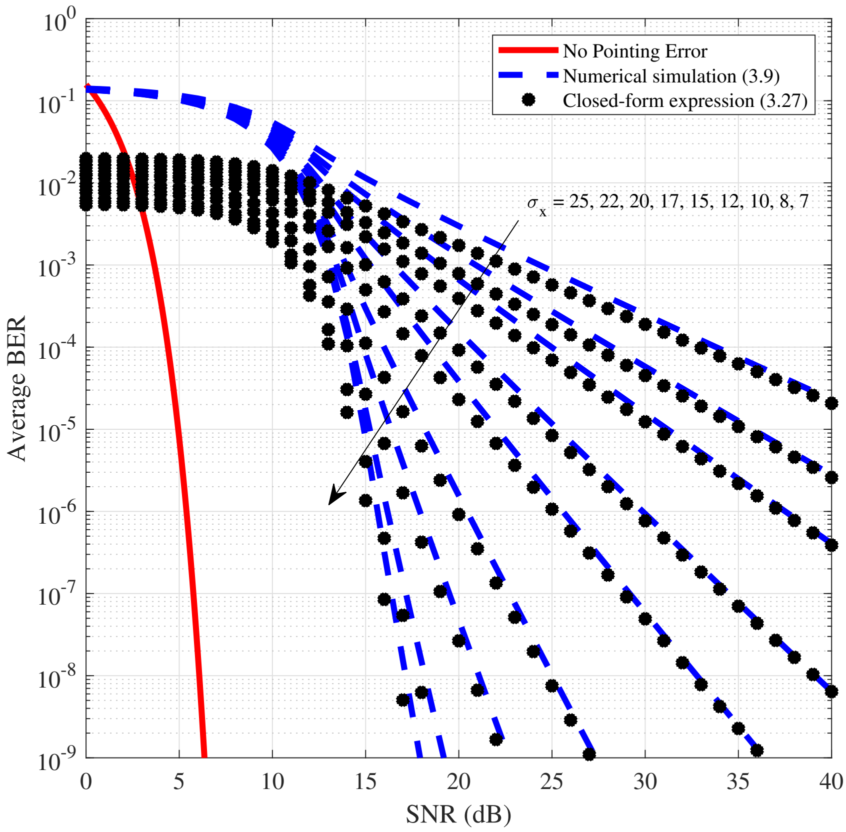

In Figure 3.7, we investigate the effect of wind speeds on the BER. We consider a building with a height $h = 200$ m and width $d = 24$ m and assume an aperture radius $a = 1$ cm, beam width $w_L = 5$ cm. The wind speed is varied in the range of 15 to 25 mph. With the increasing wind speeds from light to strong winds, significant changes in the BER are observed. For instance, to achieve a BER of 10^{-4} , SNR of 16 dB is required for $w = 18$ mph. This increases to 39 dB for $w = 25$ mph.

Figure 3.7: *Effect of Wind Speed on the BER.* $h = 200$ *m,* $d = 24$ *m,* $a = 1$ *cm and* $w_L = 5$ *cm are assumed.*

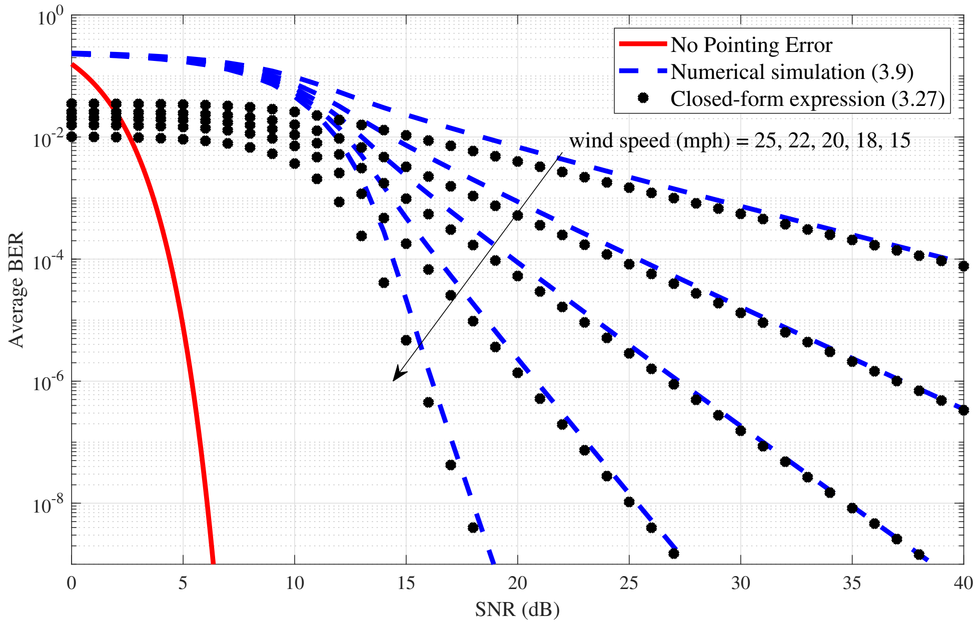

In Figure 3.8, we investigate the effect of building heights on the BER. We consider a 24 m wide building and assume wind speed $w = 30$ mph, an aperture radius $a = 1$cm and beam width $w_L = 5$cm. The building height is varied between $h = 100$ m to 170 m. It is observed that as the building height increases, the BER deteriorates. For example, to achieve a BER of 10^{-4}, SNR of 13 dB is required for $h = 100$ m. This increases to 40 dB for $h = 170$ m.

Figure 3.8: *Effect of Building Height on the BER.* $d = 24$ *m,* $w = 30$ *mph,* $a = 1$ *cm and* $w_L = 5$ *cm are assumed.*

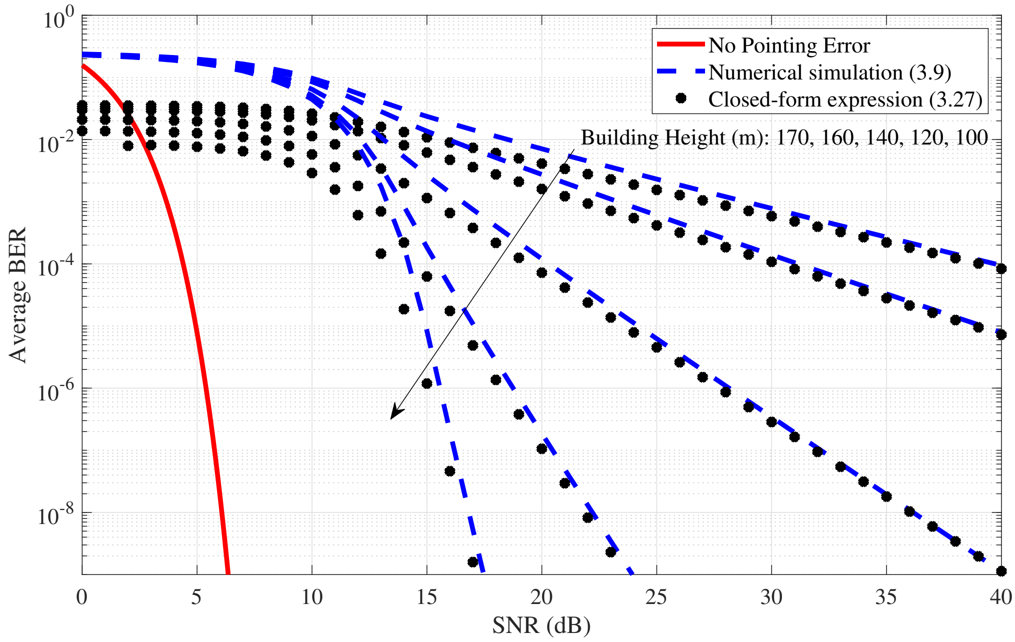

3.4 Conclusion

In the existing literature on FSO systems in the presence of pointing errors, the variance values of jitter are provided without relating them to the underlying physical phenomena. In practice, jitter occurs due to the sway behavior of a building, and the level of misalignment depends on the wind force and static forces on the building coupled with its height and shape. Based on an extensive simulation study using civil engineering software, our study reveals out how the jitter is related to wind loads and building parameters. Through non-linear regression, we propose a closed-form expression for the standard deviation as a function of building height, width and wind speed. Our result demonstrates that the jitter increases as the height of the building or the wind speed increase while all the other parameters are kept constant. Furthermore, it was also seen that the jitter decreases as the building gets wider while all the other parameters are kept constant. Afterwards, we present a closed-form BER expression as a function of these environmental parameters and confirm its accuracy through Monte Carlo simulations. Further studies can commence to model the motion behavior of buildings with non-square forms, and also to analyze the pointing error behavior of terrestrial FSO systems with non-Gaussian beams under wind sway.

4. INFLUENCE OF OCEANIC WAVES AND WIND ON BUOY-BASED UNDERWATER OPTICAL COMMUNICATION SYSTEMS

4.1 Introduction

Underwater Wireless Optical Communication (UWOC) systems have emerged as a promising solution to the growing demand for high-bandwidth data transmission in underwater environments. Unlike traditional Underwater Acoustic Communication (UAC) methods, which suffer from low data rates, significant latency, and vulnerability to multipath effects, UWOC offers gigabit-level data rates with low latency, minimal electromagnetic interference, low mass and power requirements [32, 33]. By using visible or near-infrared light, UWOC systems can support real-time video transmission, sensor data exchange, and autonomous vehicle coordination in applications ranging from environmental monitoring to defense and offshore infrastructure inspection [4]. Performance of UOWC links is greatly degraded by environmental factors such as solar background noise, oceanic turbulence, water absorption and scattering, and pointing error [5].

Pointing error between the receiver and the transmitter is caused by random misalignment known as jitter and boresight. This misalignment causes a considerable loss in the received signal intensity [34]. The degrading effects of pointing error in FSO systems are widely studied in [11]. Numerous statistical models have been proposed to model the statistical distribution of pointing error in FSO systems [34, 35, 36]. In the majority of the FSO works, the Rayleigh distribution for radial displacement, assuming that the displacements in two orthogonal axes causing the misalignment are independent and follow a normal distribution, is adopted [34]. The Rayleigh model is also used in the majority of the UWOC studies as well [37, 38, 39, 40, 41]. In [42], the authors assume a

Beckmann distribution for the radial displacement and derive the PE accordingly. For a vertical UWOC link, the effect of the beam divergence angle on received power is studied in [43]. [44, 45] study the effect of angular misalignment of the transmitted beam, due to the roughness of the sea caused by winds, on channel performance. In this study, the authors also assume a Rayleigh PDF for PE as well. In some works, the authors assume a PDF model for sea surface roughness, assume that the buoy follows the exact shape of the sea surface slope and derive the resultant PE [41, 43, 44, 45, 46].

In none of the UWOC works, neither translational nor rotational motions of the ocean buoy inducing PEs, are ever simulated via an oceanographic simulation tool for varying waves and winds. For the studies that assume a UWOC installed on a buoy, none consider that ocean buoys are connected to the sea surface via moorings, which significantly affect their motion behavior [47]. Additionally, while some studies account for sea surface roughness and assume that the buoy experiences the same angular rotation as the sea surface, none consider the physical properties of the buoy itself. Mass, moment of inertia, center of gravity, stability and natural rolling period are all important factors that determine the buoy's resultant rotational motion [48]. This study aims to fill this gap.

Turbulence-induced fading, caused by fluctuations in water temperature, salt levels (salinity) and density, leads to variations in both the phase and the intensity of the received signal [49]. PDFs of the intensity fluctuations in turbulent atmospheric channels have been studied both theoretically and experimentally. Models, such as log-normal [50, 51, 52, 53], gamma [54], generalized gamma distribution [55], gamma-gamma [55, 56], Weibull [57], Exponential Weibull [55], K [56] have been proposed. A model for underwater turbulence is developed by incorporating turbulent eddies with varying sizes and refractive indices [51]. By combining both pointing error and turbulence-induced fading, BER is derived for a vertical UWOC link under the combined effect of Gamma-Gamma turbulence and Rayleigh distributed PE [58]. Even though most of these studies are entirely theoretical, some present experimental results demonstrating PDFs of turbulence induced fading under various environmental conditions, such as water temperature [52], air bubbles [56] and salinity [59, 60]. Overall, it is stated that single-lobe statistical distributions such as log-normal, Gamma, K, Weibull, exponential Weibull, Gamma-Gamma and generalized Gamma distributions are good matches for the distribution of received signal intensity [54].

In this work, we develop a pointing error model caused solely by buoy tilt, driven by wave and wind loading. We anticipate that the pointing error caused by rotational tilt will have a significantly greater impact than that caused by linear displacements, especially as the link distance, corresponding to the water depth in our case, increases. Moreover, although linear displacements that cause pointing error can be mitigated using multiple moorings, the roll motion of an ocean buoy will persist due to the inherent dynamics of the sea surface. This approach is also adopted in other studies [42]. Towards this end, we use an oceanographic marine simulation software to simulate the rotational and linear motions of a realistic ocean buoy with moorings. We conduct extensive simulations to characterize the roll and pitch behavior of the buoy under different wave heights, wind speeds and wind directions. Statistical analysis of the buoy's roll and pitch angles for varying sea conditions indicate that the motions are not Gaussian, but instead follow a Gaussian Mixture Model (GMM). More so, the rotational motions in two axes are not truly independent due to the effect of the mooring line [61]. To better model the statistical behavior of the rotational motion, tilt angle which is a trigonometric relation between the roll and pitch angles is further studied. It is observed that the tilt angle follows a GMM distribution as well. Through third order polynomial fitting, we present a closed-form expression for the tilt angle distribution as a function of wave height, wind speed and wind direction. We then present the PDF of the pointing error and model the optical channel with this new pointing error and turbulent-induced log-normal fading. Afterwards we derive the closed-form expression for the average BER. Finally, we confirm the accuracy through Monte Carlo simulations for various sea conditions.

The rest of this chapter is organized as follows: In Chapter 4.2, we discuss the simulation model of a realistic ocean buoy and analyze its roll and pitch motions. We then present the statistical distribution of the tilt angle as a function of wave height, wind speed and wind direction based on comprehensive simulation study. In Chapter 4.3, we derive the closed-form expression for the average bit error rate of the UWOC link in the presence of pointing errors and log-normal fading. In Chapter 4.4, we present the numerical results for error probability considering various wave heights and wind speeds. Finally, we conclude in Chapter 4.5.

4.2 Simulating the Motion of an Ocean Buoy Under Various Wave and Wind Condition

To study the motion behavior of an ocean buoy, we use ProteusDS, an oceanographic marine simulation software specialized in dynamic analysis of marine systems. The software uses hydrodynamic and finite-element models and is capable of simulating buoys, moorings and vessels under the effects of wind, current and waves [62]. In this study we simulate a realistic ocean buoy with mooring under various wave and wind conditions and analyze the characteristics of the tilt motion statistically.

Ocean waves are surface oscillations of seawater primarily caused by wind transferring energy to the sea surface. These waves can vary in height, period, and direction. In oceanographic studies, waves are typically characterized using spectral representations, which describe how wave energy is distributed across different frequencies or wavelengths. The Joint North Sea Wave Project (JONSWAP) spectrum is a refined model of the wave energy spectrum developed from measurements in the North Sea and is widely used to model realistic sea states which are commonly irregular and random [63]. The JONSWAP spectrum is widely used in ocean engineering and wave modeling due to its ability to describe wind-generated seas with a pronounced spectral peak. In [64], ocean data from 39 buoys in a coastal area is analyzed and authors indicate that JONSWAP spectrum is accurate in describing the sea states. In our simulations, JONSWAP spectrum is used to generate waves ranging from 1 to 10 meters in height.

Wind is the horizontal movement of air relative to the Earth's surface, driven primarily by pressure gradients caused by uneven solar heating. Wind plays a crucial role in weather patterns and the generation of ocean waves. Wind characteristics such as speed, direction, and turbulence are essential parameters and are often analyzed using statistical and spectral methods. The Norwegian Petroleum Directorate (NPD) spectrum is a standardized model used to describe the power spectral density of wind speed fluctuations, particularly for offshore engineering applications [65]. It captures the turbulent nature of wind by representing how energy is distributed across different frequencies. The NPD spectrum is commonly employed in the design and analysis of offshore structures, providing a realistic representation of wind loading in the seas. In addition, the NPD spectrum has been adopted in the ISO 19901-1 standard, which provides guidelines for the design of offshore structures [66]. In our simulations, NPD spectrum is used to generate winds ranging from 0 to 20 m/s. Furthermore, we used standard wind directions, from 0 degrees to 315 degrees with 45 degrees increments to study the effects of altering wind direction.

In our simulations we consider a commercial ocean buoy, Jet7000 by Mobilis [67]. The physical properties of the buoy [68] are given in Table 4.1 below.

In simulation, the buoy is placed in waters of 50 m depth and is fixed to the sea floor via mooring lines. A finite element model of the buoy is then used in simulations under varying wave height and wind speed conditions. Roll (ϕ), pitch (θ) and tilt (ε) angular motions of the buoy are recorded. Shown in Figure 4.1 below are the axes of

Table 4.1: *Technical Specifications of the Simulated Ocean Buoy Derived from Datasheet.*

Mass (kg)	1747
Surface Visible Area (m^2)	6.7
Net buoyancy (L)	5180
Focal Plane (mm)	5780
Draught (mm)	2830
Total Height (mm)	9510

rotation for these motions.

Figure 4.1: *Rotation and Tilt Axes of the Ocean Buoy.*

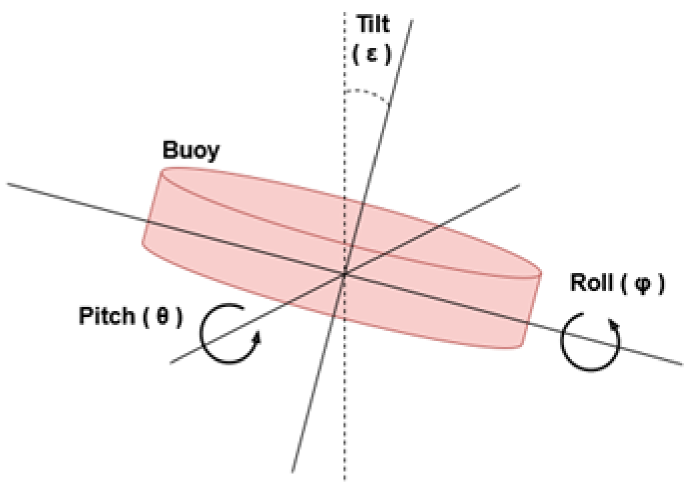

Extensive simulations are carried out for varying wave heights from 1 to 10 meters and wind speeds from 0 to 20 m/s, and wind directions from 0 to 315 degrees. An example simulation output, showing time series of roll, pitch and tilt motion for a buoy experiencing 4 m waves and 0 m/s winds is shown in Figure 4.2 below.

Figure 4.2: *Roll, Pitch, Tilt Angle for the Buoy Experiencing 4 m Waves and 0 m/s Winds ($w = 4$ m, $v = 0$ m/s and $h = 1$).*

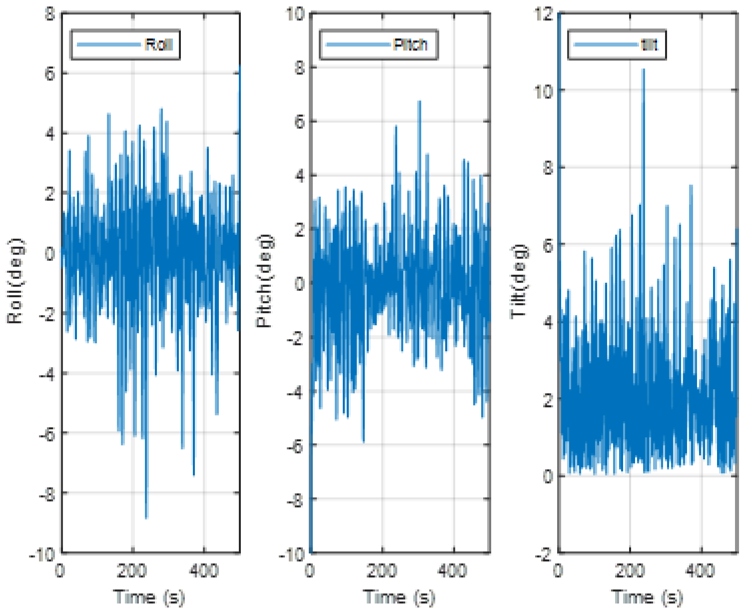

In Figure 4.3 below, histograms for each rotational angle is presented for the case of buoy experiencing 5 m waves, 15 m/s winds with 270 degrees heading. Shape of the distributions clearly indicate the bimodal nature of the simulated buoy motion.

Figure 4.3: *Roll, Pitch and Tilt PDFs of Buoy Experiencing 5 m Waves and 15 m/s Winds with 270 Degrees Heading ($w = 5$ m, $v = 15$ m/s and $h = 7$).*

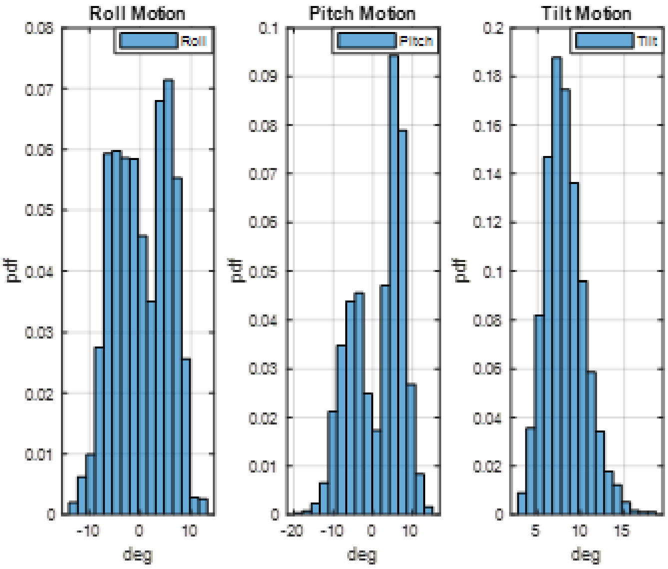

This case is a good example showing how the roll and pitch angles do not follow Gaussian behavior unlike nearly all the works in the literature. Statistical analysis of this data indicates that the roll and pitch behavior of the buoy follow a Gaussian Mixture Model (GMM). This behavior can be clearly seen in the shape of the roll and pitch PDFs as they have separate peaks due to bimodality.

GMM is a probabilistic model, useful for representing the data as a mixture of several Gaussian distributions with independent parameters. PDF of the data is represented as a weighted sum of K normally distributed components [69] as shown in Equation (4.1).

$$p(x) = \sum_{k=1}^{K} A_k N(x \mid \mu_k, \sigma_k) \tag{4.1}$$

where, A_k is the mixture weight and it follows $\sum A_k = 1$ and $A_k \geq 0$, $N(x \mid \mu_k, \sigma_k)$ is the multivariate normal distribution with mean μ_k and standard deviation σ_k.

In our simulations, it is observed that the bimodality trend becomes more obvious as the wave heights and wind speeds increase. For our work, we adopt $K = 2$ as it gives good results and is computationally less complex compared to higher values K.

To reliably model the motion behavior, tilt angle is studied as it already incorporates both the roll and the pitch motion of the buoy. The tilt angle can be represented as [[70], Eq. (A2)]

$$\varepsilon = arccos\left(cos\left(\phi\right) \cdot cos\left(\theta\right)\right) \tag{4.2}$$

The buoy rotational motion is simulated extensively for wave heights (w) ranging from 1 to 10 m, wind speeds (v) from 0 to 20 m/s and wind direction (h) representing directions of 0 to 315 degrees as shown in Table 4.2 below.

Table 4.2: *Correspondence Between Wind Directions and Variable h.*

Wind Direction (deg)	**Compass Point**	h
0	North	1
45	Northeast	2
90	East	3
135	Southeast	4
180	South	5
225	Southwest	6
270	West	7
315	Northwest	8

Afterwards, a GMM curve is fit to the tilt data and its coefficients for two Gaussian components are computed with Matlab's fitgmdist function. Shown in Table 4.3 below are the computed GMM coefficients from the simulated test cases for $h = 1$.

Table 4.3: *Displacement Statistics Under Varying Winds and Building Heights.*

w (m)	v (m/s)	A	μ_1 (rad)	σ_1 (rad)	μ_2 (rad)	σ_2 (rad)
1	0	0.9829	0.0133	0.0027	0.0704	0.1423

Continued from previous page

1	5	0.9794	0.0207	0.0064	0.0781	0.1268
1	10	0.9702	0.0698	0.0175	0.1137	0.0786
1	15	0.6570	0.1292	0.0403	0.1694	0.0381
1	20	0.3902	0.1949	0.0851	0.2464	0.1044
2	0	0.9846	0.0223	0.0084	0.0772	0.1313
2	5	0.6219	0.0186	0.0056	0.0416	0.0274
2	10	0.4127	0.0620	0.0197	0.0801	0.0443
2	15	0.5289	0.1285	0.0587	0.1619	0.0630
2	20	0.3708	0.2064	0.1305	0.2404	0.1367
3	0	0.6509	0.0229	0.0065	0.0466	0.0285
3	5	0.5847	0.0208	0.0058	0.0533	0.0362
3	10	0.5078	0.0579	0.0258	0.0941	0.0562
3	15	0.2830	0.1341	0.0703	0.1518	0.1056
3	20	0.4887	0.2125	0.1569	0.2468	0.1610
4	0	0.6089	0.0274	0.0090	0.0592	0.0426
4	5	0.6070	0.0260	0.0086	0.0682	0.0558
4	10	0.4648	0.0556	0.0282	0.1027	0.0801
4	15	0.2196	0.1297	0.0699	0.1573	0.1398
4	20	0.5400	0.2211	0.1788	0.2500	0.2330
5	0	0.6372	0.0334	0.0144	0.0762	0.0745
5	5	0.5954	0.0307	0.0130	0.0837	0.0876
5	10	0.4869	0.0582	0.0347	0.1174	0.1180
5	15	0.4486	0.1417	0.0822	0.1682	0.1677
5	20	0.5854	0.2214	0.1959	0.2703	0.2875

Continued from previous page						
6	0	0.6256	0.0377	0.0184	0.0935	0.1172
6	5	0.5926	0.0362	0.0189	0.1018	0.1361
6	10	0.4960	0.0625	0.0427	0.1346	0.1715
6	15	0.7429	0.1494	0.1569	0.2212	0.3129
6	20	0.8043	0.2394	0.2742	0.3021	0.6306
7	0	0.6345	0.0428	0.0233	0.1132	0.1726
7	5	0.6012	0.0424	0.0258	0.1220	0.1960
7	10	0.5306	0.0692	0.0565	0.1554	0.2487
7	15	0.7899	0.1581	0.2017	0.2542	0.5039
7	20	0.9281	0.2526	0.3789	0.3845	0.6256
8	5	0.5927	0.0488	0.0334	0.1438	0.3060
8	10	0.5665	0.0787	0.0781	0.1810	0.4109
8	15	0.8200	0.1689	0.2604	0.2951	0.8871
8	20	0.9117	0.2598	0.4447	0.4298	1.5976
9	0	0.6454	0.0564	0.0451	0.1648	0.4730
9	5	0.6193	0.0587	0.0515	0.1753	0.5373
9	10	0.6136	0.0915	0.1154	0.2144	0.6869
9	15	0.8226	0.1784	0.3175	0.3433	1.2847
9	20	0.8791	0.2657	0.4880	0.4714	1.9367
10	0	0.7319	0.1119	0.2075	0.3364	1.8992
10	5	0.6182	0.0679	0.0719	0.2063	0.7792
10	10	0.6443	0.1048	0.1547	0.2574	1.0337
10	15	0.8227	0.1899	0.3812	0.3983	1.8318
10	20	0.8569	0.2734	0.5424	0.5093	2.2016

Afterwards, a 3rd order polynomial fit is used to fit the data, and the closed-form expression for each GMM coefficient is computed for a given wave height w and wind speed v and wind direction h. Equations (4.3)- (4.7) below show the relationship for each coefficient.

$$\begin{aligned} A = c_{A_1}w^3 + c_{A_2}w^2v + c_{A_3}w^2\theta + c_{A_4}w^2 + c_{A_5}wv^2 + c_{A_6}wv\theta + c_{A_7}wv \\ +c_{A_8}w\theta^2 + c_{A_9}w\theta + c_{A_{10}}w + c_{A_{11}}v^3 + c_{A_{12}}v^2\theta + c_{A_{13}}v^2 + c_{A_{14}}v\theta^2 \\ +c_{A_{15}}v\theta + c_{A_{16}}v + c_{A_{17}}\theta^3 + c_{A_{18}}\theta^2 + c_{A_{19}}\theta + c_{A_{20}} \end{aligned} \tag{4.3}$$

$$\begin{aligned} \mu_1 = c_{\mu_{1.1}}w^3 + c_{\mu_{1.2}}w^2v + c_{\mu_{1.3}}w^2\theta + c_{\mu_{1.4}}w^2 + c_{\mu_{1.5}}wv^2 + c_{\mu_{1.6}}wv\theta + c_{\mu_{1.7}}wv \\ +c_{\mu_{1.8}}w\theta^2 + c_{\mu_{1.9}}w\theta + c_{\mu_{1.10}}w + c_{\mu_{1.11}}v^3 + c_{\mu_{1.12}}v^2\theta + c_{\mu_{1.13}}v^2 + c_{\mu_{1.14}}v\theta^2 \\ +c_{\mu_{1.15}}v\theta + c_{\mu_{1.16}}v + c_{\mu_{1.17}}\theta^3 + c_{\mu_{1.18}}\theta^2 + c_{\mu_{1.19}}\theta + c_{\mu_{1.20}} \end{aligned} \tag{4.4}$$

$$\begin{aligned} \sigma_1 = c_{\sigma_{1.1}}w^3 + c_{\sigma_{1.2}}w^2v + c_{\sigma_{1.3}}w^2\theta + c_{\sigma_{1.4}}w^2 + c_{\sigma_{1.5}}wv^2 + c_{\sigma_{1.6}}wv\theta + c_{\sigma_{1.7}}wv \\ +c_{\sigma_{1.8}}w\theta^2 + c_{\sigma_{1.9}}w\theta + c_{\sigma_{1.10}}w + c_{\sigma_{1.11}}v^3 + c_{\sigma_{1.12}}v^2\theta + c_{\sigma_{1.13}}v^2 + c_{\sigma_{1.14}}v\theta^2 \\ +c_{\sigma_{1.15}}v\theta + c_{\sigma_{1.16}}v + c_{\sigma_{1.17}}\theta^3 + c_{\sigma_{1.18}}\theta^2 + c_{\sigma_{1.19}}\theta + c_{\sigma_{1.20}} \end{aligned} \tag{4.5}$$

$$\begin{aligned} \mu_2 = c_{\mu_{2.1}}w^3 + c_{\mu_{2.2}}w^2v + c_{\mu_{2.3}}w^2\theta + c_{\mu_{2.4}}w^2 + c_{\mu_{2.5}}wv^2 + c_{\mu_{2.6}}wv\theta + c_{\mu_{2.7}}wv \\ +c_{\mu_{2.8}}w\theta^2 + c_{\mu_{2.9}}w\theta + c_{\mu_{2.10}}w + c_{\mu_{2.11}}v^3 + c_{\mu_{2.12}}v^2\theta + c_{\mu_{2.13}}v^2 + c_{\mu_{2.14}}v\theta^2 \\ +c_{\mu_{2.15}}v\theta + c_{\mu_{2.16}}v + c_{\mu_{2.17}}\theta^3 + c_{\mu_{2.18}}\theta^2 + c_{\mu_{2.19}}\theta + c_{\mu_{2.20}} \end{aligned} \tag{4.6}$$

$$\sigma_2 = c_{\sigma_{2.1}} w^3 + c_{\sigma_{2.2}} w^2 v + c_{\sigma_{2.3}} w^2 \theta + c_{\sigma_{2.4}} w^2 + c_{\sigma_{2.5}} w v^2 + c_{\sigma_{2.6}} w v \theta + c_{\sigma_{2.7}} w v$$
$$+ c_{\sigma_{2.8}} w \theta^2 + c_{\sigma_{2.9}} w \theta + c_{\sigma_{2.10}} w + c_{\sigma_{2.11}} v^3 + c_{\sigma_{2.12}} v^2 \theta + c_{\sigma_{2.13}} v^2 + c_{\sigma_{2.14}} v \theta^2 \quad (4.7)$$
$$+ c_{\sigma_{2.15}} v \theta + c_{\sigma_{2.16}} v + c_{\sigma_{2.17}} \theta^3 + c_{\sigma_{2.18}} \theta^2 + c_{\sigma_{2.19}} \theta + c_{\sigma_{2.20}}$$

The corresponding coefficient values are given in Table 4.4 below.

Table 4.4: *3^{rd} Order Polyfit Coefficients for the Closed-form Relationship Between the Wave Height, Wind Speed and Wind Direction to GMM Parameters Used in Equation* (4.1) *and Equations* (4.3)- (4.7).

Curve Ratio (A)		Curve 1 Mean (μ_1)		Curve 1 Std. (σ_1)		Curve 2 Mean (μ_2)		Curve 2 Std. (σ_2)	
Coeff.	**Value**	**Coeff.**	**Value**	**Coeff.**	**Value**	**Coeff.**	**Value**	**Coeff.**	**Value**
c_{A_1}	-0.00282	$c_{\mu_{1_1}}$	2.821e-05	$c_{\sigma_{1_1}}$	0.000164	$c_{\mu_{2_1}}$	-5.045e-06	$c_{\sigma_{2_1}}$	0.00298
c_{A_2}	0.00444	$c_{\mu_{1_2}}$	-3.148e-05	$c_{\sigma_{1_2}}$	-1.307e-05	$c_{\mu_{2_2}}$	-6.990e-05	$c_{\sigma_{2_2}}$	-0.000204
c_{A_3}	-0.01711	$c_{\mu_{1_3}}$	-0.00199	$c_{\sigma_{1_3}}$	-0.00592	$c_{\mu_{2_3}}$	-0.00755	$c_{\sigma_{2_3}}$	-0.0754
c_{A_4}	0.05905	$c_{\mu_{1_4}}$	-0.000554	$c_{\sigma_{1_4}}$	6.132e-05	$c_{\mu_{2_4}}$	0.00477	$c_{\sigma_{2_4}}$	-0.0159
c_{A_5}	9.906e-05	$c_{\mu_{1_5}}$	2.953e-05	$c_{\sigma_{1_5}}$	0.000130	$c_{\mu_{2_5}}$	9.045e-05	$c_{\sigma_{2_5}}$	0.00100
c_{A_6}	-0.00716	$c_{\mu_{1_6}}$	-0.00161	$c_{\sigma_{1_6}}$	-0.00682	$c_{\mu_{2_6}}$	-0.00721	$c_{\sigma_{2_6}}$	-0.0500
c_{A_7}	0.00900	$c_{\mu_{1_7}}$	-0.000292	$c_{\sigma_{1_7}}$	-0.00109	$c_{\mu_{2_7}}$	-0.000348	$c_{\sigma_{2_7}}$	- 0.00947
c_{A_8}	-2.839	$c_{\mu_{1_8}}$	0.926	$c_{\sigma_{1_8}}$	3.514	$c_{\mu_{2_8}}$	1.876	$c_{\sigma_{2_8}}$	10.913
c_{A_9}	0.537	$c_{\mu_{1_9}}$	-0.0933	$c_{\sigma_{1_9}}$	-0.359	$c_{\mu_{2_9}}$	-0.137	$c_{\sigma_{2_9}}$	-0.4529
$c_{A_{10}}$	-0.396	$c_{\mu_{1_{10}}}$	0.000706	$c_{\sigma_{1_{10}}}$	0.00165	$c_{\mu_{2_{10}}}$	-0.0276	$c_{\sigma_{2_{10}}}$	-0.00622
$c_{A_{11}}$	6.905e-05	$c_{\mu_{1_{11}}}$	-1.292e-05	$c_{\sigma_{1_{11}}}$	-7.291e-06	$c_{\mu_{2_{11}}}$	-1.170e-05	$c_{\sigma_{2_{11}}}$	-4.439e-05
$c_{A_{12}}$	-6.613e-05	$c_{\mu_{1_{12}}}$	-1.702e-05	$c_{\sigma_{1_{12}}}$	-0.00115	$c_{\mu_{2_{12}}}$	0.000827	$c_{\sigma_{2_{12}}}$	0.000105
$c_{A_{13}}$	-0.00260	$c_{\mu_{1_{13}}}$	0.000784	$c_{\sigma_{1_{13}}}$	0.000163	$c_{\mu_{2_{13}}}$	0.000561	$c_{\sigma_{2_{13}}}$	-0.00143
$c_{A_{14}}$	2.0114	$c_{\mu_{1_{14}}}$	0.598	$c_{\sigma_{1_{14}}}$	2.0508	$c_{\mu_{2_{14}}}$	1.191	$c_{\sigma_{2_{14}}}$	4.934
$c_{A_{15}}$	-0.1794	$c_{\mu_{1_{15}}}$	-0.0719	$c_{\sigma_{1_{15}}}$	-0.225	$c_{\mu_{2_{15}}}$	-0.139	$c_{\sigma_{2_{15}}}$	-0.477
$c_{A_{16}}$	-0.0192	$c_{\mu_{1_{16}}}$	-0.000778	$c_{\sigma_{1_{16}}}$	0.00506	$c_{\mu_{2_{16}}}$	0.00102	$c_{\sigma_{2_{16}}}$	0.0321
$c_{A_{17}}$	65.993	$c_{\mu_{1_{17}}}$	38.641	$c_{\sigma_{1_{17}}}$	28.973	$c_{\mu_{2_{17}}}$	162.896	$c_{\sigma_{2_{17}}}$	747.0381
$c_{A_{18}}$	-22.303	$c_{\mu_{1_{18}}}$	-14.290	$c_{\sigma_{1_{18}}}$	-32.319	$c_{\mu_{2_{18}}}$	-42.986	$c_{\sigma_{2_{18}}}$	-209.806

Continued from previous page									
Coeff.	**Value**	**Coeff.**	**Value**	**Coeff.**	**Value**	**Coeff.**	**Value**	**Coeff.**	**Value**
$c_{A_{19}}$	1.381	$c_{\mu_{1_{19}}}$	1.176	$c_{\sigma_{1_{19}}}$	3.405	$c_{\mu_{2_{19}}}$	2.790	$c_{\sigma_{2_{19}}}$	13.428
$c_{A_{20}}$	1.411	$c_{\mu_{1_{20}}}$	0.00105	$c_{\sigma_{1_{20}}}$	-0.0441	$c_{\mu_{2_{20}}}$	0.0701	$c_{\sigma_{2_{20}}}$	-0.000406

Overall, a good fit for each coefficient was achieved, with RMSE values ranging from 0.0097 to 0.2418 were obtained.

Validity of the derived formulation is tested against simulated data. For each case the corresponding GMM coefficients are obtained based on Equation (4.1) and Equations (4.3)- (4.7). Figure 4.4 below presents the tilt angle PDF of the ocean buoy experiencing $w = 3$ m, $v = 15$ m/s and $h = 1$. In the plot the GMM curve obtained by Matlab and the GMM curve obtained by Equation (4.1) and Equations (4.3)- (4.7) are shown for comparison.

Figure 4.4: *GMM Fit for the Case $w = 3$ m, $v = 15$ m/s and $h = 1$, Low Bimodality is Observed.*

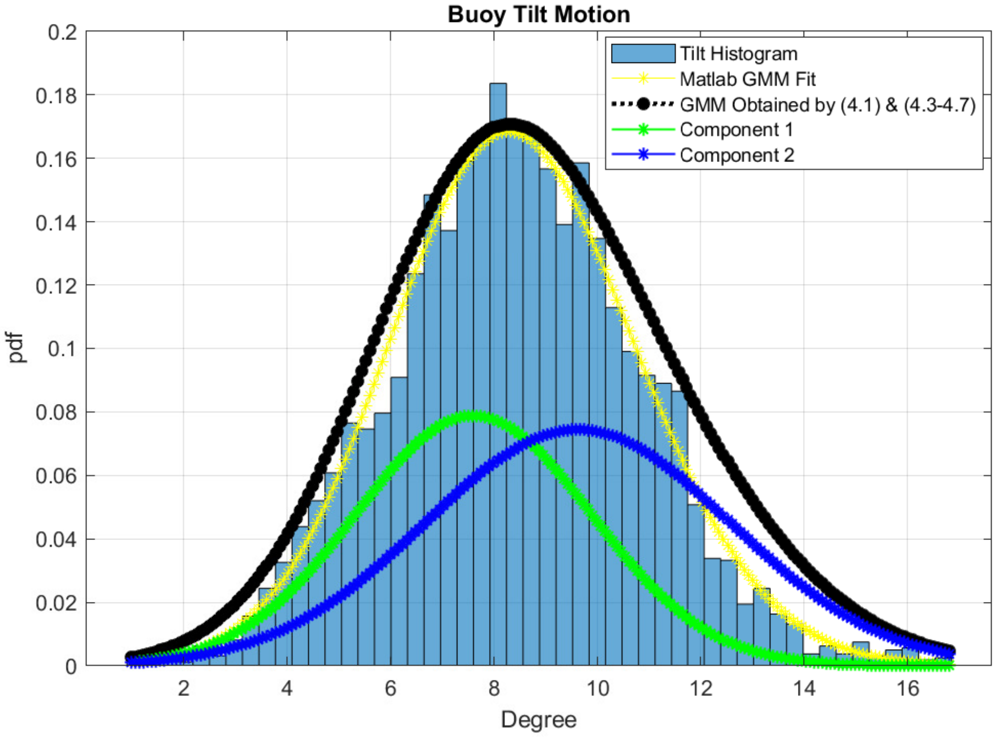

Overall, a good match is observed. Furthermore, the two components of the obtained GMM curve are also shown. This case is a good example of the overall tilt PDF being weakly bimodal. Figure 4.5 below represents the GMM fitting for the case where $w = 6$ m, $v = 15$ m/s and $h = 4$.

Figure 4.5: *GMM Fit for the Case $w = 6$ m, $v = 15$ m/s and $h = 4$, Medium Bimodality is Observed.*

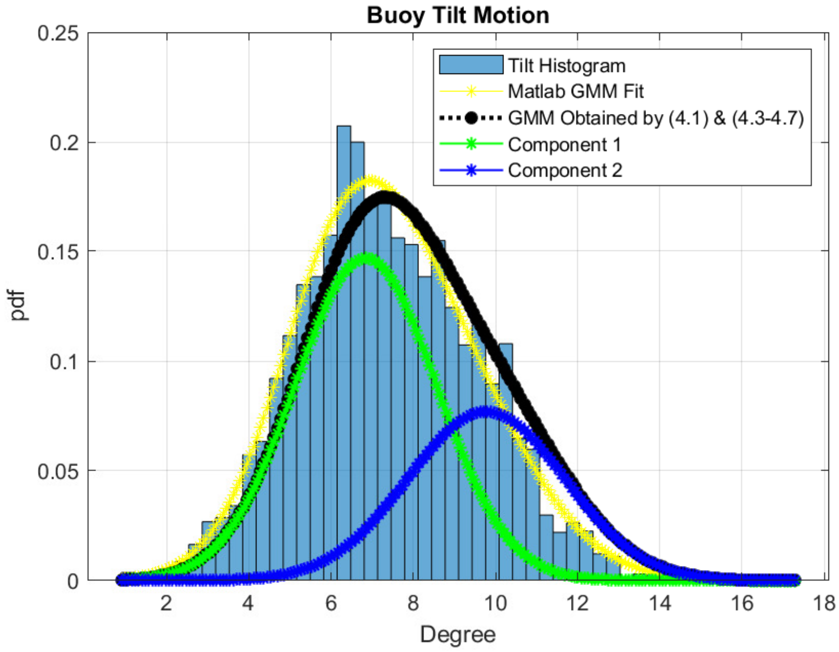

This case is a good example where the resultant curve bimodality is moderate. Figure 4.6 below represents the GMM fitting for the case where $w = 10$ m, $v = 20$ m/s and $h = 7$.

Figure 4.6: *GMM Fit for the Case $w = 10$ m, $v = 20$ m/s and $h = 7$, High Bimodality is Observed.*

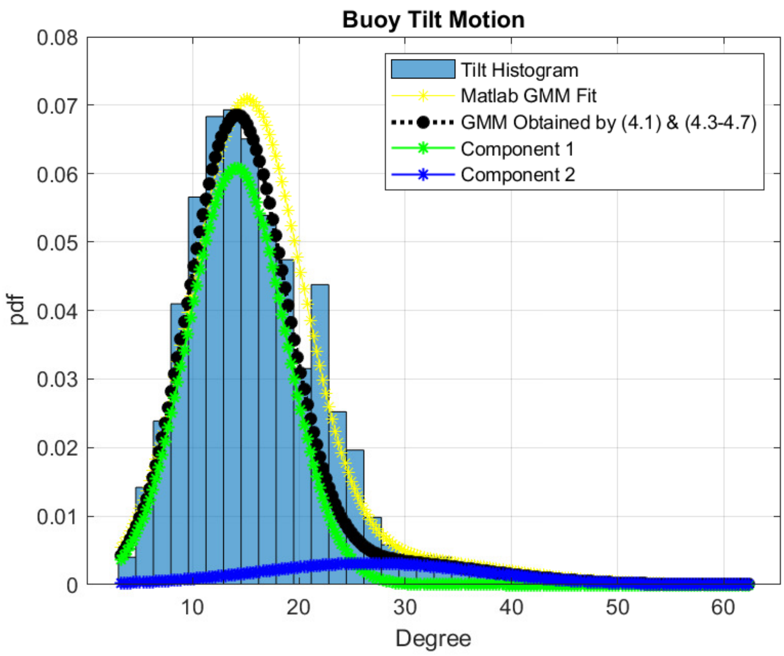

This case is a good example where the resultant curve bimodality is high. In all cases, the GMM approach and the closed-form expressions Equation (4.1) and Equations (4.3)- (4.7) seem to provide a reasonable approximation of the buoy tilt angle PDF.

4.3 Error Performance in the Presence of Pointing Error and Turbulence Induced Fading

4.3.1 Pointing Error

We consider a UOWC link with a transmission distance of water depth d and a circular receive aperture with radius a. The fraction of the power collected by the receiver is given by

$$h_p(\mathbf{r};d) = \int\limits_A I_{beam}(\rho - \mathbf{r};d)d\rho \tag{4.8}$$

where $r = \|\mathrm{r}\| = \sqrt{r_x^2 + r_y^2}$ is the radial vector from the detector to beam center, ρ is the radial vector from beam center, and $A = \pi a^2$ is the circular detection area. Here $I_{beam}\left(.\right)$ represents the normalized spatial distribution of transmitted intensity. For a Gaussian beam, it is given by [11]

$$I_{beam}(\rho;d) = A_0 \exp\left(-\frac{2\|\rho\|^2}{w_L^2}\right) \tag{4.9}$$

where w_L is the beam waist and A_0 is the fraction of the collected power at $r = 0$. It can be calculated as $A_0 = \left[\mathrm{erf}\left(v\right)\right]^2$ where $v = \left(\sqrt{\pi}a\right)/\left(\sqrt{2}w_L\right)$ is the ratio between circular aperture radius and beam waist. Assuming that the radial distance is located along the primary axis, the pointing error is approximated as [11]

$$h_p(r;d) \approx A_0 \mathrm{exp}\left(-\frac{2r^2}{w_{L_{eq}}^2}\right) \tag{4.10}$$

where $w_{L_{eq}}$ is the equivalent beam width and defined as [11]

$$w_{L_{eq}}^2 = w_L^2 \frac{\sqrt{\pi}\mathrm{erf}\left(v\right)}{2v\mathrm{exp}\left(-v^2\right)} \tag{4.11}$$

Radial distance r is a trigonometric function of water depth d as depicted in Figure 4.7 below.

Figure 4.7: *Transmitted Beam Radial Distance.*

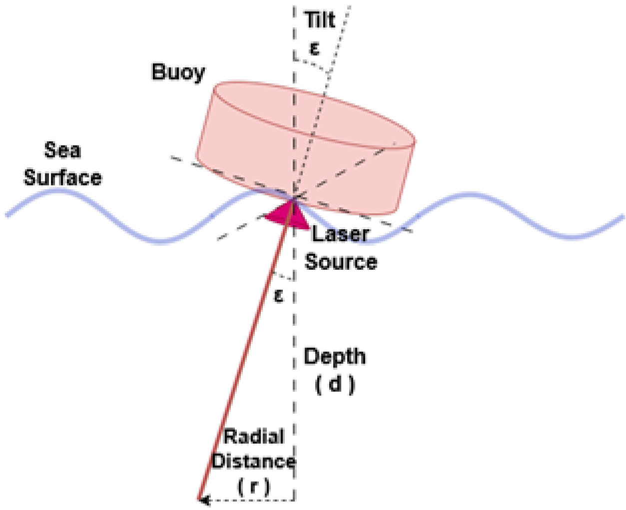

Based on the tilt angle ε can be represented as

$$\varepsilon = \arctan\left(\frac{r}{d}\right) \tag{4.12}$$

Realizing that the tilt angle follows a GMM distribution, its PDF can be represented as

$$f_{\varepsilon}\left(\varepsilon\right) = A\mathrm{N}\left(\varepsilon;\mu_1,\sigma_1^2\right) + (1-A)\mathrm{N}\left(\varepsilon;\mu_2,\sigma_2^2\right) \tag{4.13}$$

where

$$N(\varepsilon;\mu,\sigma^2) = \frac{1}{\sqrt{2\pi}\sigma}exp\left(-\frac{(\varepsilon-\mu)^2}{2\sigma^2}\right) \tag{4.14}$$

By combining Equations (4.13)- (4.14) and applying density transformation according to Equation (4.12), the PDF of radial distance r can be obtained as

$$f_r(r) = \begin{bmatrix} A\frac{1}{\sqrt{2\pi}\sigma_1}exp\left(-\frac{\left(\tan^{-1}\left(\frac{r}{d}\right)-\mu_1\right)^2}{2\sigma_1^2}\right)+ \\ (1-A)\frac{1}{\sqrt{2\pi}\sigma_2}exp\left(-\frac{\left(\tan^{-1}\left(\frac{r}{d}\right)-\mu_2\right)^2}{2\sigma_2^2}\right) \end{bmatrix} \frac{d}{d^2+r^2}\frac{180}{\pi} \tag{4.15}$$

where $d/(d^2+r^2)$ is the Jacobian and $180/\pi$ term is added for converting between radians to degrees.

Performing density transformation of r to h_p on the combination of Equation (4.10) and Equation (4.15) and some further simplifications, the PDF of pointing error $f_{h_p}(h_p)$ for GMM radial displacement with two components is obtained as

$$f_{h_p}(h_p) = \begin{bmatrix} A\frac{1}{\sqrt{2\pi}\sigma_1}exp\left(-\frac{\left(\tan^{-1}\left(\frac{\sqrt{-0.5w_{zeq}^2\ln\left(\frac{h_p}{A_0}\right)}}{d}\right)-\mu_1\right)^2}{2\sigma_1^2}\right)+ \\ (1-A)\frac{1}{\sqrt{2\pi}\sigma_2}exp\left(-\frac{\left(\tan^{-1}\left(\frac{\sqrt{-0.5w_{zeq}^2\ln\left(\frac{h_p}{A_0}\right)}}{d}\right)-\mu_2\right)^2}{2\sigma_2^2}\right) \end{bmatrix} \times\frac{45w_{zeq}^2h_p^{-1}d\pi^{-1}}{\left[d^2-0.5w_{zeq}^2\ln\left(\frac{h_p}{A_0}\right)\right]\left[\sqrt{-0.5w_{zeq}^2\ln\left(\frac{h_p}{A_0}\right)}\right]} \tag{4.16}$$

4.3.2 Turbulence Induced Fading

Turbulence induced log-normal fading h_t is deterministic and can represented as [71]

$$f_{h_t}(h_t) = \frac{1}{h_t\sigma_t\sqrt{2\pi}}\exp\left(-\frac{(\ln h_t-\mu_t)^2}{2\sigma_t^2}\right),\ h_t>0 \tag{4.17}$$

where $\sigma_t = \sqrt{\ln\left(1+\sigma_I^2\right)}$, σ_I^2 is the scintillation index, μ_t and σ_I^2 are the mean and variance of logarithmic fading. Assuming turbulent waters, good mixing will be achieved between water layers, and hence a moderate turbulence value σ_t^2 is adopted [72].

4.3.3 *Error Performance*

We assume IM/DD system with OOK modulation. The signal received is given by

$$y = hRx + z \tag{4.18}$$

where R is the detector responsivity, x is the transmitted OOK signal, z is AWGN and h is the channel fading coefficient described as

$$h = h_p h_t \tag{4.19}$$

where h_p is the pointing error and h_t is the turbulent-induced channel fading.

The transmitted signal symbols are drawn from OOK constellation equiprobably such that $x \in \{0, 2P_t\}$, where P_t is the average transmitted optical power. The conditional BER for an IM/DD system with OOK is given by [17]

$$P_b(e|h) = \frac{1}{2}\text{erfc}\left(\frac{P_t h}{\sigma_N}\right) \tag{4.20}$$

The average BER can be obtained by averaging Equation (4.20) over PDF of h.

$$\overline{BER} = P_b\left(e\right) = \int\limits_0^\infty \int\limits_0^{A_0} BER\left(h_p, h_t\right) f_{h_p}\left(h_p\right) f_{h_t}\left(h_t\right) dh_p dh_t \tag{4.21}$$

In order to ease the derivation process, the inner argument which is a function of h_p and $BER\left(h_p\right)$ is studied first. Assuming Unipolar Pulse Amplitude Modulation

(PAM), the average BER resulting from h_p can be written as

$$U = \overline{BER}\left(h_t\right) = \int_0^{A_0} BER\left(h_p\right) f_{h_p}\left(h_p\right) dh_p = \int_0^{A_0} F\,\mathrm{erfc}\left(\sqrt{C\gamma} h_p\right)\; f_{h_p}\left(h_p\right) dh_p \tag{4.22}$$

where F is the power efficiency of PAM and is described as

$$F = \frac{M-1}{M\log_2\left(M\right)} \tag{4.23}$$

as M is number of distinct amplitude levels used in modulation, for k bits per symbol, $M = 2^k$. C is the normalized average power of the unipolar PAM constellation and is described as

$$C = \frac{3}{2\left(M-1\right)\left(2M-1\right)} \tag{4.24}$$

Now combining Equation (4.22) with Equation (4.16), and some re-arrangements, U is re-written as

$$U = \frac{FA}{\sqrt{2\pi}\sigma_1}\int\limits_0^{A_0} \mathrm{erfc}\left(\sqrt{C\gamma}h_p\right)\ exp\left(-\frac{\left(\tan^{-1}\left(\frac{\sqrt{-0.5w_{z_{eq}}^2\ln\left(\frac{h_p}{A_0}\right)}}{d}\right)-\mu_1\right)^2}{2\sigma_1^2}\right) \times \frac{45w_{z_{eq}}^2 h_p^{-1} d\pi^{-1}}{\left[d^2-0.5w_{z_{eq}}^2\ln\left(\frac{h_p}{A_0}\right)\right]\left[\sqrt{-0.5w_{z_{eq}}^2\ln\left(\frac{h_p}{A_0}\right)}\right]}dh_p + \frac{F(1-A)}{\sqrt{2\pi}\sigma_2}\int\limits_0^{A_0} \mathrm{erfc}\left(\sqrt{C\gamma}h_p\right)\ exp\left(-\frac{\left(\tan^{-1}\left(\frac{\sqrt{-0.5w_{z_{eq}}^2\ln\left(\frac{h_p}{A_0}\right)}}{d}\right)-\mu_2\right)^2}{2\sigma_2^2}\right) \times \frac{45w_{z_{eq}}^2 h_p^{-1} d\pi^{-1}}{\left[d^2-0.5w_{z_{eq}}^2\ln\left(\frac{h_p}{A_0}\right)\right]\left[\sqrt{-0.5w_{z_{eq}}^2\ln\left(\frac{h_p}{A_0}\right)}\right]}dh_p \tag{4.25}$$

Realizing the values of interest, the following approximation is considered.

$$d^2 - 0.5w_{z_{eq}}^2 \ln\left(\frac{h_p}{A_0}\right) \approx d^2 \tag{4.26}$$

Substituting Equation (4.26) into Equation (4.25) and further rearrangement of the constants to outside of the integration, following expression is obtained.

$$U = \frac{45FAw_{z_{eq}}^2}{\pi^{3/2}d\sqrt{2}\sigma_1}\int_0^{A_0}\left[\begin{array}{c}\operatorname{erfc}\left(\sqrt{C\gamma}h_p\right)\ exp\left(-\frac{\left(\tan^{-1}\left(\frac{\sqrt{-0.5w_{z_{eq}}^2\ln\left(\frac{h_p}{A_0}\right)}}{d}\right)-\mu_1\right)^2}{2\sigma_1^2}\right)\\ \times\frac{h_p^{-1}}{\left[\sqrt{-0.5w_{z_{eq}}^2\ln\left(\frac{h_p}{A_0}\right)}\right]}dh_p\end{array}\right] + \frac{45F(1-A)w_{z_{eq}}^2}{\pi^{3/2}d\sqrt{2}\sigma_2}\int_0^{A_0}\left[\begin{array}{c}\operatorname{erfc}\left(\sqrt{C\gamma}h_p\right)\ exp\left(-\frac{\left(\tan^{-1}\left(\frac{\sqrt{-0.5w_{z_{eq}}^2\ln\left(\frac{h_p}{A_0}\right)}}{d}\right)-\mu_2\right)^2}{2\sigma_2^2}\right)\\ \times\frac{h_p^{-1}}{\left[\sqrt{-0.5w_{z_{eq}}^2\ln\left(\frac{h_p}{A_0}\right)}\right]}dh_p\end{array}\right] \tag{4.27}$$

To facilitate the derivation, the following is defined

$$x = \sqrt{-0.5w_{z_{eq}}^2\ln\left(\frac{h_p}{A_0}\right)} \tag{4.28}$$

In order to perform variable substitution is obtained as

$$dh_p = 2A_0\exp\left(-\frac{2x^2}{w_{z_{eq}}^2}\right)\left(-\frac{2}{w_{z_{eq}}^2}\right)xdx \tag{4.29}$$

Using Equations (4.28)- (4.29) and utilizing variable substitution between x and h_p, Equation (4.27) can be written as

$$U = \frac{180FA}{\pi^{3/2}d\sqrt{2}\sigma_1}\int_0^{\infty}\left[\begin{array}{c}\operatorname{erfc}\left(\sqrt{C\gamma}A_0\exp\left(-\frac{2x^2}{w_{z_{eq}}^2}\right)\right)\\ \times\ exp\left(-\frac{\left(\tan^{-1}\left(\frac{x}{d}\right)-\mu_1\right)^2}{2\sigma_1^2}\right)dx\end{array}\right] + \frac{180F(1-A)}{\pi^{3/2}d\sqrt{2}\sigma_2}\int_0^{\infty}\left[\begin{array}{c}\operatorname{erfc}\left(\sqrt{C\gamma}A_0\exp\left(-\frac{2x^2}{w_{z_{eq}}^2}\right)\right)\\ \times\ exp\left(-\frac{\left(\tan^{-1}\left(\frac{x}{d}\right)-\mu_2\right)^2}{2\sigma_2^2}\right)dx\end{array}\right] \tag{4.30}$$

Realizing the form inside the integration, the Gaussian-Hermite quadrature formula [73] is considered. To do so, first the following variable is introduced.

$$z^2 = \frac{\left(\tan^{-1}\left(\frac{x}{d}\right) - \mu_2\right)^2}{2\sigma_2^2} \tag{4.31}$$

Therefore x can be written as

$$x = d \ \tan\left(\mu_2 + \sqrt{2\sigma_2^2} \ z\right) \tag{4.32}$$

To continue the variable transformation, the derivative is also obtained as, the following re-arrangement is made

$$\tan^{-1}\left(\frac{x}{d}\right) = \mu_2 + \sqrt{2\sigma_2^2} \ z \tag{4.33}$$

Derivative is then written

$$2\sigma_2^2 \left(\frac{d^2 + x^2}{d}\right) dz = dx \tag{4.34}$$

Performing variable transformation between x and z, realizing conversion from radians to degrees by multiplying the expression with $\pi/180$, and substituting Equation (4.31) and Equation (4.34) into Equation (4.30), following relationship is achieved

$$U = \frac{FA}{\sqrt{\pi}} \int_{-\infty}^{\infty} \left(\begin{array}{l} \left(1 + \ \mathrm{tand}^2 \left(\mu_1 + \sqrt{2\sigma_1^2} \ \ z\right)\right) \\ \quad \times \, \mathrm{erfc}\left(\sqrt{C\gamma}\, A_0 \exp\left(-2\frac{d^2 \ \ \mathrm{tand}^2\left(\mu_1 + \sqrt{2\sigma_1^2} \ \ z\right)}{w_{z_{eq}}^2}\right)\right) \\ \quad \times \, exp\left(-z^2\right) dz \end{array} \right) + \frac{F(1-A)}{\sqrt{\pi}} \int_{-\infty}^{\infty} \left(\begin{array}{l} \left(1 + \ \mathrm{tand}^2 \left(\mu_2 + \sqrt{2\sigma_2^2} \ \ z\right)\right) \\ \quad \times \, \mathrm{erfc}\left(\sqrt{C\gamma}\, A_0 \exp\left(-2\frac{d^2 \ \ \mathrm{tand}^2\left(\mu_2 + \sqrt{2\sigma_2^2} \ \ z\right)}{w_{z_{eq}}^2}\right)\right) \\ \quad \times \, exp\left(-z^2\right) dz \end{array} \right) \tag{4.35}$$

The integration in Equation (4.35) is in the form of $\int_{-\infty}^{\infty} g\left(y_i\right) f\left(y_i\right) dy_i$, as $g\left(y_i\right) = \exp\left(-y_i^2\right)$ is an integrable function and $f\left(y_i\right)$ is a smooth-continuous function. Utilizing Gauss-Hermite rule, Equation (4.35) can be expressed as [[73], Eq. (25.4.46)]

$$U \approx \sum_{i=1}^{n} w_{i,n} \left[\begin{array}{c} \frac{FA}{\sqrt{\pi}} \left(1 + \ \tan^2 \left(\mu_1 + \sqrt{2\sigma_1^2} \ \ x_{i,n}\right)\right) \\ \times \mathrm{erfc}\left(\sqrt{C\gamma}\, A_0 \exp\left(-2\frac{d^2 \ \ \tan^2\left(\mu_1 + \sqrt{2\sigma_1^2} \ \ x_{i,n}\right)}{w_{z_{eq}}^2}\right)\right) \end{array} \right] + \sum_{i=1}^{n} w_{i,n} \left[\begin{array}{c} \frac{F(1-A)}{\sqrt{\pi}} \left(1 + \ \tan^2 \left(\mu_2 + \sqrt{2\sigma_2^2} \ \ x_{i,n}\right)\right) \\ \times \mathrm{erfc}\left(\sqrt{C\gamma}\, A_0 \exp\left(-2\frac{d^2 \ \ \tan^2\left(\mu_2 + \sqrt{2\sigma_2^2} \ \ x_{i,n}\right)}{w_{z_{eq}}^2}\right)\right) \end{array} \right] \tag{4.36}$$

where n is the order of approximation, $x_{i,n}$ is the set of roots defined by $H_n\left(x\right) = 0$ with $H_n\left(x\right)$ denoting the physicists Hermite polynomial. $w_{i,n}$ are the corresponding weights. Realizing Equation (4.22) and substituting Equation (4.36), Equation (4.21) is re-expressed as

$$\overline{BER} = \int_{0}^{\infty} U f_{h_t}\left(h_t\right) dh_t = \int_{0}^{\infty} \overline{BER}\left(h_t\right) f_{h_t}\left(h_t\right) dh_t \tag{4.37}$$

Substituting Equation (4.17) into Equation (4.37), average BER is re-arranged as

$$
\overline{BER} = \int_0^\infty \left[\begin{array}{c} \sum_{i=1}^{n} w_{i,n} \left\{ \begin{array}{c} \frac{FA}{\sqrt{\pi}} \left(1 + \tan^2\left(\mu_1 + \sqrt{2\sigma_1^2}\;\; x_{i,n}\right)\right) \\ \times \operatorname{erfc}\left(\sqrt{C\gamma}\, A_0 \exp\left(-2\frac{d^2 \;\tan^2\left(\mu_1 + \sqrt{2\sigma_1^2}\;\; x_{i,n}\right)}{w_{zeq}^2}\right)\right) \end{array} \right\} \\ + \sum_{i=1}^{n} w_{i,n} \left\{ \begin{array}{c} \frac{F(1-A)}{\sqrt{\pi}} \left(1 + \tan^2\left(\mu_2 + \sqrt{2\sigma_2^2}\;\; x_{i,n}\right)\right) \\ \times \operatorname{erfc}\left(\sqrt{C\gamma}\, A_0 \exp\left(-2\frac{d^2 \;\tan^2\left(\mu_2 + \sqrt{2\sigma_2^2}\;\; x_{i,n}\right)}{w_{zeq}^2}\right)\right) \end{array} \right\} \end{array} \right] \times \frac{1}{\sqrt{\sigma_t^2 2\pi}} h_t^{-1} \exp\left(-\frac{(\ln h_t - \mu_t)^2}{2\sigma_t^2}\right) dh_t \tag{4.38}
$$

A similar integral closed-from derivation approach is adopted for the remaining expression. In order to use Gaussian-Hermite quadrature method, let

$$
l^2 = \frac{\left(\ln\left(h_t\right) - \mu_t\right)^2}{2\sigma_t^2} \tag{4.39}
$$

After taking square root then exponential of both sides and re-arranging, Equation (4.39) becomes

$$
h_t = \exp\left(\sqrt{2\sigma_t^2}\; l + \mu_t\right) \tag{4.40}
$$

In order to apply the quadrature method, the derivative of Equation (4.40) is also computed as

$$
h_t\sqrt{2\sigma_t^2}\; dl = dh_t \tag{4.41}
$$

Using the newly introduced variable l , Equation (4.36) can be expressed as

$$U\left(l\right)=\sum_{i=1}^{n}w_{i,n}\left[\begin{array}{c}\frac{FA}{\sqrt{\pi}}\left(1+\ \tan^2\left(\mu_1+\sqrt{2\sigma_1^2}\ \ x_{i,n}\right)\right)\\ \times\ \mathrm{erfc}\left(\begin{array}{c}\sqrt{C\gamma}\ \exp\left(\sqrt{2\sigma_t^2}\ l+\mu_{tT}\right)A_0\\ \times\ \exp\left(-2\frac{d^2\ \ \tan^2\left(\mu_1+\sqrt{2\sigma_1^2}\ \ x_{i,n}\right)}{w_{zeq}^2}\right)\end{array}\right)\end{array}\right]$$
$$+\sum_{i=1}^{n}w_{i,n}\left[\begin{array}{c}\frac{F(1-A)}{\sqrt{\pi}}\left(1+\ \tan^2\left(\mu_2+\sqrt{2\sigma_2^2}\ \ x_{i,n}\right)\right)\\ \times\ \mathrm{erfc}\left(\begin{array}{c}\sqrt{C\gamma}\ \exp\left(\sqrt{2\sigma_t^2}\ l+\mu_t\right)A_0\\ \times\ \exp\left(-2\frac{d^2\ \ \tan^2\left(\mu_2+\sqrt{2\sigma_2^2}\ \ x_{i,n}\right)}{w_{zeq}^2}\right)\end{array}\right)\end{array}\right] \quad (4.42)$$

Therefore, by applying [[73], Eq. (25.4.46)] the average BER can be expressed as

$$\overline{BER}=\frac{1}{\sqrt{\pi}}\int_0^{\infty}U\left(l\right)\exp\left(-l^2\right)\ dl\approx\frac{1}{\sqrt{\pi}}\sum_{j=1}^{m}w_{j,m}U\left(x_{j,m}\right) \quad (4.43)$$

where m is the order of approximation, $x_{j,m}$ is the set of roots defined by $H_m\left(x\right)=0$ with $H_m\left(x\right)$ denoting the physicists Hermite polynomial. $w_{j,m}$ are the corresponding weights. Realizing $\left(1+\ \tan^2\left(\mu_1+\sqrt{2\sigma_1^2}\ \ x_{i,n}\right)\right)\approx 1$ and some further re-arrangements, the closed-form average BER for the GMM pointing error model with log-normal turbulent induced fading can be written as

$$\overline{BER}\approx\frac{F(1-A)}{\pi}\times\sum_{j=1}^{m}\sum_{i=1}^{n}w_{j,m}w_{i,n}\ \mathrm{erfc}\left(\exp\left(\frac{w_{zeq}^2(T)-2d^2\ \ \tan^2\left(\mu_2+\sqrt{2\sigma_2^2}\ \ x_{i,n}\right)}{w_{zeq}^2}\right)\right)$$
$$+\frac{FA}{\pi}\sum_{j=1}^{m}\sum_{i=1}^{n}w_{j,m}w_{i,n}\mathrm{erfc}\left(\exp\left(\frac{w_{zeq}^2(T)-2d^2\ \ \tan^2\left(\mu_1+\sqrt{2\sigma_1^2}\ \ x_{i,n}\right)}{w_{zeq}^2}\right)\right) \quad (4.44)$$

where $T=\sqrt{2\sigma_t^2}\ x_{j,m}+\mu_t+\ln\left(\sqrt{C\gamma A_0^2}\right)$.

4.4 Numerical Results

In this section, we present the numerical results for the BER performance. Unless otherwise noted, we assume $A_0 = 1$, $w_{L_{eq}} = 3.5$, $\sigma_t^2 = 0.78$ [72] and $\mu_t = -0.5\sqrt{\sigma_t^2}$ for well mixed waters in the presence of oceanic turbulence. We also assume a low value of $n = 5$, as PE tends to follow a linear behavior for higher values, whereas we assume $m = 20$, as the addition of turbulent induced fading has a more non-linear behavior.

Figure 4.8: *BER Plot for Increasing Wave Heights at 10 m Depth and 10 m/s Winds with 0 Degrees Wind Heading ($d = 10$ m, $v = 10$ m/s and $h = 1$).*

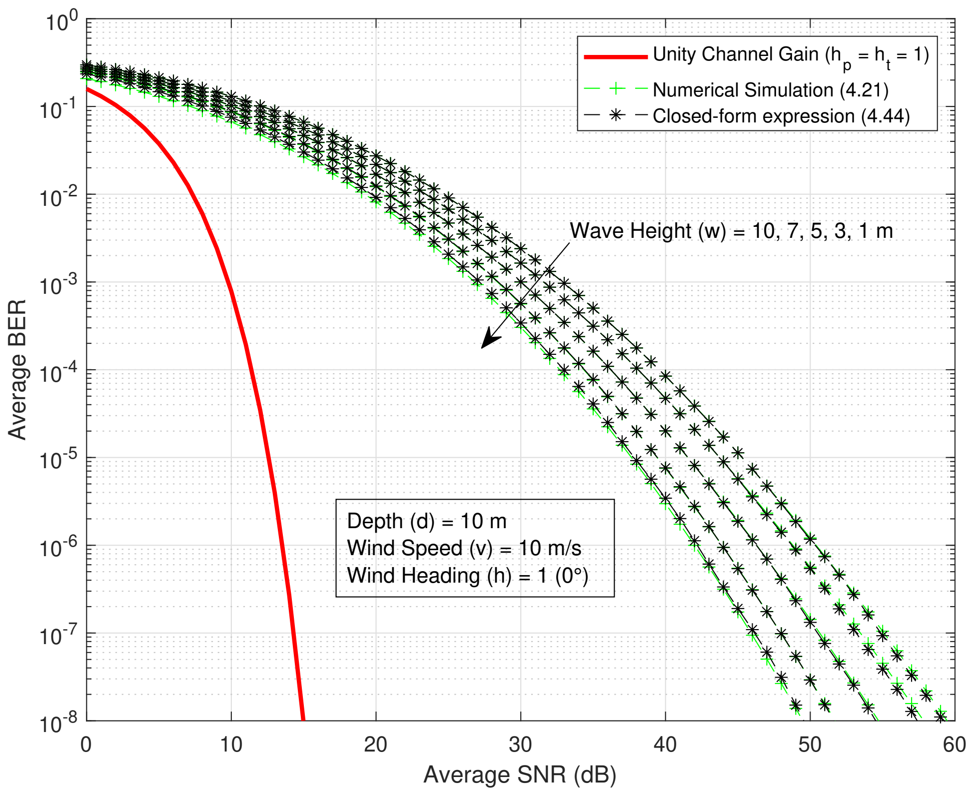

In Figure 4.8, we investigate the effect of increasing wave height on BER. We assume $v = 10$ m/s, $d = 10$ m and $h = 1$. We present the BER assuming that the wave height takes values in the range of $w = 1$ m to 10 m, see Table 4.4 for GMM values.

As the wave height increases, BER performance significantly deteriorates. For example, to achieve a BER of 10^{-4}, SNR of 33 dB is required for $w = 1$ m, which would be considered low oceanic turbulence. The required SNR increases to 40 dB for $w = 10$ m, a typical value for very turbulent oceanic states. In the figure, we have further included the numerical computation of the integral Equation (4.21) as a benchmark to demonstrate the accuracy of the derived approximate expression in Equation (4.44). It is observed that the derived expression converges to the simulation results for practical SNR values.

In Figure 4.9 below, we investigate the effect of increasing wind speed on the BER.

Figure 4.9: *BER Plot for Increasing Wind Speeds at 10 m Depth and 4 m High Waves and Heading 0 Degrees ($d = 10$ m, $w = 4$ m and $h = 1$).*

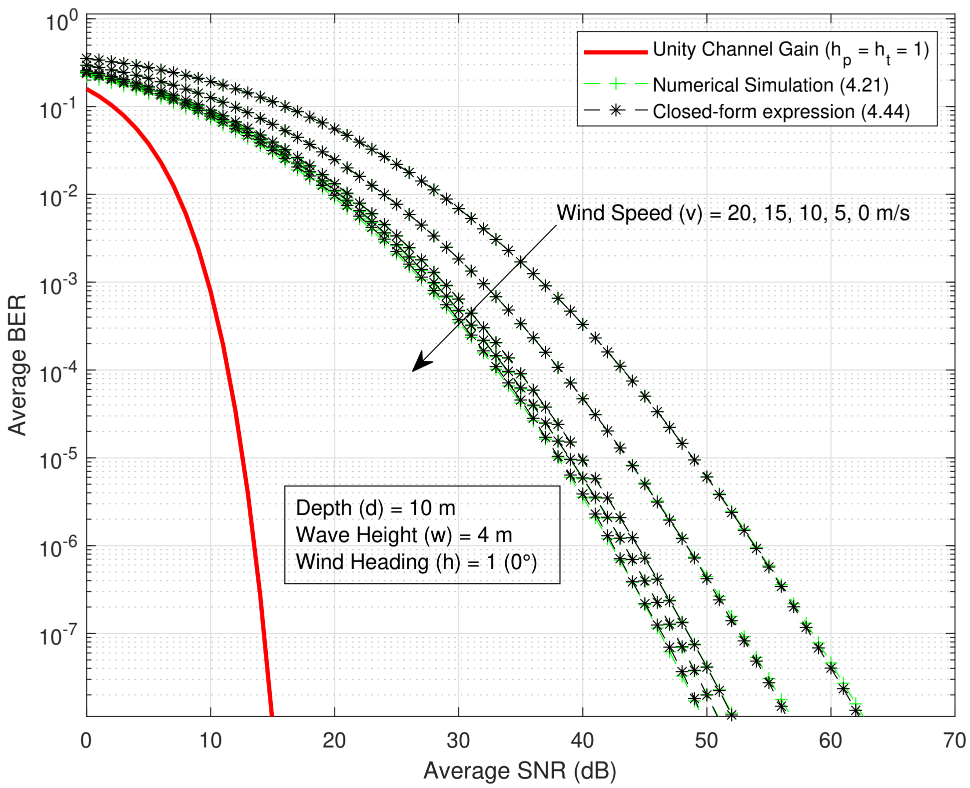

We consider $w = 4$ m, $d = 10$ m and $h = 1$. Wind speed v is varied between

0 m/s, no wind, and 20 m/s, gale [74]. As the wind speed increases, there is noticeable change in the BER performance. For instance, when wind speed doubles from 10 m/s to 20 m/s, the required SNR to achieve a BER of 10^{-4} increases by 7 dB. This result is expected as the wind speed increases, the sea surface becomes more turbulent and the buoy tends to move with rotations with higher magnitude.

In Figure 4.10 below, we investigate the effect of increasing water depth on the BER.

Figure 4.10: *BER Plot for Increasing Depth for 1 m High Waves and 5 m/s Winds, and 45 Degrees Wind Heading ($w = 1$ m, $v = 5$ m/s and $h = 2$).*

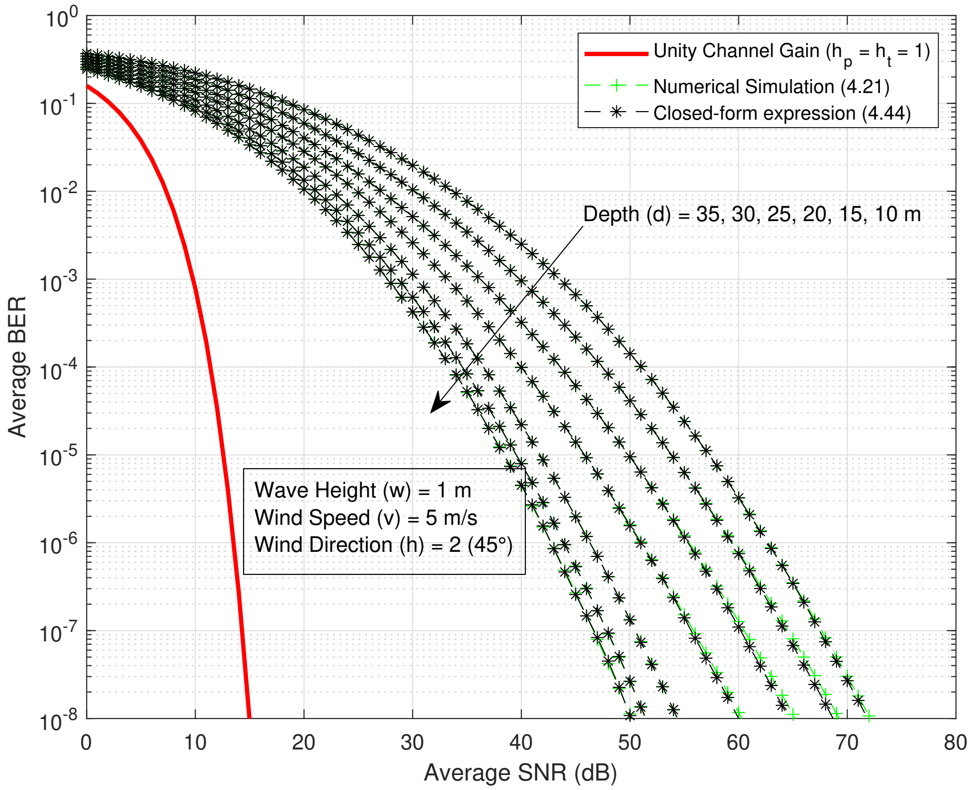

We consider $w = 1$ m, $v = 5$ m/s and $h = 2$. Water depth d is varied between 10 m to 35 m. With the increasing depth, significant changes in the BER are observed. For instance, to achieve a BER of 10^{-4}, SNR of 32 dB is required for $d = 10$ m. This increases to 51 dB for $d = 35$ m. This drastic deterioration is primarily attributed to the increased propagation distance at greater water depths, whereby any rotational deviation of the buoy leads to a more significant misalignment of the optical beam, resulting in increased beam divergence and degradation of channel performance.

In Figure 4.11 below, we investigate the effect of changing wind direction on the BER.

Figure 4.11: *BER Plot for Changing Wind Directions for 3 m High Waves and 10 m/s Winds at 20 m Depth ($w = 3$ m, $v = 10$ m/s and $d = 20$).*

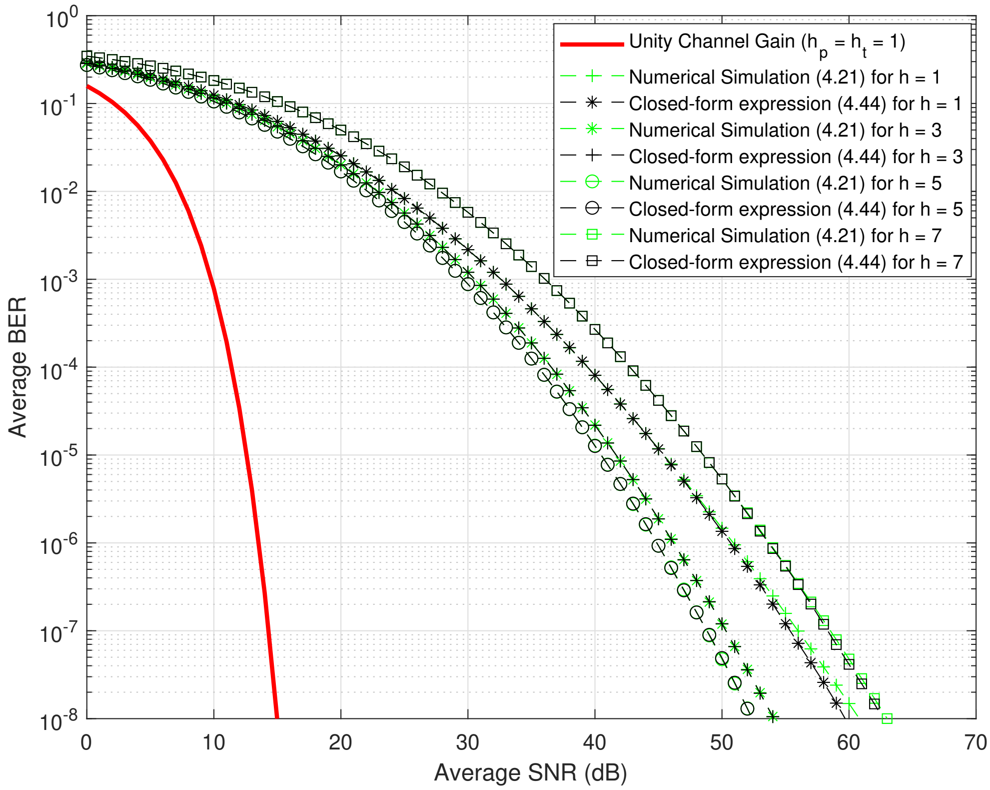

We consider $w = 3$ m, $v = 10$ m/s and $d = 20$ m. Wind direction is varied from 1 to 7, representing the cases described in Table 4.2. It is observed that for some cases when the wind and waves do not have the same heading, BER tends to get better for some directions, whereas it gets worse for other directions. For instance, to achieve a BER of 10^{-4}, SNR of 39 dB is required for $h = 1$. However, this decreases to 35 dB for $h = 5$, but then goes up to 42 dB for $h = 7$. This behavior arises from the constructive and destructive interactions between wind and wave forces, further influenced by the buoy's physical characteristics, including its center of gravity and moment of inertia.

4.5 Conclusions

In the existing literature on buoy-based UWOC systems, the effects of pointing error and turbulence induced fading on the channel performance are provided without relating them to the actual physical behavior of the buoy under the sea disturbances including waves and winds. In practice, the pitch and roll motion of an ocean buoy is greatly affected by these environmental parameters and are not independent. Based on extensive simulations it was seen that roll, pitch and tilt motions of an ocean buoy follows a GMM distribution rather than the widely assumed Gaussian distribution. It was also seen that focusing only on tilt motion to study the channel performance was more appropriate as it appears to have a less complex structure compared to that of roll and pitch. Through polynomial fitting, we proposed closed-form expressions to estimate the GMM curve parameters for the tilt angle as a function of wave height, wind speed and wind direction. Our results demonstrate that the tilt angle increases as wave height and wind speed increase. Afterwards, we derived the closed-form BER expression for the GMM pointing error case along with turbulence induced log-normal fading as a function of these environmental parameters and confirmed its accuracy through Monte Carlo simulations. Through BER analysis, we quantified the performance degradations due to wave height and wind loads for a realistic ocean buoy in waters of varying depths.

5. MODELLING OF POINTING ERRORS IN AERIAL FSO LINKS CAUSED BY WIND TURBULENCE

5.1 Introduction

UAV based FSO communication systems are getting noticeable attention in recent years. The inherent mobility and operational flexibility of UAVs make them highly advantageous in FSO networks, facilitating rapid deployment and enhancing connectivity in remote or inaccessible regions [75]. These systems can also be utilized very rapidly during emergencies such as natural disasters and can provide crucial benefits for the public. Given these attributes, the integration of UAVs into FSO networks is projected to become more prevalent in the near future and foster more innovative communication solutions. Additionally, FSO technology offers a secure and interference-resistant communication channel, rendering it particularly attractive for military applications [6, 76, 77].

Accurate channel modelling plays an important role in the thorough analysis of UAV based FSO links. Various analytical models have been developed in the literature for hovering based UAVs. In some works, inter UAV FSO links are also considered. Misalignment mitigation has been studied in numerous studies [78, 79, 80]. Also Pointing, Acquisition and Tracking (PAT) for FSO links are analyzed in number of works. While majority of the works assume a flat or a circular receiver, there exists some studies that have assumed a spherical receiver as well [81]. In some works, a broader variety of channels such as Ground-to-UAV (G2U), UAV-to-UAV (U2U) and UAV-to-Ground (U2G) channels are considered [82].

Other works exist where analytical models for hovering UAV FSO communications are proposed while incorporating not only FSO but also RF channels as in conjunction [83]. In these studies the ergodic channel capacity is presented for the relay based networks built of UAVs. In further studies, the throughput of such systems are analyzed. Some works also look at the AoA effects on the FSO channel [75, 84, 85, 86], as due to the orientation fluctuations in a hovering UAV, the AoA has an effect on channel outage.

However, similar to both terrestrial FSO and UWOC studies, not many studies exist where the behavior of an UAV-to-Ground optical channel is simulated extensively for statistical analysis. Majority of the works simply assume a Gaussian distribution for all axes of interest, whether position or orientation, and derive the pointing error models accordingly. As expected, all the derived pointing error models are very similar to the terrestrial models previously discussed [11].

In this study, we try to fill this gap by correlating the behavior of the pointing error to the underlying physical phenomenon. Towards this end we model a realistic quadcopter UAV, hovering at a set altitude in the presence of wind. While altering the wind conditions, the hover behavior of UAV is analyzed statistically. Afterwards a PDF of pointing error is derived and presented. The rest of this chapter is as follows, in Chapter 5.2 we present the flight dynamics and hovering behavior analysis of the quadcopter UAV model in the presence of industry standard wind models. Then in Chapter 5.3, we derive a pointing error formulation for an UAV-to-Ground FSO system mounted on a quadcopter UAV. Finally, we conclude in Chapter 5.4.

5.2 Flight Dynamics and Hover Simulation of the Quadcopter UAV in the Presence of Winds

5.2.1 Quadcopter UAV

A quadcopter UAV is a type of rotary-wing aircraft that utilizes four rotors for lift and maneuverability. Unlike fixed-wing UAVs, quadcopters achieve flight stability through differential rotor speeds, allowing precise control over altitude, pitch, roll, and yaw. This configuration provides enhanced agility, making quadcopters suitable for applications such as aerial surveillance, environmental monitoring, and autonomous navigation.

These UAVs house four brushless DC motors arranged in a symmetrical configuration to achieve stable flight. These motors are typically mounted on the ends of a cross-shaped or X-shaped frame, with two rotating clockwise and two counterclockwise to maintain balance and control. The propellers attached to these motors generate lift, and their speed variations allow for precise maneuverability in terms of pitch, roll, and yaw and provide 6-DOF motion [87]. The frame is often constructed from lightweight materials such as carbon fiber or aluminum to optimize durability and flight efficiency. Shown below in Figure 5.1 is the diagram of a UAV model used for simulation in this work.

Figure 5.1: *Overview of a Quadcopter UAV.*

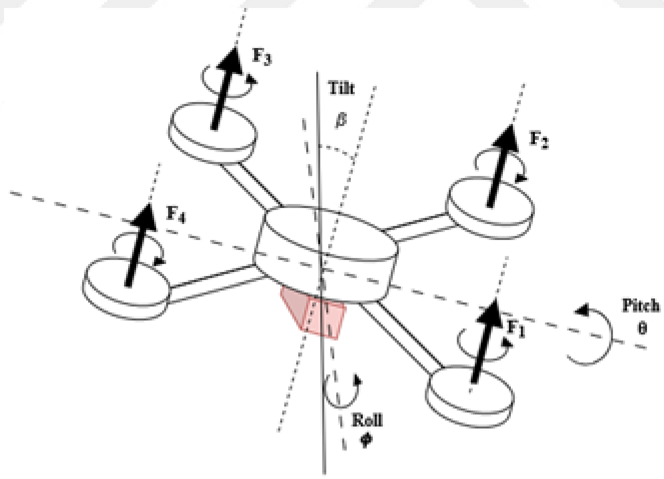

5.2.2 Flight Dynamics of a Quadcopter UAV

The flight dynamics of the drone are modeled using a 6-DOF rigid body model, which describes the translational and rotational motions in three-dimensional space. The drone's motion is governed by Newton-Euler equations [88]. Defined in Equation (5.1) below is the translational motion

$$m\frac{d\mathbf{v}}{dt} = F_{Total} = F_{thrust} + F_{drag} + F_{lift} + mg \tag{5.1}$$

where m is the quadcopter mass, $\mathbf{v} = [v_x, v_y, v_z]^T$ is the velocity vector in three axes, F_{Total} is the sum of all external forces, namely F_{thrust} is the thrust force, F_{drag} is the drag force, F_{lift} is the lift force and mg is the force due to the weight of the quadcopter as g is the gravitational acceleration.

F_{thrust} is generated by the quadcopter's rotors and acts primarily along the z-axis. Its magnitude depends on the rotor speed and propeller characteristics. F_{drag} is a resultant of the aerodynamic drag that opposes the quadcopter's motion relative to the air. It is modeled as proportional to the square of the velocity relative to the air as shown in Equation (5.2) below

$$F_{drag} = -\frac{1}{2}\rho C_D A v^2 \tag{5.2}$$

where ρ is air density, C_D is the drag coefficient, A is the reference area, and v is the quadcopter velocity relative to wind and $v = dp/dt$ is the aerodynamic lift force and can occur due to body shape and airspeed of the quadcopter [88]. Defined in Equation (5.3) below is the rotational motion

$$\mathbf{I}\frac{d\omega}{dt} + \omega \times (\mathbf{I}\omega) = M_{total} = M_{thrust} + M_{drag} + M_{lift} \tag{5.3}$$

where $\mathbf{I}$ is the quadcopter's moment of inertia matrix, $\omega = [p, q, w]^T$ are the body angular rates, namely roll, pitch and yaw as shown in Figure 5.1. M_{Total} is the total moment vector acting on the quadcopter and it consists of the moments generated by previously mentioned force vectors.

Orientation of the quadcopter consists of Euler angles [88]: roll (ϕ), pitch (θ) and yaw (ψ) and rotation matrix from quadcopter body frame to inertial frame is given in Equation (5.4) below

$$\mathbf{R} = R_x(\phi)\, R_y(\theta)\, R_z(\psi) \tag{5.4}$$

where

$$R_x(\phi) = \begin{bmatrix} 1 & 0 & 0 \\ 0 & \cos\phi & -\sin\phi \\ 0 & \sin\phi & \cos\phi \end{bmatrix} \tag{5.5}$$

$$R_y(\theta) = \begin{bmatrix} \cos\theta & 0 & \sin\theta \\ 0 & 1 & 0 \\ -\sin\theta & 0 & \cos\theta \end{bmatrix} \tag{5.6}$$

$$R_z(\psi) = \begin{bmatrix} \cos\psi & -\sin\psi & 0 \\ \sin\psi & \cos\psi & 0 \\ 0 & 0 & 1 \end{bmatrix} \tag{5.7}$$

The time derivatives of Euler angles are related to the body angular rates [88] as shown in Equation (5.8) below.

$$\begin{bmatrix} \dot{\phi} \\ \dot{\theta} \\ \dot{\psi} \end{bmatrix} = \begin{bmatrix} 1 & \sin\phi\tan\theta & \cos\phi\tan\theta \\ 0 & \cos\phi & -\sin\phi \\ 0 & \sin\phi/\cos\theta & \cos\phi/\cos\theta \end{bmatrix} \begin{bmatrix} p \\ q \\ w \end{bmatrix} \tag{5.8}$$

5.2.3 *Controller Design of a Quadcopter UAV*

Our quadcopter uses a cascaded PID control architecture to stabilize and track the desired position and orientation [7]. An overview of the cascaded control system is shown in Figure 5.2 below.

Figure 5.2: *Cascaded Controller System of the Simulated Quadrotor UAV.*

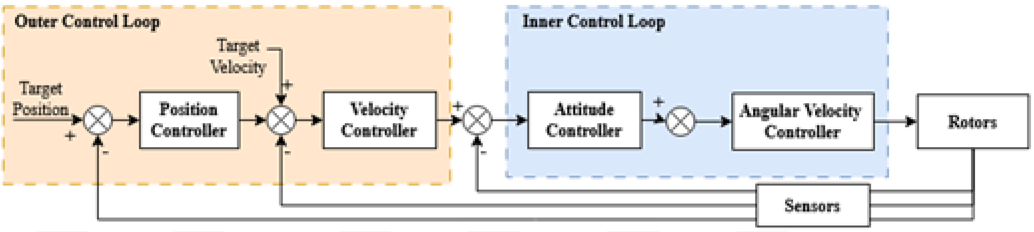

Matlab's Aerospace Toolbox offers a UAV Toolkit that offers cascaded controller systems [9]. For realistic results, DJI Matrice 300 RTK quadcopter UAV [89] technical specifications are used in the simulated model.

5.2.4 *Wind Models*

To reliably model the UAV hovering flight under the influence of winds, various wind models are studied. In aerospace engineering, particularly for quadcopter UAV simulations, accurate wind modeling is essential to evaluate flight dynamics, control system robustness, and mission success under realistic environmental conditions.

A commonly used model is the Dryden wind turbulence model, which represents atmospheric turbulence as a stationary stochastic process based on power spectral density functions. It is especially favored for its relatively simple mathematical structure and compatibility with linear systems, making it ideal for real-time simulation and control system design. The model assumes a steady-state turbulence field with spatial correlation and white-noise temporal behavior, making it suitable for low- to mid-altitude flight scenarios [90].

Another widely applied model is the von Kármán wind turbulence model, which offers a more physically accurate representation of atmospheric turbulence, particularly at higher altitudes and for long-duration disturbances. Unlike the Dryden model, the von Kármán model has a continuous spectral slope at low frequencies, providing a more realistic depiction of wind gusts and turbulence experienced during cruise or high-speed maneuvers. It also aligns better with empirical data collected from atmospheric measurements and flight tests. As such, it is frequently used in certification-level aircraft simulations and high-fidelity aerospace modeling environments [90].

Even though Dryden wind turbulence model is widely used in UAV simulations due to its mathematical simplicity, for more accurate modeling of atmospheric turbulence, especially at low altitudes, the von Kármán Wind Turbulence Model is often preferred. The von Kármán model treats the linear and angular velocity components of continuous gusts as spatially varying stochastic processes and specifies each component's power spectral density. This allows for a more realistic representation of atmospheric turbulence, particularly for low-altitude UAV operations. It provides a better match to observed continuous gusts and is the preferred model of the United States Department of Defense in most aircraft design and simulation applications [91].

In this study von Kármán wind model is adopted as it is readily available in Matlab's Aerospace toolbox. Shown in Figure 5.3 below is the generated wind forces in X, Y, Z directions according to von Kármán wind model with 15 m/s initial winds and 315 degrees wind heading for a simulation duration of 18000 seconds.

Figure 5.3: *Wind Forces in X, Y, Z Directions Generated by von Kármán Wind Model with 15 m/s Initial Winds and 315 Degrees Wind Heading for Simulation Duration of 18000 Seconds.*

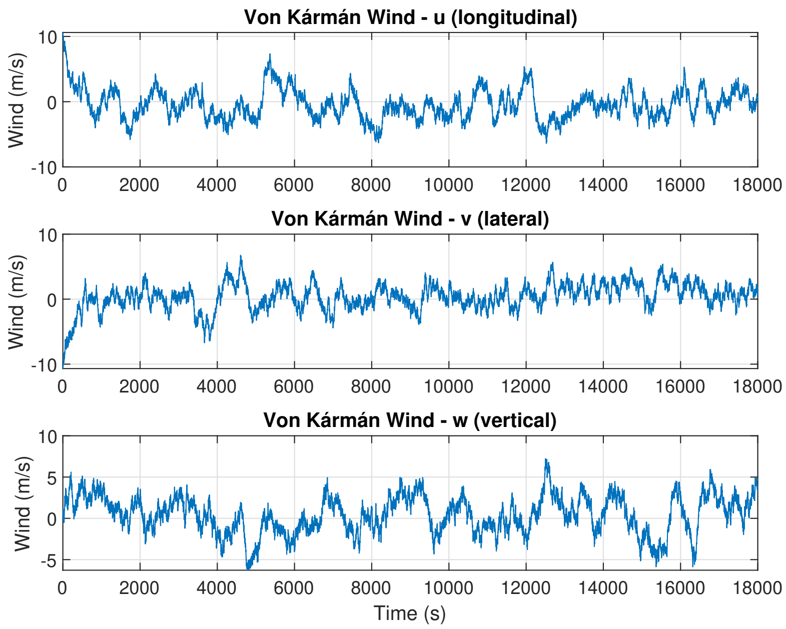

5.2.5 *Hovering Behavior of Quadcopter UAV under the Influence of Winds*

Extensive simulations are carried out to model the statistical behavior of UAV rotational motion and translational displacement under various wind speeds and directions. 0.1 m/s to 25 m/s winds were tested along with all major wind directions. Shown in Figure 5.4 below are the X, Y, Z positions of the quadcopter hovering in 20 m/s winds.

Figure 5.4: *X, Y, Z Positions of the Quadcopter Hovering at 100 meters Experiencing 20 m/s Winds.*

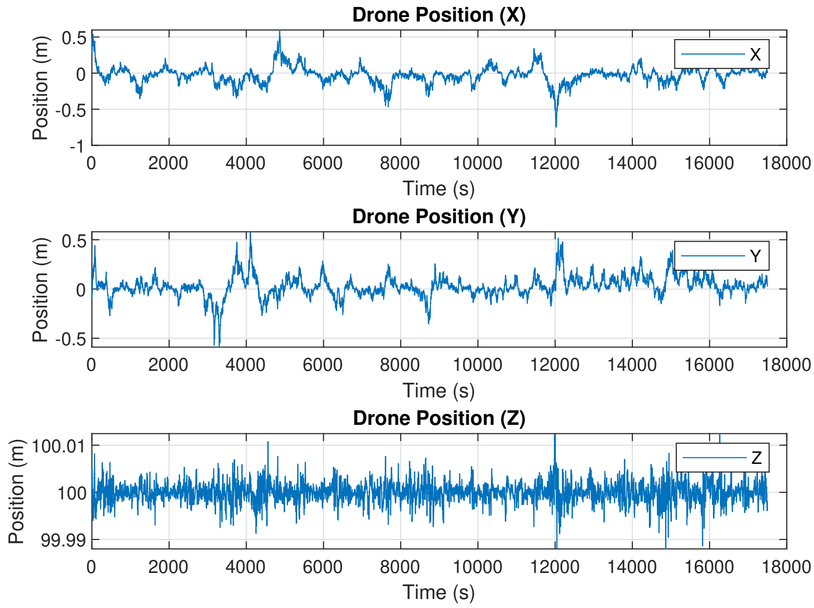

Shown below in Figure 5.5 is the roll and pitch behavior of a quadcopter hovering in 15 m/s winds with 315 degrees heading.

Figure 5.5: *Roll and Pitch Behavior of a Quadcopter Hovering at 100 meters and Experiencing Winds of 15 m/s with 315 Degrees Heading.*

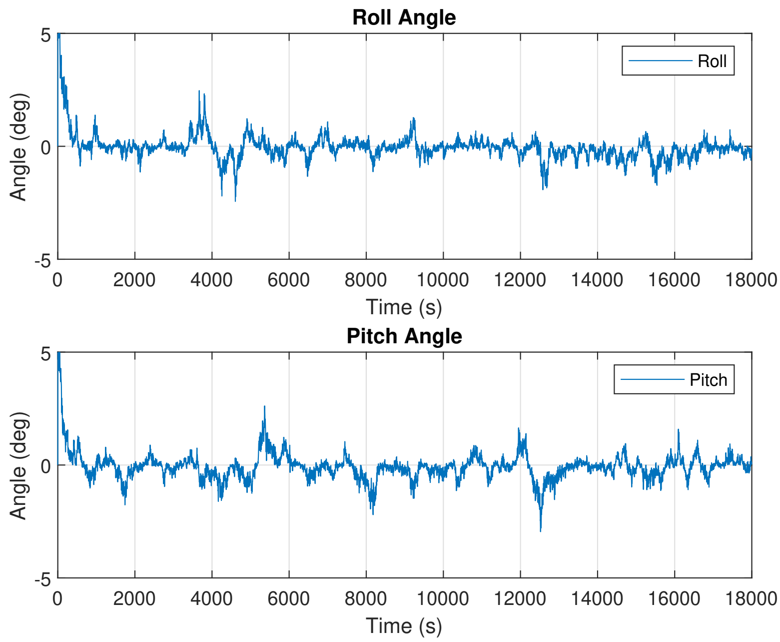

Shown in Figure 5.6 is the XY scatter plot of the UAV for the same flight conditions.

Figure 5.6: *XY Scatter Plot of the UAV Hovering at 100 meters and Experiencing 15 m/s Winds at 315 Degrees Heading.*

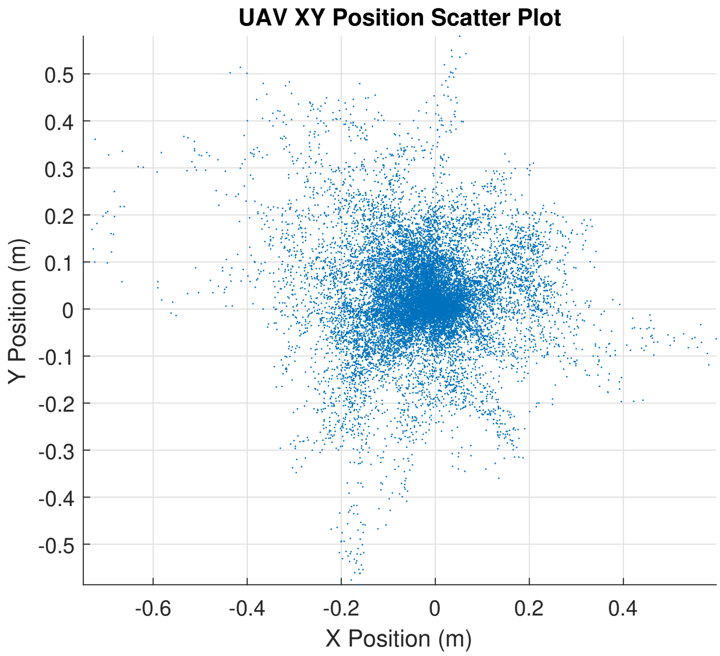

Shown in Figure 5.7 below is the UAV position density heatmap for the same flight conditions.

Figure 5.7: *The Density Heatmap of the UAV Hovering at 100 meters and Experiencing 15 m/s Winds at 315 Degrees Heading.*

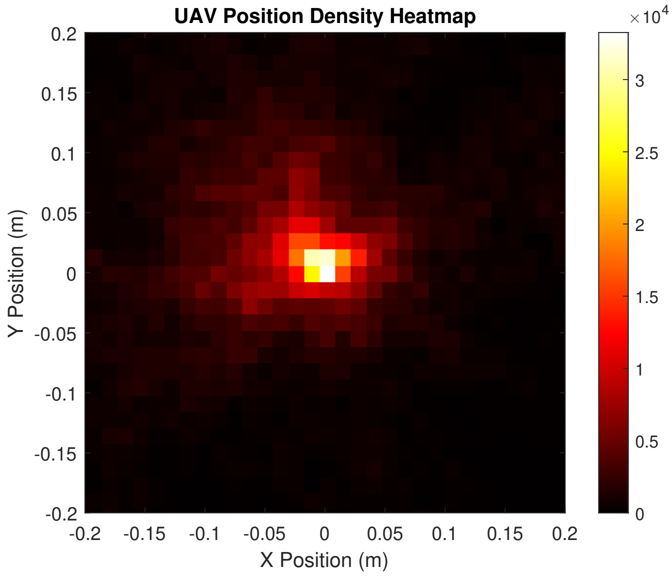

Shown in Figure 5.8 is the 2D histogram of the UAV position for the same flight conditions

Figure 5.8: *2D Position Histogram of the UAV Hovering at 100 meters and Experiencing 15 m/s Winds at 315 Degrees Heading.*

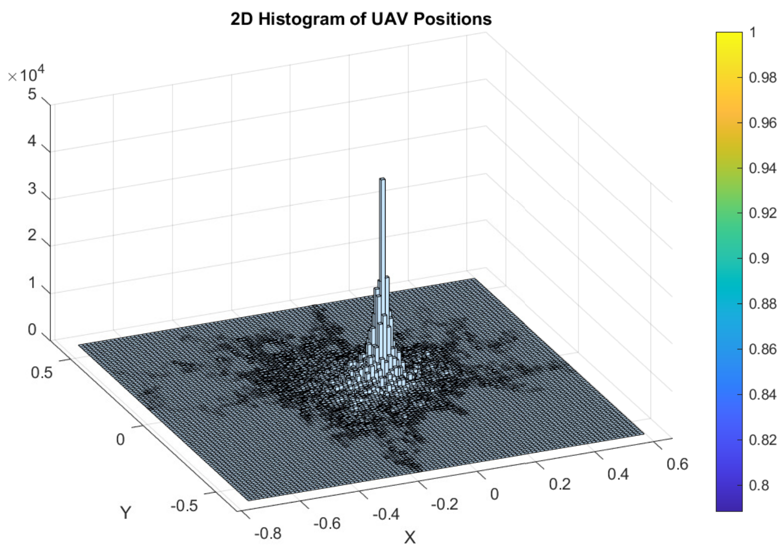

5.2.5.1 Rotational Behavior

Statistical analysis of the rotational motion reveals that the distributions for roll and pitch angles do not follow Gaussian as widely assumed in literature. Shown in Figure 5.9 below is the histograms for both roll and pitch angles for a quadcopter hovering at 100 m for 18000 seconds under the presence of von Kármán winds.

Figure 5.9: *Roll and Pitch Angle Distributions for Quadcopter Hovering at 100 meters for 18000 seconds Under the Presence of von Kármán Winds.*

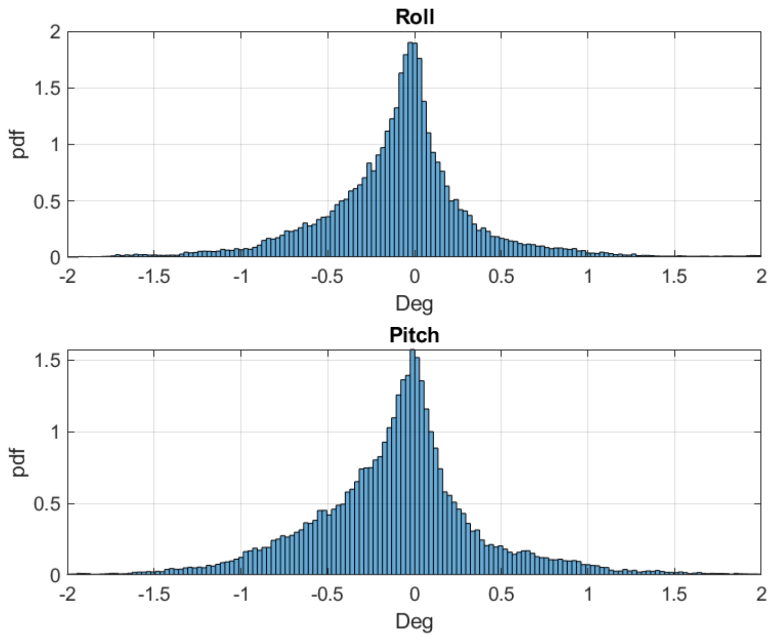

It is noticed that both curves are closer to a t location-scale distribution rather than Gaussian. It is also observed that the roll and pitch PDFs also get affected by the wind incident angle. Afterwards, tilt angle of the UAV is computed according to Equation (4.2) and its histogram is obtained. It is seen that the tilt angle does not get affected by the wind direction because of the physical layout of the quadcopter's thrust generating motors. Once the PDF of the tilt motion is obtained, Matlab's fitdist function is used to fit a log-normal distribution on the simulation data and a good match is achieved. Shown in

Figure 5.10 below is the tilt angle histogram of the aforementioned test case along with Matlab's fitted log-normal PDF.

Figure 5.10: *Tilt Angle Distribution and Log-Normal Curve Fitting for Quadcopter Hovering at 100 meters for 18000 seconds Under the Presence of von Kármán Winds.*

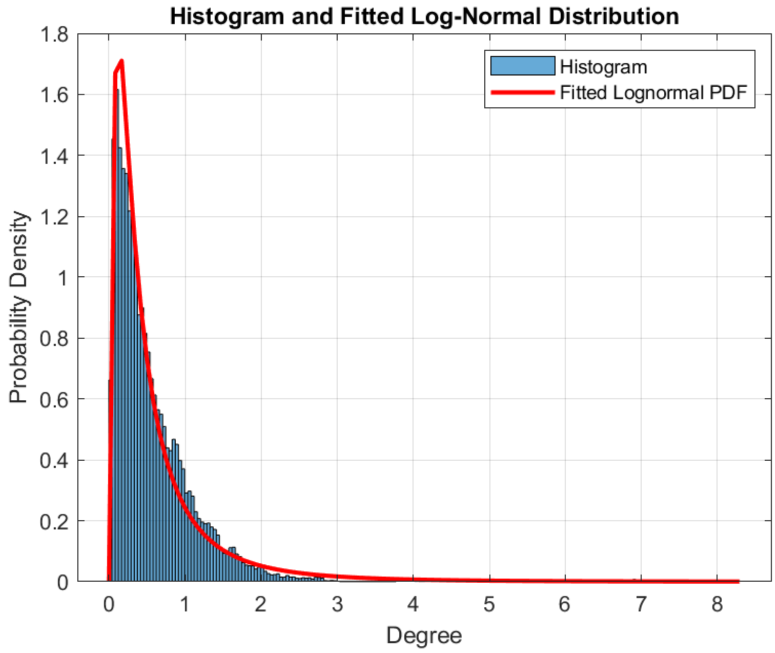

Log-normal distribution is a continuous probability distribution whose logarithm is normally distributed. The PDF of log-normal distribution is given as

$$\frac{1}{x\sigma\sqrt{2\pi}} \exp\left(-\frac{(\ln x - \mu)^2}{2\sigma^2}\right) \tag{5.9}$$

where μ is the expected value, and σ is the standard deviation. Log-normal PDF parameters, μ and σ, are computed for each simulation case. These parameters are then used for 3rd order polynomial fitting to obtain a closed-form relationship between wind speed and tilt PDF as shown in Equations (5.10)- (5.11) below. RMSE of 0.0025-0.0029 is achieved.

$$a_\mu v^3 + b_\mu v^2 + c_\mu v + d_\mu = \mu_f \tag{5.10}$$

$$a_\sigma v^3 + b_\sigma v^2 + c_\sigma v + d_\sigma = \sigma_f \quad (5.11)$$

The coefficients are given in Table 5.1.

Table 5.1: *3^{rd} Order Polyfit Coefficients for the Closed-form Relationship between the Wind Speed and Log-normal Curve Parameters.*

Coefficient	Value	Coefficient	Value
a_μ	-2.8673e-05	a_σ	9.8953e-06
b_μ	0.00093849	b_σ	-8.0197e-05
c_μ	-0.0039616	c_σ	0.00028141
d_μ	-0.0073291	d_σ	1.0159

Analysis indicates that the estimated values provide a good curve estimation for the tilt angle PDF. Shown below in Figure 5.11 are the histogram and closed-form approximation for the case of quadcopter hovering at 100 m under 12 m/s winds. Overall a good match is observed.

Figure 5.11: *Histogram and 3^{rd} Order Closed-form Approximation for the Case of UAV Hovering at 100 m Under 12 m/s von Kármán Winds.*

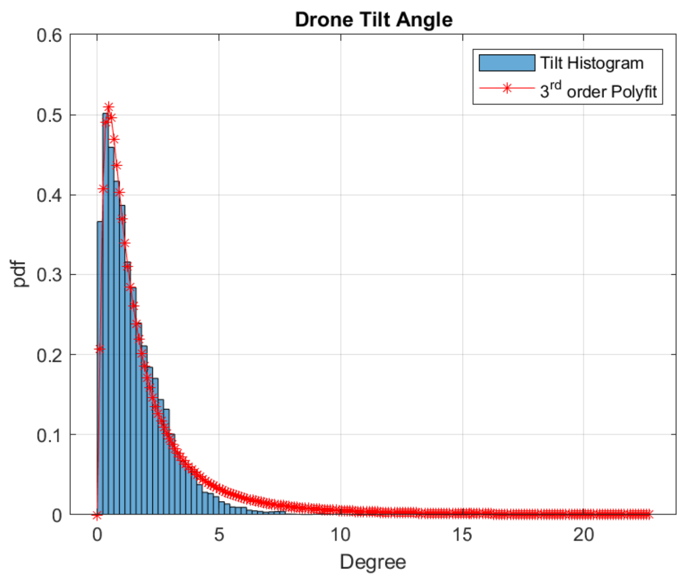

5.2.5.2 Translational Behavior

Statistical analysis of the translational motion reveals that the distributions for X and Y positions do not follow a widely assumed Gaussian distribution. Shown in Figure 5.12 below are the histograms for X and Y positions of the UAV hovering at 100 meters while experiencing 16 m/s winds.

Figure 5.12: *PDFs for X and Y Positions of the UAV Hovering at 100 meters while Experiencing 16 m/s Winds.*

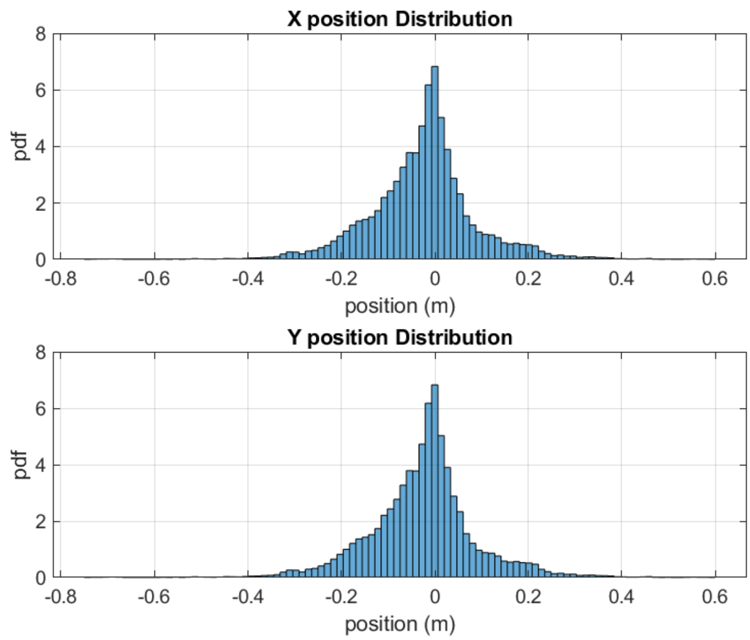

It can be seen that neither curve fully follows a Gaussian behavior; instead, both are closer to a t location-scale distribution. To follow, radial distance, simply $\mathbf{r} = \sqrt{r_x^2 + r_y^2}$, and its histogram are shown in Figure 5.13 below. A Gamma distribution is fitted to the radial distance PDF and overall a good match is achieved.

Figure 5.13: *Radial Distance Time Series and PDF Along with Fitted Gamma Distribution for the UAV Hovering at 100 meters while Experiencing 15 m/s Winds.*

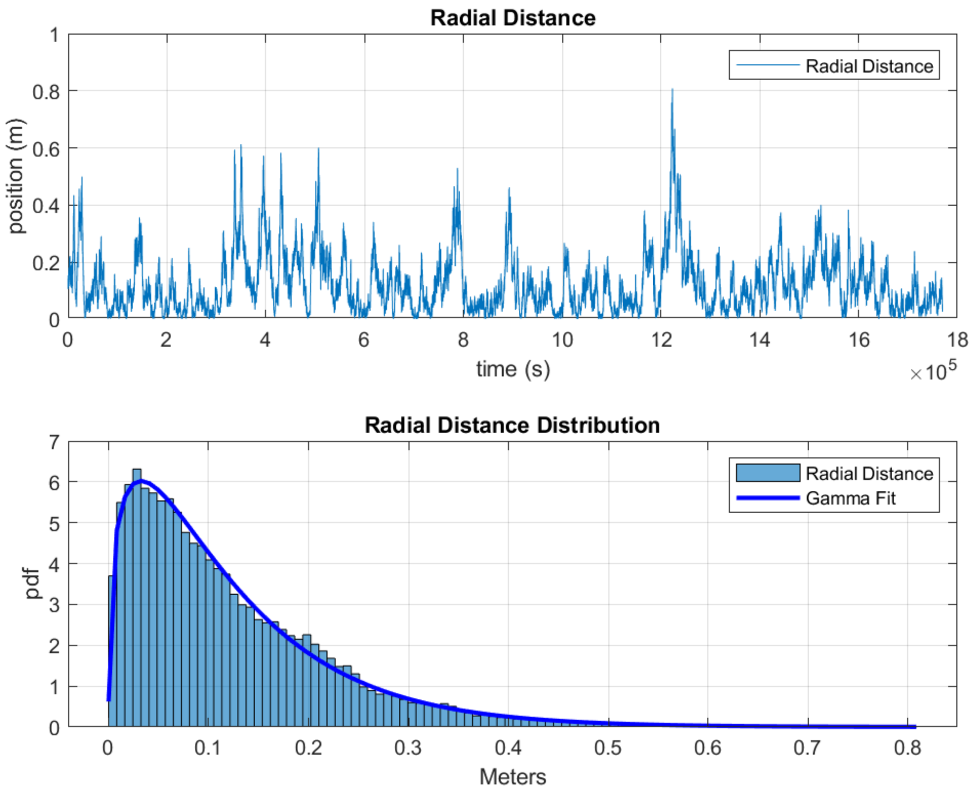

A t location-scale distribution is useful for modeling data with heavier tails than the normal distribution. It approaches normal distribution as the shape parameter approaches infinity, while smaller yields to heavier tails. The PDF of the t location-scale distribution is given as

$$f\left(x\right) = \frac{\Gamma\left(\frac{\upsilon+1}{2}\right)}{\sigma\sqrt{\upsilon\pi}}\left[\frac{\upsilon + \left(\frac{x-\mu}{\sigma}\right)^2}{\upsilon}\right]^{-\left(\frac{\upsilon+1}{2}\right)} \tag{5.12}$$

where μ is the location parameter and σ is the scale parameter. In order to double verify that two t location-scale distributions, when evaluated as $\mathbf{r} = \sqrt{r_x^2 + r_y^2}$, results in a

Gamma distributions, two random t location-scale distribution curves were generated by Matlab and afterwards the resultant value $\mathbf{r} = \sqrt{r_x^2 + r_y^2}$ are plotted in Figure 5.14 below.

Figure 5.14: *Two Random Generated t Location-Scale Distributions as X and Y position PDFs for 7 m/s Winds (top), and the Resultant Lateral Radial Distance Vector Gamma Distribution (bottom).*

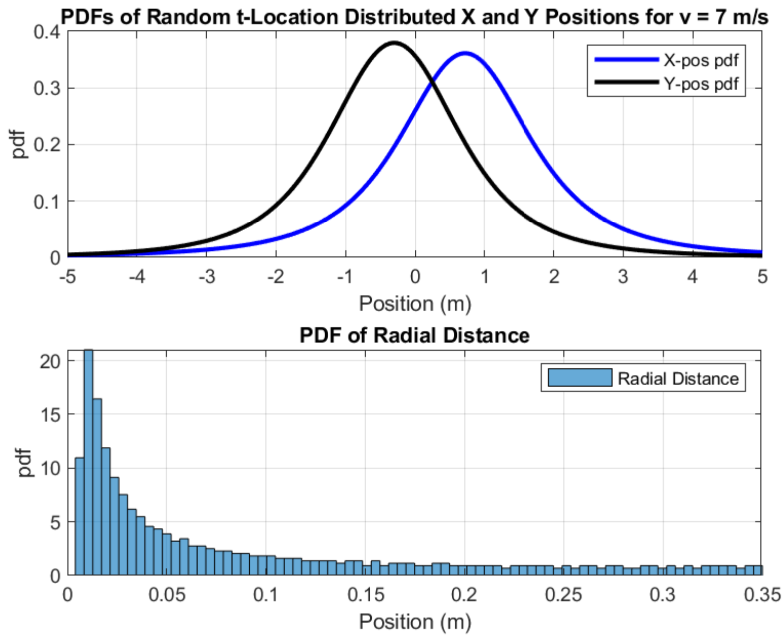

It can be seen that two t location-scale distributions, when squared and added together lead to a Gamma distribution. Gamma distribution is a continuous two parameter probability distribution. It has two parameters, shape parameter a and scale parameter b. The PDF of Gamma distribution is given as

$$f(x) = \frac{1}{\Gamma(a)\, b^a} x^{a-1} e^{-x/b} \tag{5.13}$$

where $\Gamma(.)$ is the Gamma function.

Gamma PDF shape and scale parameters are computed for each simulation case. These parameters are then used for 3$^{\text{rd}}$ order polynomial fitting to obtain a closed-form relationship between wind speed and tilt PDF as shown in Equations (5.14)- (5.15) below. RMSE of 0.0004-0.0017 is achieved.

$$a_a v^3 + b_a v^2 + c_a v + d_a = a_f \tag{5.14}$$

$$a_b v^3 + b_b v^2 + c_b v + d_b = b_f \tag{5.15}$$

The coefficients are given in Table 5.2 .

Table 5.2: *3rd Order Polyfit Coefficients for the Closed Form Relationship between the Wind Speed and Translational Radial Distance Gamma Distribution Parameters.*

Coefficient	Value	Coefficient	Value
a_a	-3.387e-05	a_b	9.204e-06
b_a	0.00091969	b_b	-0.00020414
c_a	-0.0063982	c_b	0.001354
d_a	1.3805	d_b	0.37214

Analysis indicates that the estimated values provide a good curve estimation for the lateral radial distance PDF. Shown below in Figure 5.15 are the histogram and closed-form approximation for the case of hovering at 100 m under 10 m/s winds. Overall a good match is observed.

Figure 5.15: *Histogram and 3rd Order Closed-form Approximation for Lateral Radial Distance for the Case of UAV Hovering at 100 m Under 10 m/s von Kármán Winds.*

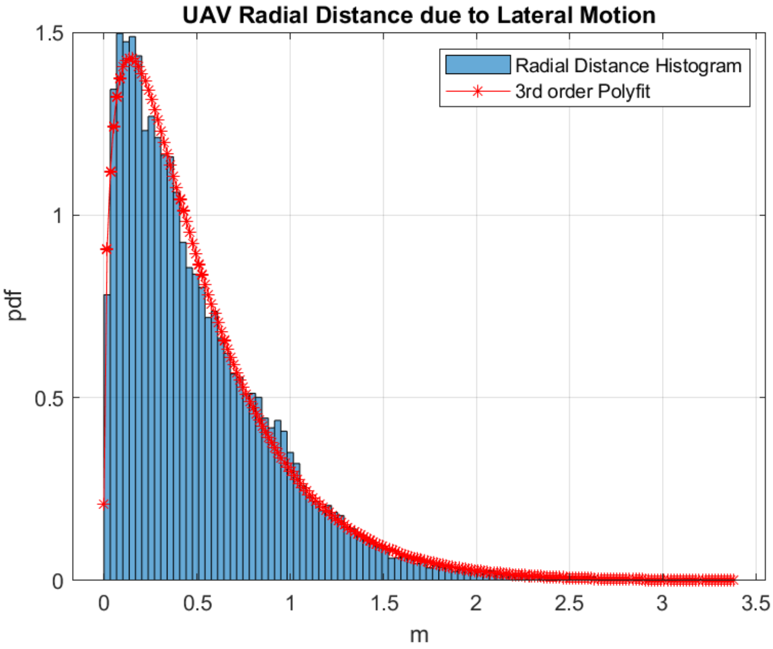

5.3 Pointing Error Model for a Hovering Quadcopter in the Presence of Wind

In the case of a quadcopter drone hovering at a fixed altitude, the PE can be caused mainly by rotational and translational motions. Shown in Figure 5.16 below are the corresponding radial displacement vectors caused by each motion and the overall resultant displacement vector.

Figure 5.16: *Pointing Error Caused by Lateral and Rotational Motion During Hover Under Wind.*

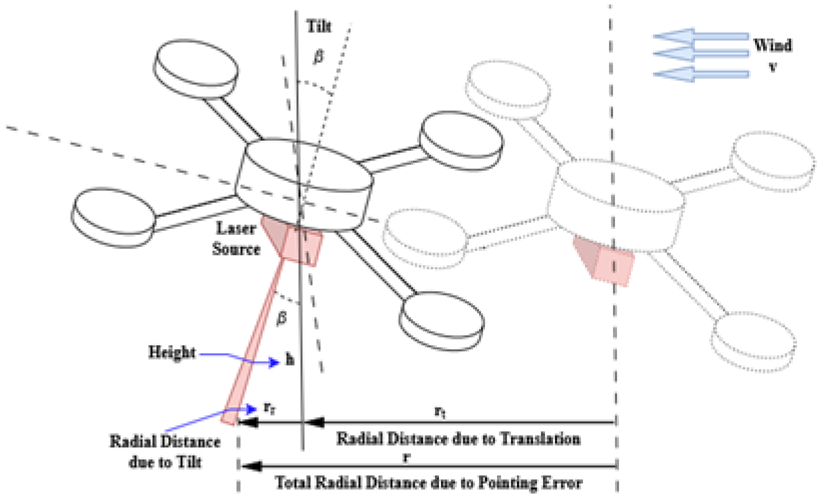

Radial displacement r is defined as

$$\mathbf{r} = \mathbf{r}_t + \mathbf{r}_r \tag{5.16}$$

where $\mathbf{r}_t$ is the radial displacement due to lateral motion of the quadcopter and $\mathbf{r}_r$ is the radial displacement due to the rotational motion of the quadcopter. Radial displacement due to lateral motion $\mathbf{r}_t$ has a Gamma distribution Equation (5.13), and therefore $f_{r_t}(r_t)$ can be expressed as

$$f_{r_t}(r_t) = \frac{1}{\Gamma(a)\, b^a} r_t^{a-1} e^{-r_t/b}, \qquad r_t > 0 \tag{5.17}$$

where a is the shape parameter, b is the scale parameter and $\Gamma(.)$ is the Gamma function. Radial displacement due to rotational motion $\mathbf{r}_r$ is a function of the tilt angle β. Tilt angle can be expressed as

$$\beta = \arctan\left(\frac{r_r}{h}\right) \tag{5.18}$$

Therefore $\mathbf{r}_r$ can be expressed as

$$r_r = h\tan\left(\beta\right) \tag{5.19}$$

where h is the altitude of the UAV. As stated in 5.2.5.1 Tilt angle β has a log-normal distribution Equation (5.12). By applying density transformation between $\mathbf{r}_r$ and β and converting from degree to radians, $f_{r_r}\left(r_r\right)$ can be expressed as

$$f_{r_r}\left(r_r\right) = \frac{1}{\left(tan^{-1}\left(\frac{r_r}{h}\right)\right)\sigma\sqrt{2\pi}}\exp\left(-\frac{\left(\ln\left(tan^{-1}\left(\frac{r_r}{h}\right)\right)-\mu\right)^2}{2\sigma^2}\right)\frac{h}{h^2+r_r^2}\frac{180}{\pi} \tag{5.20}$$

where $h/(h^2+r_r^2)$ is the Jacobian. Pointing error h_p due to r can be expressed as Equation (2.4), and furthermore r can be expressed as

$$r \approx \sqrt{-0.5w_{z_{eq}}^2\ln\left(\frac{h_p}{A_0}\right)} \tag{5.21}$$

Incorporating the effect of two radial displacements, overall pointing error $f_{h_p}\left(h_p\right)$ for a hovering quadcopter UAV is described as

$$f_{h_p}\left(h_p\right) = f_{r_t}\left(r_t\right)\left|\frac{dr_t}{dh_p}\right| + f_{r_r}\left(r_r\right)\left|\frac{dr_r}{dh_p}\right| \tag{5.22}$$

$$\left|\frac{dr_t}{dh_p}\right| = \left|\frac{dr_r}{dh_p}\right| = \left|\frac{dr}{dh_p}\right| = \frac{w_{z_{eq}}^2}{4h_p\sqrt{-0.5w_{z_{eq}}^2\ln\left(\frac{h_p}{A_0}\right)}} \tag{5.23}$$

Subtituting Equation (5.17), Equation (5.20) and Equation (5.23) into Equation (5.22), $f_{h_p}\left(h_p\right)$ is obtained as

$$
\begin{aligned}
f_{h_p}\left(h_p\right) = & \left[\begin{array}{l} \left(\frac{1}{\Gamma(a)b^a} \left(\sqrt{-0.5 w_{z_{eq}}^2 \ln\left(\frac{h_p}{A_0}\right)} \right)^{a-1} \exp\left(- \frac{\sqrt{-0.5 w_{z_{eq}}^2 \ln\left(\frac{h_p}{A_0}\right)}}{b} \right) \right) \\
+ \left[\begin{array}{l} \frac{1}{\left(tan^{-1} \left(\frac{\left(\sqrt{-0.5 w_{z_{eq}}^2 \ln\left(\frac{h_p}{A_0}\right)}\right)}{h} \right) \right) \sigma\sqrt{2\pi}} \\
\times \exp\left(- \frac{\left(\ln\left(\tan^{-1}\left(\frac{\left(\sqrt{-0.5 w_{z_{eq}}^2 \ln(h_p/A_0)}\right)}{h} \right) \right) - \mu \right)^2}{2\sigma^2} \right) \\
\times \frac{h}{h^2 - 0.5 w_{z_{eq}}^2 \ln(h_p/A_0)} \frac{180}{\pi} \end{array} \right] \end{array} \right] \\
& \times \left(\frac{w_{z_{eq}}^2}{4h_p \sqrt{-0.5 w_{z_{eq}}^2 \ln\left(\frac{h_p}{A_0}\right)}} \right)
\end{aligned}
\tag{5.24}
$$

5.4 Conclusions

In this study we thoroughly modelled, simulated and analyzed hovering flight behavior of a quadcopter UAV under the presence of wind. Statistical analysis showed that the rotational and lateral motions caused by the wind disturbance on the UAV both follow distributions different than the ones present in current literature. We model and simulate a commercial UAV, hovering at a set altitude while facing von Kármán winds for long durations. Extensive simulations were carried out for various wind speeds and directions. It is observed that by analyzing the tilt angle, its effect on pointing error is statistically modelled accurately without bearing any dependence on the wind heading angle. Afterwards, we derive 3rd order polynomial approximations for both tilt angle and lateral displacement distributions for a given wind speed. These approximations are then used to model the PE for a quadcopter UAV in the presence of winds.

6. CONCLUSIONS AND FUTURE WORK

In this study we performed an in depth analysis of the pointing error in FSO communication systems. While doing so, our focus was to relate the pointing error to the underlying physical phenomena causing the error in the first place. To do so, we have used both experimental and simulation based approaches to model the behavior of the optical channel.

Design and manufacturing of a 5-axis XYZ table has proven itself to be reliable yet cost effective platform to experimentally test pointing error. Currently there are no works in the literature that experimentally tested the pointing error as presented in this study. More so, the XYZ table can be used to test for cases for a non-Gaussian beam, such as Top-Hat or Laguerre-Gaussian beams. Analysis of these beams in the presence of pointing errors experimentally have not been studied in any of the existing literature yet. More so, motion of a 3rd, then 4th and 5th axes can be included and resulting pointing error models can be measured. This type of multi-dimensional, simultaneous and controllable motion capability would be very beneficial in the performance analysis of terrestrial, aerial and underwater FSO systems.

Pointing error in the terrestrial FSO links are studied in this work, and the relationship between the building sway caused by winds and the statistical behavior of pointing error are derived. Using an industry standard civil engineering software to simulate the sway, led to the possibility of parametric analysis of the pointing error behavior. This analysis can be further continued in the following fashion. Currently, the sway behavior of the building motion is only considered as a linear translation. However building, when a building sways it also undergoes a torsion as well. This amount of torsion is proportional to the amplitude of the sway, which is a function of building height, width and wind speed as presented by this study. When a building faces torsion, this creates not a linear translation, but instead results in a fluctuation in orientation. This orientation change, expressed in milli radians, creates a divergence in the transmitted optical beam. The effect of this divergence is also proportional to the link distance. So in theory, an optimal link distance in the presence of building sway due to wind can be studied. This currently does not exist in literature.

Pointing error and closed form BER for a buoy based UWOC system is studied by using an industry standard oceanographic marine simulation software. Parametric analysis of buoy motion is performed under various environmental conditions. For future work, translational motion of the buoy due to environmental factors can also be studied. This translational motion will also create a pointing error, similar to boresight, and should be counted for if accurate modelling of the UWOC channel is sought after.

For an aerial FSO system, PE model is derived for a quadcopter UAV hovering in the presence of wind. Parametric analysis of the hover behavior and its effect on PE is analyzed through extensive simulations. To numerically analyze the channel performance, closed-form BER derivation can be further studied. More so, UAV-to-UAV scenarios can also be simulated and studied. For these scenarios, the AoA between the UAVs, affected by the variations in the yaw angle of the quadcopter will also have an effect. Furthermore, an optimization study can be carried out to find out the most optimum flight altitude for a quadcopter carrying an FSO unit in the presence of wind. This study can then be further extended to include energy management constraints as well.

REFERENCES

[1] M. Uysal and et al., *Optical Wireless Communications: An Emerging Technology*. Springer, 2016.

[2] A. Khalighi and M. Uysal, "Survey on free space optical communication: A communication theory perspective," *IEEE Communications Surveys & Tutorials*, vol. 16, no. 4, pp. 2231–2258, 2014. Fourthquarter.

[3] L. C. Andrews and R. L. Phillips, *Laser Beam Propagation Through Random Media*. SPIE Optical Engineering Press, 1998.

[4] X. Sun, C. H. Kang, M. Kong, O. Alkhazragi, Y. Guo, M. Ouhssain, Y. Weng, B. H. Jones, T. K. Ng, and B. S. Ooi, "A review on practical considerations and solutions in underwater wireless optical communication," *Journal of Lightwave Technology*, vol. 38, pp. 421–431, 2020.

[5] Z. Zeng, S. Fu, H. Zhang, Y. Dong, and J. Cheng, "A survey of underwater optical wireless communications," *IEEE Communications Surveys Tutorials*, vol. 19, pp. 204–238, Q1 2017.

[6] M. T. Dabiri, S. M. S. Sadough, and M. A. Khalighi, "Channel modeling and parameter optimization for hovering uav-based free-space optical links," *IEEE Journal on Selected Areas in Communications*, vol. 36, pp. 2104–2113, September 2018.

[7] A. A. Hoshu, G. E. M. Abro, M. Alhussein, I. A. Tunio, K. Aurangzeb, and A. Ali, "Cascaded control system design for quadrotor uav through relay with embedded integrator-based automatic tuning approach," *International Journal of Aerospace Engineering*, p. 6651286, 2023.

[8] National Instruments, Corp., "Labview version: 2015 - 64bit." `https://www.ni.com/en.html`, 2024. Accessed: February 01, 2024.

[9] The MathWorks, Inc., "Matlab r2024a," 2024. Accessed: July 12, 2025.

[10] J. D. Barry and G. S. Mecherle, "Beam pointing error as a significant parameter for satellite borne, free-space optical communication systems," *Optical Engineering*, vol. 24, pp. 1049–1054, Nov. 1985.

[11] A. A. Farid and S. Hranilovic, "Outage capacity optimization for free-space optical links with pointing errors," *Journal of Lightwave Technology*, vol. 25, pp. 1702–1710, Jul. 2007.

[12] W. Gappmair, S. Hranilovic, and E. Leitgeb, "Ook performance for terrestrial fso links in turbulent atmosphere with pointing errors modeled by hoyt distributions," *IEEE Communications Letters*, vol. 15, pp. 875–877, Aug. 2011.

[13] R. Boluda-Ruiz, A. Garcia-Zambrana, C. Castillo-Vázquez, and B. Castillo-Vázquez, “Novel approximation of misalignment fading modeled by beckmann distribution on free-space optical links,” *Optics Express*, vol. 24, pp. 22635–22649, 2016.

[14] K. Jung, S. S. Nam, M. Alouini, and Y. Ko, “Unified finite series approximation of fso performance over strong turbulence combined with various pointing error conditions,” *IEEE Transactions on Communications*, vol. 68, pp. 6413–6425, Oct. 2020.

[15] M. A. Amirabadi and V. T. Vakili, “A new optimization problem in fso communication system,” *IEEE Communications Letters*, vol. 22, pp. 1442–1445, Jul. 2018.

[16] S. Arnon, “Effects of atmospheric turbulence and building sway on optical wireless communication systems,” *Optics Letters*, vol. 28, pp. 129–131, Jan. 2003.

[17] H. Sandalidis, T. Tsiftsis, G. Karagiannidis, and M. Uysal, “Ber performance of fso links over strong atmospheric turbulence channels with pointing errors,” *IEEE Communications Letters*, vol. 12, pp. 44–46, Jan. 2008.

[18] H. Sandalidis, T. Tsiftsis, and G. Karagiannidis, “Optical wireless communications with heterodyne detection over turbulence channels with pointing errors,” *Journal of Lightwave Technology*, vol. 27, pp. 4440–4445, Oct. 2009.

[19] W. Gappmair, S. Hranilovic, and E. Leitgeb, “Performance of ppm on terrestrial fso links with turbulence and pointing errors,” *IEEE Communications Letters*, vol. 14, pp. 468–470, May 2010.

[20] A. Garcia-Zambrana, B. Castillo-Vazquez, and C. Castillo-Vazquez, “Asymptotic error-rate analysis of fso links using transmit laser selection over gamma-gamma atmospheric turbulence channels with pointing errors,” *Optics Express*, vol. 20, pp. 2096–2109, Jan. 2012.

[21] “Etabs — building analysis and design.” `https://www.csiamerica.com/products/etabs`. Accessed: Jul. 14, 2022.

[22] C. Dyrbye and S. O. Hansen, *Wind Loads on Structures*. Chichester: Wiley, 1997. Print.

[23] A. Nyberg and G. Soderlund, “Wind-induced acceleration in high-rise buildings: An investigation on the dynamic effects due to a deep foundation.” Master’s Thesis, Chalmers University of Technology, 2017.

[24] U. of Notre Dame, “Nathaz on-line wind simulator.” `http://windsim.ce.nd.edu`. Accessed: Jan. 20, 2020.

[25] ASCE - American Society of Civil Engineers, "Asce 7 standard." `https://www.asce.org/publications-and-news/asce-7P`. Accessed: Jul. 14, 2022.

[26] N. W. S. N. Oceanic and A. Administration, "Estimating wind." `https://www.weather.gov/pqr/windhtml`. Accessed: Aug. 16, 2022.

[27] H. Park, H. Shon, I. Kim, and J. Park, "Monitoring of structural behavior of high-rise buildings using gps," *Council on Tall Buildings and Urban Habitat Conference*, Oct. 2004.

[28] J. Wu, *Field measurements and numerical study of wind effects on tall buildings*. PhD thesis, City University of Hong Kong, Kowloon Tong, Hong Kong, 2006.

[29] A. A. Farid and S. Hranilovic, "Diversity gain and outage probability for mimo free-space optical links with misalignment," *IEEE Transactions on Communications*, vol. 60, pp. 479–487, Feb. 2012.

[30] M. Chiani, D. Dardari, and M. Simon, "New exponential bounds and approximations for the computation of error probability in fading channels," *IEEE Transactions on Wireless Communications*, vol. 2, no. 4, pp. 840–845, 2003.

[31] Wolfram Inc., "Exponential function: Integration (formula 01.03.21.0056)." `https://functions.wolfram.com/ElementaryFunctions/Exp/21/01/02/01/01/04/0001/`. Accessed: Jun. 16, 2024.

[32] C. Roa, M. Roa, T. Radoo, A. Jurado-Navas, and M. del Castillo Vazquez, "Cooperative terrestrial–underwater fso system: Design and performance analysis," *Photonics*, vol. 11, p. 58, Jan. 2024.

[33] M. A. Khalighi, C. Gabriel, T. Hamza, S. Bourennane, P. Léon, and V. Rigaud, "Underwater wireless optical communication; recent advances and remaining challenges (invited paper)," in *IEEE International Conference on Transparent Optical Networks (ICTON)*, (Graz, Austria), 2014.

[34] Z. Vali, D. Michelson, Z. Ghasseölooy, and H. Noori, "A survey of turbulence in underwater optical wireless communications," *Optik*, vol. 320, Feb. 2025.

[35] S. Tang, Y. Dong, and X. Zhang, "On link misalignment for underwater wireless optical communication," *IEEE Communications Letters*, vol. 16, no. 10, pp. 1688–1690, 2012.

[36] S. Yu, J. Ding, Y. Fu, *et al.*, "Novel approximate and asymptotic expressions of the outage probability and ber in gamma-gamma fading fso links with generalized pointing errors," *Optics Communications*, vol. 435, pp. 289–296, 2019.

[37] F. Yang, J. Cheng, and T. Tsiftsis, "Free-space optical communication with nonzero boresight pointing errors," *IEEE Transactions on Communications*, vol. 62, pp. 713–725, Feb. 2014.

[38] I. C. Ijeh, M. A. Khalighi, M. Elamassie, S. Hranilovic, and M. Uysal, "Outage probability analysis of a vertical underwater wireless optical link subject to oceanic turbulence and pointing errors," *Journal of Optical Communications and Networking*, vol. 14, pp. 439–453, Jun. 2022.

[39] R. B. Ruiz, A. G. Zambrana, B. C. Vázquez, and S. Hranilovic, "Impact of angular pointing error on ber performance of underwater optical wireless links," *Optics Express*, vol. 28, pp. 34606–34622, 2020.

[40] J. E. Han, S. S. Nam, C. Yoon, D. D. Hwang, and M. Alouini, "Asymptotic ergodic capacity analysis for fso communication between mobile platforms in maritime environments," *Applied Sciences*, vol. 13, no. 12, p. 6978, 2023.

[41] H. Zhang, Y. Dong, and L. Hui, "On capacity of downlink underwater wireless optical mimo systems with random sea surface," *IEEE Communications Letters*, vol. 19, pp. 2166–2169, 2015.

[42] I. C. Ijeh, O. Haddad, and M. A. Khalighi, "Ergodic capacity of a vertical underwater wireless optical communication link subject to misalignment," in *2022 4th West Asian Symposium on Optical and Millimeter-wave Wireless Communications (WASOWC)*, (Tabriz, Iran, Islamic Republic of), pp. 1–5, 2022.

[43] Q. Zhang, D. Yue, and X. Xu, "Performance analysis of fixed gain relay-assisted vertical uwoc systems with generalized misalignment fading model," *Applied Optics*, vol. 63, pp. 5064–5078, 2024.

[44] R. A. Khalil, M. I. Babar, N. Saeed, T. Jan, and H.-S. Cho, "Effect of link misalignment in the optical-internet of underwater things," *Electronics*, vol. 9, p. 646, 2020.

[45] Y. Dong, S. Tang, and X. Zhang, "Effect of random sea surface on downlink underwater wireless optical communications," *IEEE Communications Letters*, vol. 17, pp. 2164–2167, Nov. 2013.

[46] J. Wang, S. Rajbhandari, and W. O. Popoola, "Performance of uplink underwater optical wireless communications in the presence of random sea surface," in *2022 13th International Symposium on Communication Systems, Networks and Digital Signal Processing (CSNDSP)*, (Porto, Portugal), pp. 784–789, 2022.

[47] C. Jiang, O. Moctar, and T. E. Schellin, "Mooring-configurations induced decay motions of a buoy," *Journal of Marine Science and Engineering*, vol. 9, no. 3, p. 350, 2021.

[48] H. Zheng, Y. Chen, Q. Liu, Z. Zhang, Y. Li, and M. Li, "Theoretical and numerical analysis of ocean buoy stability using simplified stability parameters," *Journal of Marine Science and Engineering*, vol. 12, no. 6, p. 966, 2024.

[49] S. Tang, X. Zhang, and Y. Dong, “Temporal statistics of irradiance in moving turbulent ocean,” in *Proc. MTS/IEEE OCEANS-Bergen*, pp. 1–4, 2013.

[50] M. V. Jamali, F. Akhoundi, and J. A. Salehi, “Performance characterization of relay-assisted wireless optical cdma networks in turbulent underwater channel,” *IEEE Transactions on Wireless Communications*, vol. 15, pp. 4104–4116, 2016.

[51] Z. Vali, A. Gholami, Z. Ghassemlooy, D. G. Michelson, M. Omoomi, and H. Noori, “Modeling turbulence in underwater wireless optical communications based on monte carlo simulation,” *Journal of the Optical Society of America A*, vol. 34, pp. 2096–2106, 2017.

[52] M. P. Bernotas and C. Nelson, “Probability density function analysis for optical turbulence with applications to underwater communications systems,” in *Proceedings of Ocean Sensing and Monitoring VIII*, vol. 9827, May 2016.

[53] M. P. Bernotas and C. Nelson, “Probability density function analysis for optimization of underwater communications systems,” in *OCEANS 2015 – MTS/IEEE*, (Washington), pp. 1–8, 2015.

[54] H. M. Oubei, E. Zedini, R. T. ElAfandy, A. Kammoun, M. Abdallah, T. K. Ng, M. Hamdi, M. S. Alouini, and B. S. Ooi, “Simple statistical channel model for weak temperature-induced turbulence in underwater wireless optical communication systems,” *Optics Letters*, vol. 42, pp. 2455–2458, 2017.

[55] M. V. Jamali, A. Mirani, A. Parsay, B. Abolhassani, P. Nabavi, A. Chizari, P. Khorramshahi, S. Abdollahramezani, and J. A. Salehi, “Statistical studies of fading in underwater wireless optical channels in the presence of air bubble, temperature, and salinity random variations,” *IEEE Transactions on Communications*, vol. 66, pp. 4706–4723, 2018.

[56] M. V. Jamali, P. Khorramshahi, A. Tashakori, A. Chizari, S. Shahsavari, S. AbdollahRamezani, M. Fazeliam, S. Bahrani, and J. A. Salehi, “Statistical distribution of intensity fluctuations for underwater wireless optical channels in the presence of air bubbles,” in *2016 Iran Workshop on Communication and Information Theory (IWCIT)*, (Tehran, Iran), pp. 1–6, 2016.

[57] H. M. Oubei, E. Zedini, R. T. ElAfandy, A. Kammoun, T. K. Ng, M. S. Alouini, and B. S. Ooi, “Efficient weibull channel model for salinity induced turbulent underwater wireless optical communications,” in *Opto-Electronics and Communications Conference (OECC) and Photonics Global Conference (PGC)*, (Singapore), pp. 1–2, 2017.

[58] Y. Fu, W. Duan, C. Huang, Y. Du, and L. Zhou, “Average ber performance of rectangular qam-uwoc over strong oceanic turbulence channels with pointing error,” *Optics Communications*, vol. 476, p. 126362, 2020.

[59] S. Kumar, S. Prince, J. V. Aravind, and S. Kumar, "Analysis on the effect of salinity in underwater wireless optical communication," *Marine Georesources Geotechnology*, vol. 38, no. 3, pp. 291–301, 2019.

[60] W. H. W. Hassan, N. B. Sanmugam, F. Jasman, M. R. Awal, A. N. Dagang, Z. A. Mutalip, and S. M. Idrus, "Experimental study on the effect of water salinity in the underwater optical wireless communication (uowc) channel," *Journal of Communications*, vol. 19, no. 9, pp. 433–440, 2024.

[61] C. Eskilsson and J. Palm, "High-fidelity modelling of moored marine structures: multi-component simulations and fluid-mooring coupling," *Journal of Ocean Engineering and Marine Energy*, vol. 8, pp. 513–526, 2022.

[62] ProteusDS, "Proteusds." `https://proteusds.com/proteusds/`. Accessed: May 12, 2025.

[63] A. R. Westcott, L. G. Bennetts, N. Y. Sergiienko, and B. S. Cazzolato, "Broadband near-perfect capture of water wave energy by an array of heaving buoy wave energy converters," *Journal of Fluid Mechanics*, vol. 998, October 2024.

[64] O. M. Mazzaretto, M. Menéndez, and H. Lobeto, "A global evaluation of the jonswap spectra suitability on coastal areas," *Ocean Engineering*, vol. 266, p. 2, 2022.

[65] K. E. Kaasen, "Time domain model representations of standard wind gust spectra," in *9th International Offshore and Polar Engineering Conference*, (Brest, France), May 1999.

[66] International Organization for Standardization, "Petroleum and natural gas industries—specific requirements for offshore structures—part 1: Metocean design and operating considerations," 2015.

[67] Mobilis, "Jet 7000 - mexico – mobilis." `https://mobilis-sa.com/en/ref/jet-7000-mexico/`. Accessed: May 12, 2025.

[68] Mobilis, "Jet 7000 - mexico - mobilis – technical sheet." `https://mobilis-sa.com/wp-content/uploads/2021/01/jet-7000-qi-pf5-eaux-saines.pdf`. Accessed: May 12, 2025.

[69] C. M. Bishop, *Pattern Recognition and Machine Learning*. New York, USA: Springer, 2006.

[70] C. Berganski, A. Hoffmann, and R. Möller, "Tilt correction of panoramic images for a holistic visual homing method with planar-motion assumption," *Robotics*, vol. 12, p. 20, January 2023.

[71] X. Zhu and J. M. Kahn, "Free-space optical communication through atmospheric turbulence channels," *IEEE Transactions on Communications*, vol. 50, pp. 1293–1300, August 2002.

[72] L. Diao, M. Wang, and Y. Peng, "Scintillation index based on modified bessel beam in ocean turbulence," in *Proc. SPIE First International Conference on Spatial Atmospheric Marine Environmental Optics*, vol. 12706, (Shanghai, China), May 2023.

[73] M. Abramowitz and E. A. Stegun, *Handbook of Mathematical Functions*. USA: Dover, December 1972.

[74] N. W. S. Oceanic and A. Administration, "Estimating wind." `https://www.weather.gov/pqr/wind`. Accessed: May 1, 2025.

[75] W. Fawaz, C. Abou-Rjeily, and C. Assi, "Uav-aided cooperation for fso communication systems," *IEEE Communications Magazine*, vol. 56, pp. 70–75, January 2018.

[76] A. Kaadan, H. H. Refai, and P. G. LoPresti, "Multielement fso transceivers alignment for inter-uav communications," *Journal of Lightwave Technology*, vol. 32, pp. 4785–4795, December 15 2014.

[77] S. Huang and M. Safari, "Free-space optical communication impaired by angular fluctuations," *IEEE Transactions on Wireless Communications*, vol. 16, pp. 7475–7487, November 2017.

[78] M. T. Dabiri, M. Rezaee, I. S. Ansari, and V. Yazdanian, "Channel modeling for uav-based optical wireless links with nonzero boresight pointing errors," *IEEE Transactions on Vehicular Technology*, vol. 69, pp. 14238–14246, December 2020.

[79] A. Komaee, P. Krishnaprasad, and P. Narayan, "Active pointing control for short range free-space optical communication," *Communications in Information Systems*, vol. 7, no. 2, pp. 177–194, 2007.

[80] M. T. Dabiri, S. M. S. Sadough, and I. S. Ansari, "Tractable optical channel modeling between uavs," *IEEE Transactions on Vehicular Technology*, pp. 1–1, 2019.

[81] A. Kaadan, H. Refai, and P. Lopresti, "Spherical fso receivers for uav communication: Geometric coverage models," *IEEE Transactions on Aerospace and Electronic Systems*, vol. 52, pp. 2157–2167, October 2016.

[82] D. Singh and S. R, "Comprehensive performance analysis of hovering uav-based fso communication system," *IEEE Photonics Journal*, vol. 14, October 2022.

[83] A. J. Mahdi, W. J. Mazher, and O. N. Ucan, "Hovering drones-based fso technology in weak atmospheric turbulence with pointing error," in *2021 International Conference on Computing and Communications Applications and Technologies (I3CAT)*, (United Kingdom), pp. 52–56, 2021.

[84] I. S. Ansari, F. Yilmaz, and M. S. Alouini, "Impact of pointing errors on the performance of mixed rf/fso dual-hop transmission systems," *IEEE Wireless Communications Letters*, vol. 2, no. 3, pp. 351–354, 2013.

[85] J. Harris, J. J. Sluss, H. H. Refai, and P. G. Lopresti, "Alignment and tracking of a free-space optical communications link to a uav," in *Digital Avionics Systems Conference*, vol. 1, pp. 1.c.2–1.1–9, December 2005.

[86] N. Nallagonda and K. Prabu, "Performance analysis of fso based inter-uav communication systems," *Optical and Quantum Electronics*, vol. 53, April 2021.

[87] R. Mahony, V. Kumar, and P. Corke, "Multirotor aerial vehicles: Modeling, estimation, and control of quadrotor," *IEEE Robotics Automation Magazine*, vol. 19, pp. 20–32, September 2012.

[88] B. L. Stevens, F. L. Lewis, and E. N. Johnson, *Aircraft Control and Simulation*. Wiley, 3rd ed., 2015.

[89] DJI, "Dji matrice 300 rtk — dji store." `https://www.djistoreturkiye.com/dji-matrice-300-rtk`. Accessed: Jun. 6, 2025.

[90] "Flying qualities of piloted airplanes," tech. rep., U.S. Department of Defense, 1980.

[91] T. C. Y. Wang, G. G. Fuller, and A. S. Willsky, "Modeling and simulation of atmospheric turbulence for flight control system design," *AIAA Journal*, vol. 14, no. 5, pp. 642–649, 1976.

VITA

Name-Surname: Hasan Tahsin Toplar

Education:

- Doctor of Philosophy (PhD.) in Electrical and Electronics Engineering (Part-time) (2017-2025) - Özyeğin University (Istanbul, Turkey)

- Master of Applied Science (MSc.) in Mechanical Engineering (2012-2014) - The University of Waterloo (Waterloo, Ontario, Canada)

- Bachelor in Applied Science (BASc.) Honours Mechatronics Engineering (2004-2009) - The University of Waterloo (Waterloo, Ontario, Canada)

- International Baccalaureate Diploma (2002-2004) - Eyuboglu High School (Istanbul, Turkey)

Work Experience:

- Entrepreneur & Design Consultant (2015-Present) - Activity Network A.Ş. (Istanbul, Turkey)

- Part-time Lecturer (2017-Present) - Özyeğin University (Istanbul, Turkey)

- Researcher at Mechatronic Vehicle Systems Laboratory (2012-2015) - The University of Waterloo (Waterloo, ON, Canada)

- Hardware Design Engineer (2009-2011) - Alcatel-Lucent Corporation (Ottawa, ON, Canada)

- FPGA, Firmware and Hardware Design Engineer Intern (2007-2008) - Nuvation Research (Waterloo, ON, Canada)
- Electro-Mechanical Engineer Intern (2005-2006) - NCR Limited (Waterloo, ON, Canada)
- Test Equipment Intern (2005) - Oz Optics Limited (Ottawa, ON, Canada)

Awards and Scholarships:

- Teaching Assistant Scholarship (2017-2025) - Özyeğin University (Istanbul, Turkey)
- Full Scholarship during Master of Applied Science (2012-2014) - The University of Waterloo (Waterloo, Ontario, Canada)
- International Student Scholarship (5000$/year) during Bachelor in Applied Science (2004-2009) - The University of Waterloo (Waterloo, Ontario, Canada)
- Won NESA (Near East South Asia Council of Overseas Schools and ECIS (European Council of International Schools) Math Prizes in 1999, 2002 and 2003

Scientific Publications:

- H. T. Toplar and M. Uysal, ”Modeling of Pointing Errors in Terrestrial FSO Links Caused by Building Sway Under Wind Loads,” in IEEE Open Journal of the Communications Society, vol. 6, pp. 1161-1169, 2025, doi: 10.1109/OJCOMS.2025.3537017.

Scientific Presentations:

- H. T. Toplar and M. Uysal, ”Design of a Motion Table for Experimental Verification of Pointing Error in FSO Systems,” 2024 32nd Signal Processing and Communications Applications Conference (SIU), Mersin, Turkiye, 2024, pp. 1-4, doi: 10.1109/SIU61531.2024.10600865.